CORE-SHELL STRUCTURED FILAMENTS FOR FUSED FILAMENT FABRICATION THREE-DIMENSIONAL PRINTING & ROLL-TO-ROLL MANUFACTURING OF PIEZORESISTIVE ELASTOMERIC FILMS

A Dissertation

Presented to

The Graduate Faculty of The University of Akron

In Partial Fulfillment

of the Requirements for the Degree

Doctor of Philosophy

Fang Peng

December, 2018

CORE-SHELL STRUCTURED FILAMENTS FOR FUSED FILAMENT FABRICATION THREE-DIMENSIONAL PRINTING & ROLL-TO-ROLL MANUFACTURING OF PIEZORESISTIVE ELASTOMERIC FILMS

Fang Peng

Dissertation

Approved:	Accepted:
_____	_____
Advisor Dr. Bryan D. Vogt	Department Chair Dr. Sadhan C. Jana
_____	_____
Advisor Dr. Mukerrem Cakmak	Interim Dean of the College Dr. Ali Dhinojwala
_____	_____
Committee Member Dr. Mark D. Soucek	Dean of Graduate School Dr. Chand Midha
_____	_____
Committee Member Dr. Yu Zhu	Date
_____	
Committee Member Dr. Kwek-Tze Tan	

ABSTRACT

Fused Filament Fabrication (FFF) is an extrusion-based 3D-printing techniques in which molten polymer filament is extruded to produce 3D objects. Fused Filament Fabrication (FFF) has become one of the most popular 3D printing techniques due to its low cost, high safety, and accessibility for consumer market. However, the intrinsic poor adhesion at filament bonding interfaces leads to poor mechanical properties of FFF manufactured parts, and the highly non-isothermal FFF process leads to warping deformation and voids in the incompletely filled products.

The first part of this dissertation presents an experimental approach to measure the flow and temperature history of the non-isothermal melt extrusion process in FFF. The flow profile is measured by incorporating a pigmented polycarbonate (PC) fibres into the PC filament, and the and the temperature history is measured by an ultrafine thermocouple that flows through the extruder. Comparison with a flow model developed for isothermal flow demonstrate the critical role of radial temperature gradient in controling the velocity profile during the melt extrusion.

The second part presents a novel strategy of using a core-shell structured filament in FFF 3D printing to overcome the bond weakness at filament bonding interfaces in FFF manufactured parts. First, we demonstrate that polycarbonate-based filaments with high T_g core and low T_g shell yield improved bond strength at layer-interface and a synergistic improvement of impact properties. Further, we demonstrate that utilizing an ionomer shell – PC shell combination leads to an even stronger shell-shell bonding interface between adjacent filaments while each printed filament is filled with a continuous PC core which acts as fiber reinforcements. As a result, samples printed from core-shell filaments show significantly enhanced mechanical strength, which manifests non-break sample and improved impact resistance in notched Izod-impact tests. In addition, the printed core-shell sample less warpage caused by internal stress and better ability to print overhang features as compared to monofilaments.

The third part of this dissertation presents a scalable roll-to-roll (R2R) process to fabricate elastomeric films with tunable piezo-resistivity through the use of magnetic field to align commercially available nickel (core)@silver (shell) particles (Ni@Ag) in a polydimethylsiloxane (PDMS) matrix. We find that the Ni@Ag particles in aligned chains are in loose contact with adjacent particles.

As a result, the PDMS/Ni@Ag films exhibit piezo-resistivity behavior along thickness direction because a pressure applied to this structure can increase the connectivity of the particles and thus electrical conductivity.

ACKNOWLEDGEMENT

Many people have helped me during my last five years as a Ph.D student in the University of Akron, I would like to express my sincere gratitude to them. I couldn't have finished this dissertation without their help.

I wish to thank, first and foremost, both of my advisers, Dr. Miko Cakmak and Dr. Bryan D Vogt for their continuous support and valuable guidance throughout my graduate education. Dr. Cakmak have not only taught how to conduct research, but also how to think as a polymer engineer. His constant demand for excellence will always motivate me to improve myself. After Dr. Cakmak moved to Purdue University, Dr. Vogt generously took me in his group and provided me with his help. Dr. Vogt guided me into the right direction of research when I felt overwhelmed by experiments from different projects. His valuable guidance on analyzing results, experiment planning and scientific writing has led my work to become meaningful and publishable.

Then, I would also like to thank my committee members, Dr. Mark Soucek, Dr. Yu Zhu and Dr. Kwek-Tze Tan for their constructive and insightful suggestions on my research. I am grateful to all faculty members in the college of polymer science & Engineering for the excellent education they have

provided to me on classes. I am also grateful to staffs in the department, especially Deb Wilhite, Randall Marvel and Thomas Patrick for their unfailing support and assistance.

Furthermore, I wish to thank Don Wardius, Ernesto Silva Mojica and Marina Rogunova from Covestro LLC for providing materials and financial support for my research project. I also wish to thank Adam Woods and Piljae Joo for their help with 3D-scanning.

I wish to thank all my group members in both Prof. Cakmak's group and Prof. Vogt's group for all your support. My special thanks go to Keke Chen, Enmin Wang, Yuanhao Guo, Yuwei Chen, Tsang-min Huang, Chao Wang, Zhiyang Zhao, Xuhui Xia, and Yanfeng Xia. They have not only been supportive colleagues who I can rely on at work, but also good friends who gives me encouragement and life advice. I am also grateful to all my friends especially Yuanzhong Zhang, Xiangqian Hong, Chi Zhang, Yan Chen, Tong Xu, and Han Lin. I will never forget the good times we spent together.

Finally, I would like to thank my parents for all their unconditional support throughout my life.

TABLE OF CONTENTS

TABLE OF FIGURES

CHAPTER I

INTRODUCTION

Three-dimensional printing, alias Additive Manufacturing, is a process of joining materials to fabricate physical parts directly from a virtual computer aided designed model data as opposed to conventional manufacturing methodologies, subtractive and formative manufacturing.[1] Unlike conventional manufacturing methods that requires molds, dies (formative manufacturing) or cutting tooling (subtractive manufacturing), three-dimensional printing (3D-printing) techniques allows tool-less production of customized parts on demand and fabrication of highly complex structures. 3D-printing have been widely used in rapid prototyping of new designs for aerospace[2–4], automotive[5–7], biomedical applications[8–11]. With advances in 3D-printing technologies, 3D-printed parts now are also widely used as final products. By providing the ability to produce parts on demand, 3D-printing are used to make personalized medical devices[12,13] and orthopedic implants[14] to fit individual patient. 3D-printing are also widely used to highly complex structures like scaffolds for tissue engineering[15–17], micro fluidics[18–20] and autonomous robots[21,22].

A broad range of techniques has been introduced over the last 4 decades including ink[23–25], photopolymerization[26–28], powder bed[29–31] and extrusion[32–34] based printing techniques. Fused Filament Fabrication(FFF) is one of the most

popular 3D printing techniques due to its low cost[35], high safety in office-friendly environment[32], and accessibility for consumer market. Fused Filament Fabrication (FFF), or alias material extrusion additive manufacturing, is an extrusion-based 3D-printing process where continuous molten polymer filament is extruded out of a nozzle and deposited onto the growing workpiece to produce 3D objects. However, the parts printed by FFF often show poor mechanical properties due to the poor bond strength between joined filaments. Additionally, because FFF process is highly non-isothermal, complex temperature and flow history during filament extrusion and deposition leads to other quality issues of 3D-printed objects including warping deformation[36–38] and porosity induced by incomplete infill[39,40]. Therefore, the goal of this research includes: 1) understanding the complex flow and temperature history in FFF printing process and 2) development of core-shell filaments to overcome the bond weakness in FFF 3D-printed parts.

Chapter II provides a fundamental review of different 3D-printing techniques and their advantages with an emphasis on Fused Filament Fabrication 3D-printing techniques.

Chapter III describes an experimental approach of analyzing the flow behaviour and temperature history of the FFF extrusion process. In FFF, the extruder uses two pinch rollers to continuously feed a thermoplastic filament

into a temperature-controlled heated barrels which are often referred to as liquefier or hot-end. In the liquefier, the filament is melted while the incoming cold solid filament pushes the melt through the nozzle (0.2-0.6mm in diameter) of the liquefier. The unique self-extruding filament that acts as both feedstock and plunger simplifies the structures of FFF extruders, allowing simple mounting onto a desktop CNC gantry for controlled x-y motions. This FFF extrusion process is significantly different from traditional polymer filament extrusion process, such as a single-screw extruder where frictional heating from the screw is the dominant energy source to transform the solid polymer to the melt and the screw homogenizes the polymer melt as well as generates significant pressure to drive isothermal melt flow through the die [41]. Conversely in FFF extruder, the filament in the liquefier is heated only by the heat conduction from the liquefier barrel. The poor thermal conductivity of polymer leads to severe temperature gradients along both extrusion direction and radial direction of the nozzle which are not present in conventional extrusion processes. This temperature gradient could lead to complexity in flow and thermal histories of the self-extruding filament which could impact the properties of the 3D-printed products[42] and we have limited understanding of the complex flow and temperature profile associated with the FFF extrusion process[43]. Understanding the melt flow behavior in FFF extrusion process could facilitate the optimization of extrusion condition and design of new FFF extruder flow

channel. Therefore, Flow history of the FFF melt extrusion process is measured by incorporating a pigmented polycarbonate (PC) fibres into the PC 3D-printing filament being extruded, and the temperature history through the extruder is measured by using an ultrafine thermocouple that is embedded in the centre of the filament and flows along with the filament during extrusion. Through the measurements, we demonstrate the FFF extrusion process is highly non-isothermal and the radial temperature gradient leads to a more blunted velocity profile as compared to that expected for an isothermal power-law fluid.

In conventional thermoplastic processing techniques such as injection moulding, polymer melt is injected into the cavity of a mould, and a dense solid object is formed as the melt cools down. FFF 3D-printing builds a part by adding materials in a layer-by-layer fashion. During an FFF 3D-printing process, the extruder of the 3D printer deposits molten polymer filaments onto the preceding layer. The bond formation between layers and filaments relies on the thermal energy of the polymer melt to re-melt the preceding layer and fuse the adjacent layers together, whereas the molten polymer must solidify fast enough to ensure the part that has been built does not deform. Therefore, the fast solidification of the melt leads to low bond strength because chain diffusion is soon prohibited as the polymer melt solidifies[44]. Because of the weak bond strength at the layer interface, the mechanical properties of the parts fabricated by FFF is worse than that of injection moulded or extruder extruded parts[45–48].

Additionally, because the flow of the polymer melt is required to be limited to maintain the shape accuracy, the part is often not completely filled, thus leaving gaps voids inside the printed parts[39,49]. Because of the circular opening of printer's nozzle, the extruded polymer filament tends to have an elliptical cross-section and elliptical bodies cannot be perfectly stacked, thus making complete part filling even more difficult due to additional flow requirements. Both experimental[45,46,48,50,51] and finite element modelling (FEM) [52] studies of FFF 3D printing have shown that gaps and voids in 3D-printed samples could result in an even worse mechanical strength as it can induce severe strain energy concentration. Many studies have been carried out to improve the mechanical properties and dimensional accuracy of the printed part through optimization of printing conditions[32,34,53–59]. It is reported that high extrusion temperature or printing in a warm chamber results in better bond strength[57,60] and less unfilled cavity[42,61]. However, high processing temperature could potentially lead to over-heating of the print model, resulting in distortion of the part, especially on overhanging[62] and thin features[63]. In Chapter IV and V, we describe a novel approach that can overcome the inherent bond weakness in FFF 3D-printed parts through a material design approach of using core-shell structured filament. These filaments are composed of high glass-transition temperature (T_g) cores and shells with low solidification temperature (T_g or crystallization temperature-T_c) or low melt viscosity. The high T_g core that acts as a "stiff skeleton" to

maintain shape accuracy during printing and reinforce the printed part while the low T_g shell enables improved interdiffusion of polymers between adjacent printed layers. Chapter IV focuses on the development of a co-extrusion system for fabrication of bi-layer polycarbonate-based core-shell filaments along with various processing challenges. We demonstrate that the co-extrusion system is capable of fabricating core-shell filaments composed with various core-shell ratio. 3D-printing of core-shell filaments composed of both high-viscosity@low-viscosity and high-T_g@low-T_g PC were investigated. The results of mechanical test demonstrate that low viscosity/low T_g shell could promote bond strength at layer interface and high T_g/high viscosity core can help to maintain the shape accuracy and broaden the processing window of extrusion and bed-temperature. In Chapter V, an ionomer (Surlyn) was used as shell material due to its low T_c and high toughness. It is demonstrated that PC@Surlyn core-shell filament leads to improved dimensional accuracy and impact resistance in comparison to the parts printed from monofilaments. Due to the low Tc of the shell, interdiffusion at layer interface can be promoted due to slow crystallization. Additionally, the shell polymer contains ionic functionality to further improves the interfacial bond strength as the ionic content forms aggregates across the interface as physical cross-links. It is also demonstrated that the immiscibility between the core and the shell provides an additional mechanism for energy dissipation through local core-shell delamination on impact. Partial core-shell

delamination absorbs energy as well as enable PC cores being stretched like a fiber during impact which significantly improves the impact resistance.

Besides the material design of core-shell filaments for additive manufacturing techniques, development of functional elastomeric films utilizing another advanced manufacturing technique, roll-to-roll (R2R manufacturing), is reported in Chapter VI. Continuous roll-to-roll (R2R) processing has been actively explored for the manufacture of a variety of emergent technologies, such as polymer photovoltaics[64], flexible electronics[65], smart packaging[66], and functional films[67,68], due to its potential for high production rates and low costs. In previous works from Cakmak's group, an advanced functional R2R film processing line[69] which includes electric field[70–72], magnetic field[73,74] and thermal gradient treatment zones[75] for field assisted assembly of preferential alignment of particle and microphase, is successfully developed. In Chapter VI, we present a scalable R2R process to fabricate elastomeric films with tunable piezo-resistivity through the use of magnetic field zones of the R2R line to align commercially available nickel (core)@silver (shell) particles (Ni@Ag) in a polydimethylsiloxane (PDMS) matrix. The application of the external magnetic field leads to alignment of the particles into long chain structures that are orientated with long axis along "Z"(thickness) direction of the film. The Ni@Ag particles in these chains are either in loose contact with adjacent particles or fully separated from the closest particle with a thin gap exist between particles.

As a result, the PDMS/Ni@Ag films exhibit piezo-resistivity behaviour along thickness direction because a pressure applied to this structure can increase the connectivity of the particles, resulting in an increase of electrical conductivity through Z direction. It is also found that during compression, electrical resistivity significantly only when the applied pressure become larger than a critical “threshold” pressure. This threshold pressure can be modulated from 0 kPa to 70kPa by changing the Ni@Ag particle loading. The ability to use commercially available Ni@Ag, low-cost materials to generate tunable pressure sensors through a simple scalable R2R fabrication approach could be enabling for a range of applications for stretchable, flexible, and wearable electronics.

CHAPTER II

LITERATURE REVIEW

2.1. 3D-Printing

Three-dimensional printing is a process of building a three-dimensional geometry by successive addition of materials under computer control. Until present times, 3D-printing is often used as a synonym for additive manufacturing. Conventional manufacturing techniques build a 3D object either through cutting material off from a solid block (subtractive manufacturing, Figure 2-1A) or via shaping liquid or pliable raw materials using a rigid mould followed by the solidification of the materials (molding, Figure 2-1B). In contrast, 3D-printing or additive manufacturing (Figure 2-1C) builds a 3D structure successively through either deposition of materials in free space or selectively solidification of raw materials in a tank. Without the need for a specialized mould or cutting tools, additive manufacturing or 3D-printing technologies can quickly turn a complex computer aided design (CAD) 3D model into physical objects on demand.

By providing the ability to rapidly build complex structures on demand, 3D-printing technologies are widely used to make products that are costly or impossible using conventional manufacturing processes. One example of application is to fabricate personalized medical device to fit individual patient. Hospitals uses 3D-printing to build models to assist surgery strategy planning[76]. 3D-printed patient-specified tracheobronchial splints shows promising results of mitigating tracheobronchomalacia because they accommodate the airway

size of individual patient.[12] Additionally, due to the advantage in making complex structures, 3D-priting are also used to biomedical scaffolds[15–17], micro fluidics[18–20] and autonomous robots[21,22].

In a typical 3D-printing process, the first step is to virtually slice a 3D-model (usually in STL format) created either with computer aided design (CAD) software of 3D-scanning is into multiple thin cross-section, then the software designs the printing path and support structures for overhang part of the object. Then 3D-printer builds the object using a layer-by-layer approach based on the virtual layers and printing path planned by the software.

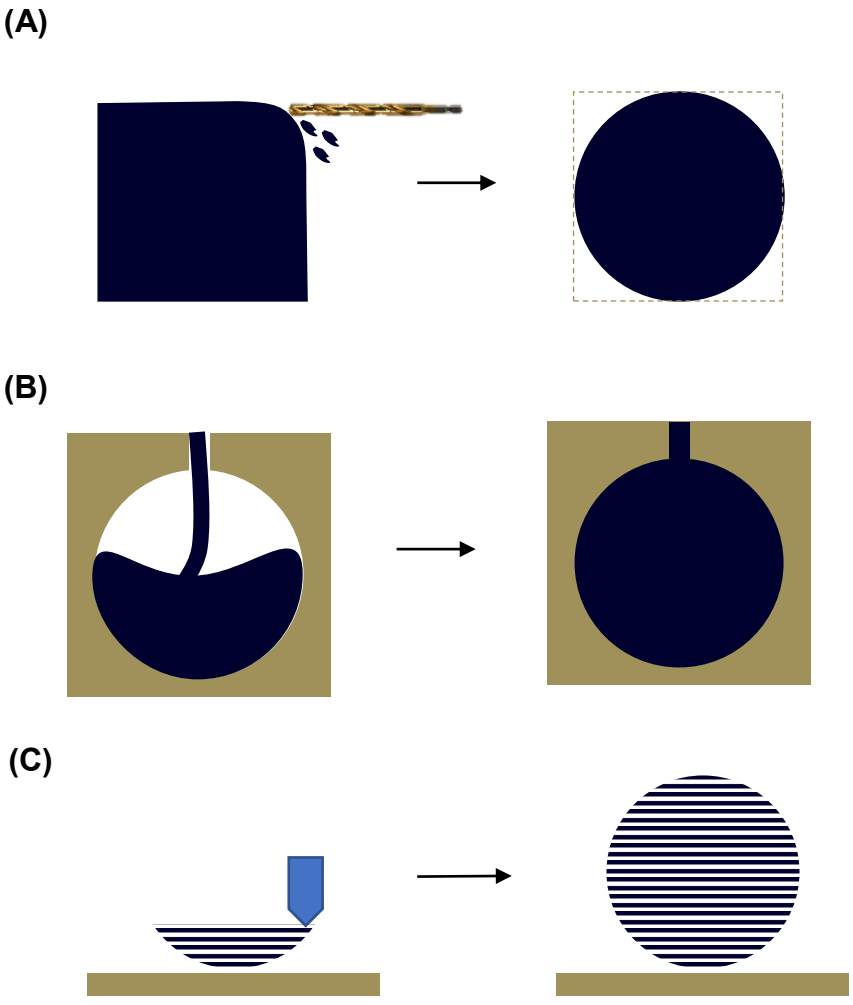

Figure 2-1 Schematic that compares (A) subtractive, (B) moulding, (C) additive manufacturing techniques

Until recently, ASTM/ISO 52900[1] has grouped additive manufacturing technologies into several different categories which include binder jetting, direct energy deposition, material extrusion, directed energy deposition, powder bed fusion, sheet lamination, and vat photo-polymerization. However, the term "*3D-printing"* is generally used when the processes are associated with machines that are low end in price or capability[1], and most 3D-printing technologies use polymers as feedstock. Due to the broad range of properties of polymers[77–80], various types of polymers have been used in 3D-printing techniques. Several reviews[81–83] have addressed the scope of different 3D printing techniques that are used to produce polymer objects. Table 2-1 summarizes the most widely used 3D-printing techniques for polymer materials. Based on the feedstock type or solidifcation mechanism, the techniques can be classified into three major caterories, vat-photopolymerization, extrusion, and powder bed process.

Table 2-1 Categorized 3D-printing techniques with technical characteristics (chart is partially reproduced with permission from Chem. Rev. 2017, 117, 10212−10290)[83]

Categorized techniques	Typical resolution	Typical materials	Advantages	Disadvantages
SLA	25−100 μm	acrylates/epoxides	excellent surface quality and precision	Limited mechanical properties
CLIP	75 μm	acrylates	High build speed	low viscosity resin required

Multiphoton lithography	0.1−5 μm	acrylates	Very high resolution	Low build speed, limited materials
SLS	50−100 μm	PA12, PEEK 25	Best mechanical properties	Rough surfaces; poor reusability of unsintered powder
Multijet	25 μm 10	acrylates	Fast; allow multi-material printing	Limited mechanical strength
FFF	100−150 μm	ABS, PLA, PC, HIPS	Inexpensive machines and materials	Rough surface; high-temperature process
Direct writing/3D Dispensing	100 μm to 1 cm	thermo-plastics, composites, photoresins, hydrogels, biomaterials	Broad range of materials	Rough surfaces; narrow viscosity process window

Vat photopolymerization 3D-printing uses laser or digital light projections to selectively photopolymerize photocurable liquid resins in a bath. The photocurable liquid resin used in this process can be cured rapidly when subjected to incident light, while the resin in the dark region remains to be liquid. Through spatially controlled solidification of liquid resin by photocuring, a 3D object can be created in the bath.

The first 3D-printing technology-Stereolithography (SLA) was developed by 3D Systems (original UVP inc.) in 1986[84]. In SLA (Figure 2-2A), a computer controlled movable spot-beam of UV light shines and scans at the liquid surface of a bath of UV-curable resins to generate a solid layer of the cross-section of the workpiece. The workpiece is then moved away from the liquid surface by the thickness defined for one layer, and the next layer is generated and joined to the preceding layer in the same manner.

Although the original patent[85] describes various apparatus configuration for implementing SLA, the top-down approach as shown in Figure 2-2(A) is increasingly being used. In this setup, light is targeted on a transparent and non-sticking window at the bottom of the resin bath. The printing starts by dipping the platform into the bath and building each layer near the window.

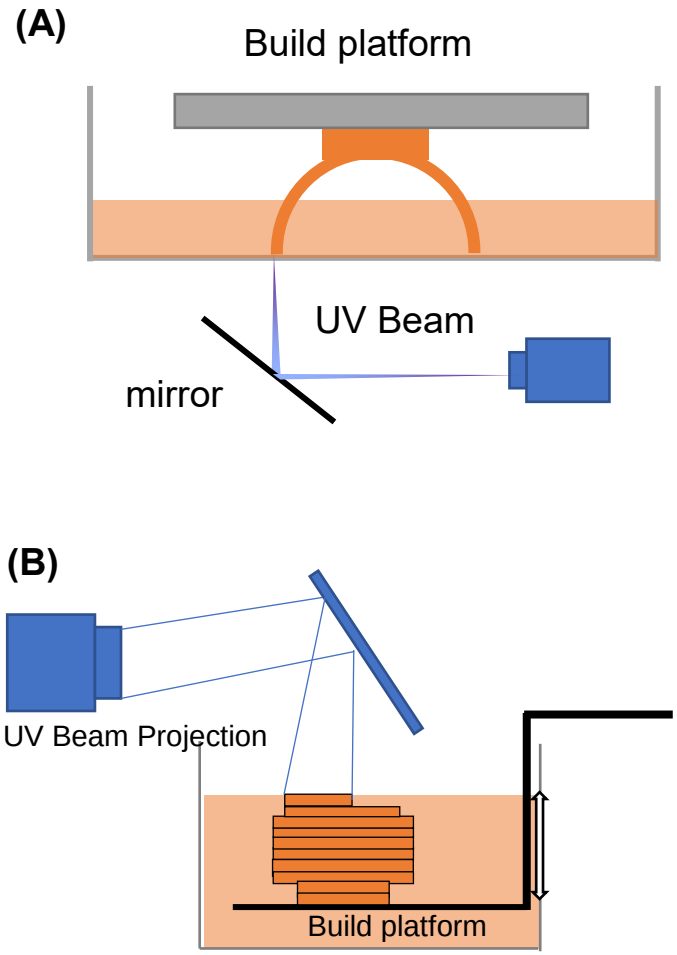

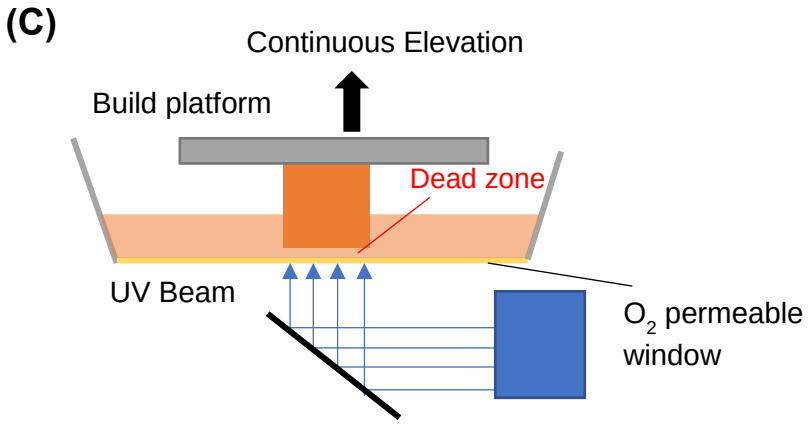

Figure 2-2 Schematic representation of a photopolymerization type 3D-printing setup: (A) stereolithography; (B) digital light processing; (C) continuous liquid interface processing.

The major advantage offered by SLA is its high resolution. SLA printers can reach a resolution of 20μm or less[86]. The high resolution is due to the high precision of UV laser control. Jacobs et al.[87] has reported an empirical equation that relates the cure depth(C_d) and cures line width(L_w) to the maximum light exposure(E_{max}), penetration depth(D_p) of the resin, laser spot diameter(B), and critical exposure time for polymerization initiation(E_c):

$$C_d = D_p \ln(E_{max}/E_c);\ L_w = B\sqrt{C_d/2D_p} \quad (2.1)$$

According to the model, the resolution of the printed objects is also determined by kinetic of the curing reactions and optical properties of the resin. To formulate a resin for SLA process, several major components[61] are needed including monomer/oligomer, diluent, chain transfer agent, and photo-initiator. Monomer and oligomer are the major component of the formulation, which can

undergo polymerization or crosslinking reaction. Acrylate-based monomers were originally used in this process because of its low viscosity, fast reaction rate and tunable thermal or mechanical properties[88]. However, their high density change upon reaction has been a major concern as shrinkage can induces severe distortion after curing[26,89]. UV-curable Epoxy based resins offer lower volume shrinkage[28,90] during curing as the ring-opening reaction of epoxy generates a shrinkage of only 1-2%[91,92]. However, it is also found that the epoxy resins have a slower curing rate as compared to acrylate-based monomers. Other monomer/oligomer types such as photo-crosslinkable poly(propylene fumarate)[16], polyethylene glycol[27] and polylactic acid[9394] were also developed for 3D-printing of biomaterials[95].

Photo-initiators are also key components in photopolymer for 3D-printing. A photo-initiator converts into reactive species on the absorption of the energy of the incident UV-light. Besides UV initiating, two photons induced polymerization(2PP) has also been applied to 3D-printing[96]. In 2PP, a photo-initiator, which absorbs only one UV photon to initiate, needs to absorb two near-IR photons at the same time and converts into free radicals that initiate polymerization. Because two-photon absorption occurs only when the spatial density of the near-IR photons is high and polymer resin is transparent to near IR light, the photopolymerization happens only at the focal point of the near-IR laser and resins in out-of-focus positions are not affected by the near-IR transmitted through. This allows 2PP process to produce parts in a direct-writing manner with resolution superior to other approaches as illustrated in Figure 2-3 .[97,98]

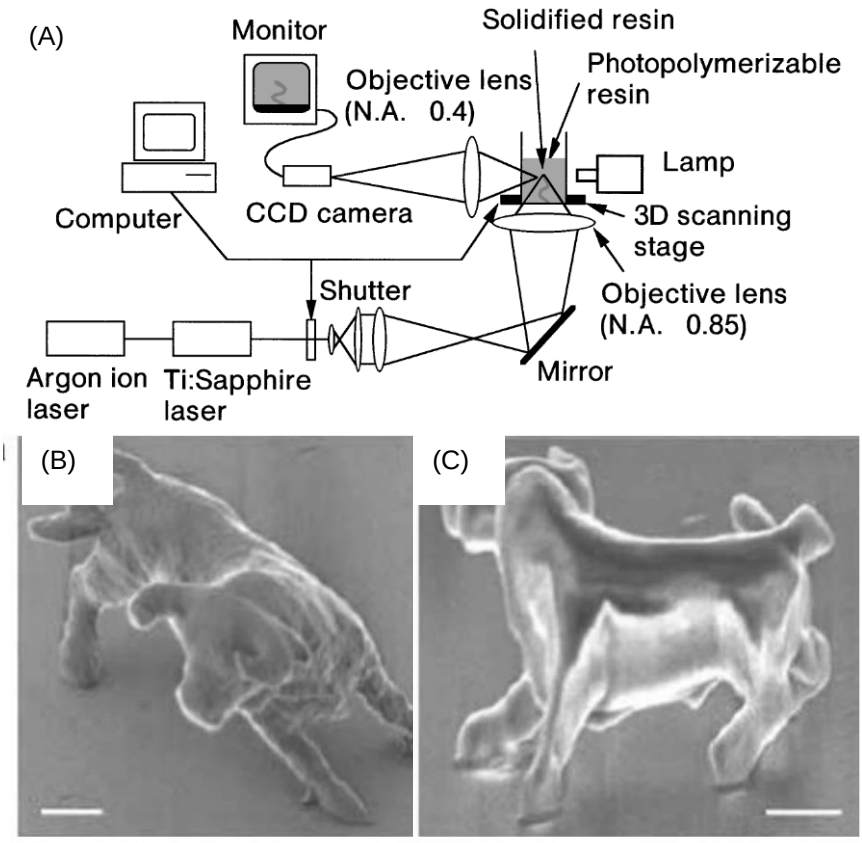

Figure 2-3 (A) schematic shows the optical system for two-photon polymerization 3D-printing(reproduced with permission from[96]); (B), (C)Scanning electron microscopy (SEM) images of 3D microstructures produced by using two-photon polymerization, the length of the scale bar is 1μm. (reproduced with permission from[99])

When the viscosity of the resin is high, diluents might need to be added into the formulation to tune the viscosity to an acceptable level for printing. For example, in high-viscosity ceramic fillers suspended resins[100] for SLA 3D-printing, low-viscosity 1,6-Hexanediol diacrylate is used as diluents to lower the viscosity which also reacts with the photopolymers during curing.

Based on the concept of photopolymerization, newer methods including digital light processing(DLP)[101,102] and continuous liquid interface production(CLIP)[103] have been developed. Instead of using a spot-beam light to cure one element at a time, DLP (Figure 2-2B) and CLIP (Figure 2-2C) project a two-dimensional pattern onto the liquid resin surface to photopolymerize an entire layer simultaneously, except CLIP proceed the curing process continuously. As such, DLP and CLIP can potentially produce faster than SLA. As shown in Figure 2-2C, at the bottom of the CLIP 3D-printer is an oxygen-permeable UV-transparent window near which photopolymerization is inhibited and a 'dead zone' is created between the window and the objects. A continuous sequence of UV-projection is projected through window and cures the workpiece above the dead zone as it is continuously drawn out of the resin bath. A part can be drawn out from the bath at a vertical speed of hundreds of millimeter per hour, whereas the speed of SLA are restricted to a few millimeter per hour[103]. Because the process is continuous, the speed of printing or resolution is not affected by layer slicing thickness.

Materials jetting, or ink jetting,[104,105] techniques also use photopolymerization process to produce physical 3D structures. In this process (Figure 2-4), an inkjet heads with an array of microscopic orifices deposits photo-curable ink droplets onto a build platform, and then UV-light scanned over the workpiece to cure the deposited layer. Stratasys has commercialized this technique in their Polyjet[106] systems which are capable of depositing

multiple different photopolymers simultaneously by using an inkjet head with an array of microscopic orifices. This unique characteristic enables users to combine multiple materials into one part in a single print[107].

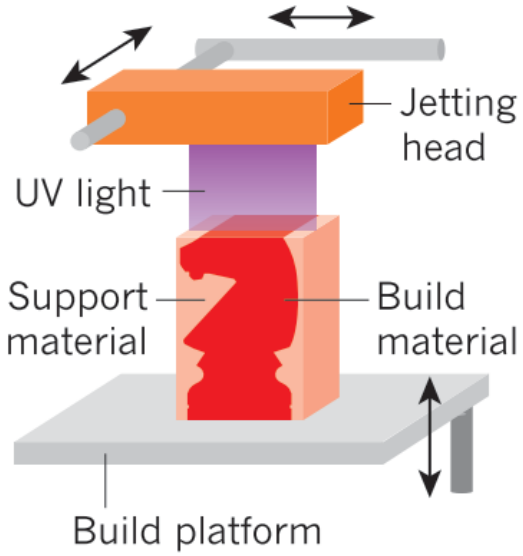

Figure 2-4 Material jetting process consisting of jetting head, UV-light source attached to a movable print-head. (reproduced with permission from [82])

Selective laser sintering (SLS), which was introduced[30] soon after SLA shares its mechanism of using incident light-beam to locally solidify feedstock materials. Instead of using a UV light beam, SLS utilizes high-energy rastering laser to locally melt and bind powder materials at the surface of the powder-bed[1]. As shown in Figure 2-5, For each layer, the laser beam scans the powder-bed to join powders together within desired cross-sectional regions. Then more powder is applied for the successive layer by a blade or roller. High energy laser beam used in this process allows the machine to process a wide range of materials that can be melted by laser including metal[108], ceramic[109] and thermoplastics[29,31,110].

Similar powder-bed feeding process was also used in 3D powder binding technology invented by Sachs et al. at MIT.[111] Instead of using laser to melt and fuse powders together, 3D powder binding uses an ink-jet print head to dispense binder liquid to selectively bond powders together.

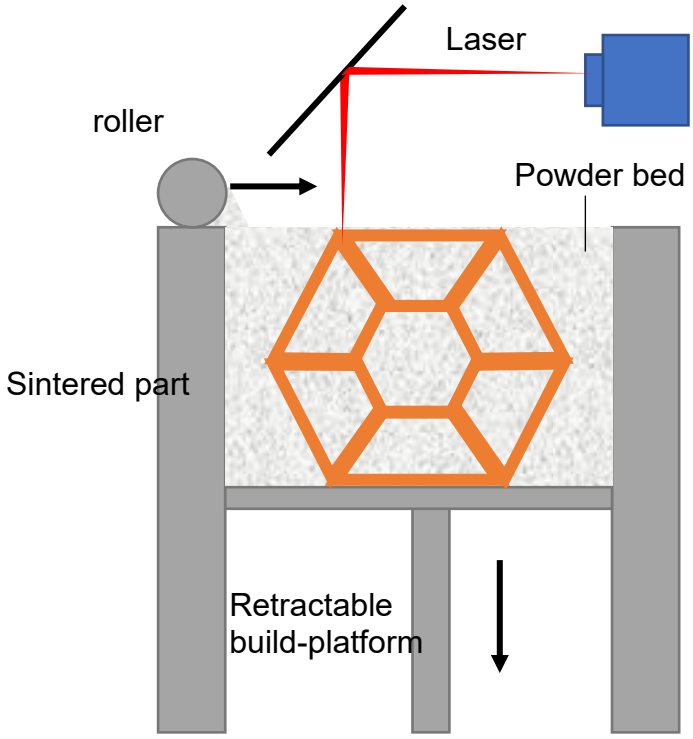

Figure 2-5 Schematic illustrating the selective laser sintering (SLS) uses a laser beam to locally melt and bind powders on a powder bed.

Material extrusion 3D-printing technique are processes in which material is selectively dispensed onto a build-platform as a continuous filament through a nozzle or orifice. The earliest type of this approach is Fused Filament Fabrication (FFF), originally known as Fused Deposition Modelling (FDM) developed by Stratasys, in which a continuous thermoplastic melt filament is deposited onto a build-platform layer-by-layer to build a 3D objec. More recently,

(Figure 2-6 A)direct ink writing technique was introduced in which a nozzle deposits viscoelastic fluid under ambient conditions[23,112]. The viscoelastic materials used in this process are tailored to be able to flow through the nozzle during extrusion when pressure is applied and then freeze rapidly after deposition to keep its shape. Therefore, gels which exhibit a yield stress and a shear thinning flow behaviour beyond the yield point (τ_y) are often used in this process. Its rheological property can be described as follow[113,114]:

$$\tau = \tau_y + \mathrm{K}\dot{\gamma}^n \tag{2.2}$$

where τ is the applied shear stress, $\dot{\gamma}$ is the shear rate, K is a constant and n is the power law index(n<1). To induce flow, a stress $\tau > \tau_y$ is applied in the nozzle so the fluid is extruded through the nozzle. When they exit the nozzle, the applied stress is relieved, and it retains its shape because τ_y is larger than the stress induced by gravity.

Hydrogels can often be applied in direct ink writing techniques[25], due to the unique combination of properties such as biocompatibility and tunable rheological properties.[115,116,123–127,116,116–122] Often, additional post-printing steps such as thermal curing[24,128] or photopolymerization[25] is required for fully solidify the printed part.

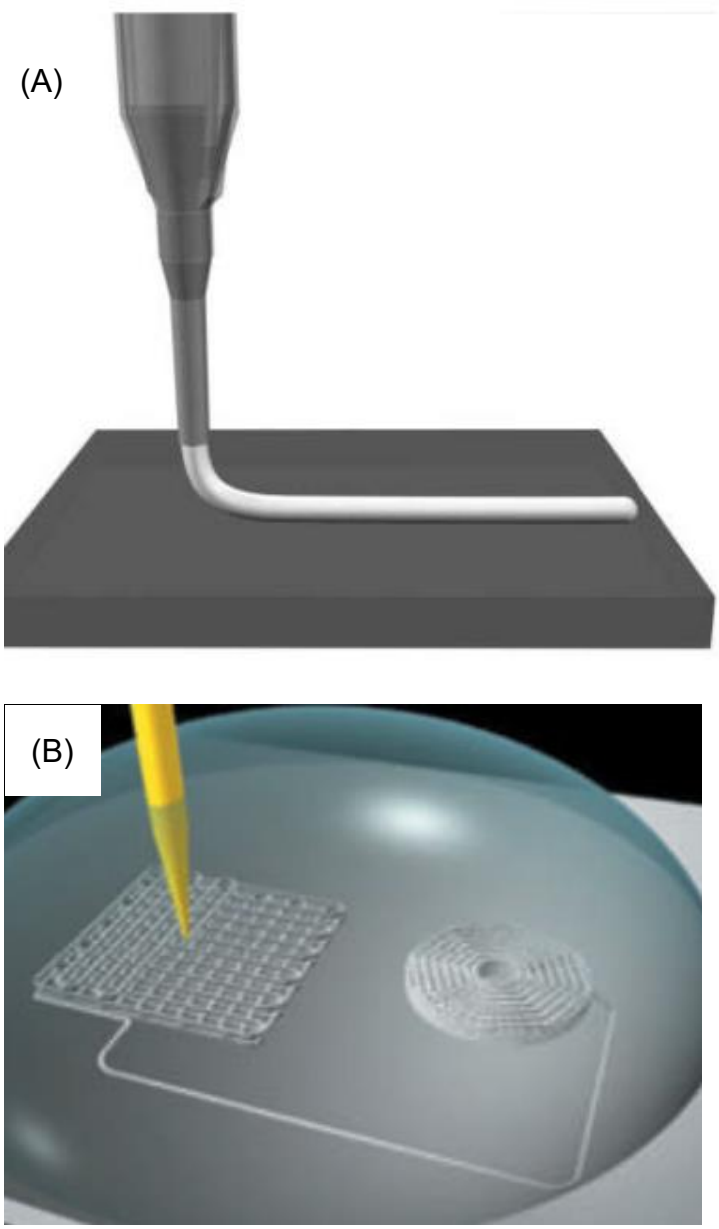

Figure 2-6 (A)Schematic illustration of direct ink writing.; (B)Schematic illustration of 3D-dispensing in liquid media (Adapted with permission from A-[23], B-[112])

Similar to direct ink-writing, 3D dispensing[17] also uses a nozzle to deposit liquid materials in the form of continuous filament. In contrast, the ink is deposited into a liquid media instead of in free space (Figure 2-6 B). In 3D-dispensing, the ink can be formulated to be able to rapidly react with the liquid

media and solidify. For example, moisture curable silicone based on acetoxysilanes was used for 3D dispensing in a water medium[17]. Mixing of oppositely charged polyelectrolytes can generate complex coacervates that precipitated from the aqueous solution[115,129,130]. Polyelectrolyte complex formation process can also be applied in 3D-dispensing to produce 3D objects via depositing polyelectrolyte solution into an alcohol/water reservoir which induces coagulation of the complex [112]. Besides a co-reactive system, by matching the densities of the liquid media with the ink, the weight of materials is compensated by buoyancy, so the printed structures would not collapse under gravity before solidification.[131] Soft granular gels made from polymeric microparticles have also been used to create media for 3D dispensing[132]. The special jamming/unjamming transition undergoes in these microparticles allow them to smoothly transform between liquid and solid. The granular gels fluidize to as the printing material is extruded through a nozzle and then quickly solidifies to trap the injected material in place. Because the jamming/unjamming transition is reversible, the track left by the moving nozzle is soon filled with gel particles, allowing the nozzle to pass the same region repeatedly. Most importantly, since the injected materials can be supported by the gel medium, this technology allows liquid materials requires long-time curing time such as thermal curing PDMS to be cured after printing

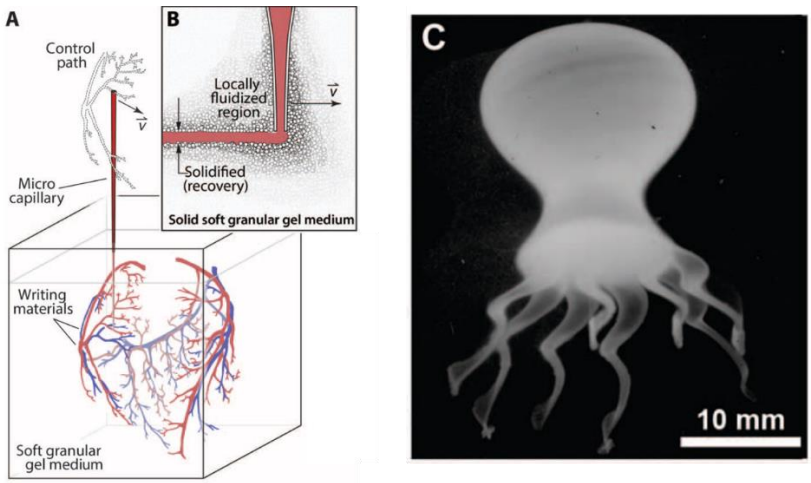

Figure 2-7 (A) microscale nozzle dispenses a complex pattern of liquid materials into the granular gel medium without the need for supporting structures or immediate solidification; (B) As the nozzle moves, the granular gel locally fluidizes and the rapidly solidify to trap the injected materials; (C) An polymerized octopus model injected and solidified in the gel medium. (adapted with permission from [131])

2.2. Fused Filament Fabrication

In late 1980s, Scott Crump[133] of Stratasys Ltd developed the 3D-printing technique with the brand name Fused Deposition Modelling, which is later known as Fused Filament Fabrication(FFF) or Material Extrusion Additive manufacturing(AM). Fused Filament Fabrication is one of the most popular 3D-printing techniques to produce plastic objects because it uses inexpensive thermoplastic filaments as feedstock which can be fabricated in large-scale at low cost. Thermoplastic filament is safe to be used in an office-friendly environment.[32] In addition, multiple print-heads can be incorporated into one FFF device to enable printing of temporary supporting structure, multiple build materials[134] or multiple colours[134].

Besides the safe and low cost of feedstock, FFF 3D-printer is also the most inexpensive type of 3D-printer due to the simplicity of its machine structures. Low-price 3D-printer can be purchased for a price lower than $200 and the simplicity of its construction also help this technique gain its popularity among the DIY community.[135] Additionally, thermoplastic filaments used in FFF do not contain sources of hazards such as volatile chemicals used in vat photopolymerization AM or the high-energy laser used in SLS, FFF 3D-printers can be placed in an office area. Due to its low cost and advantage in safety, FFF has become one of the most widely used 3D-printing techniques.[92]

2.2.1. FFF 3D Printers

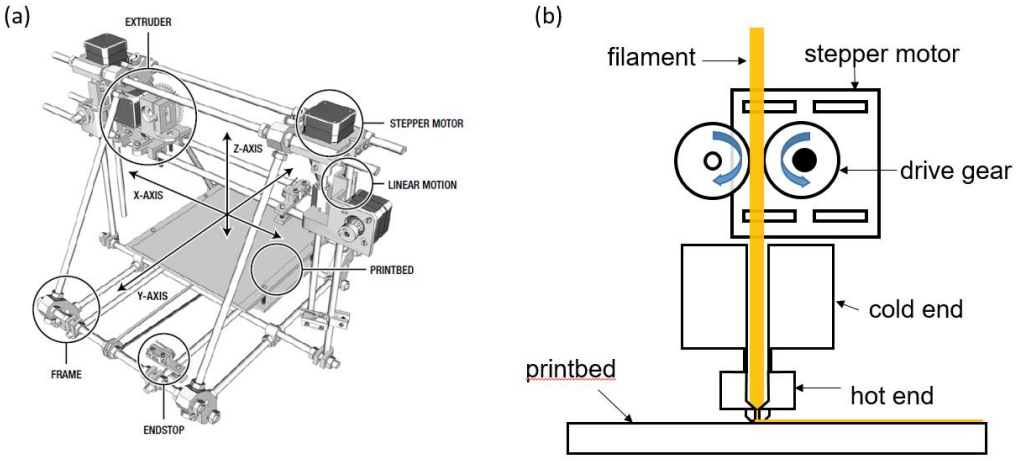

Figure 2-8 (a) schematic that illustrates the structures of a FDM 3D printer(adapted with permission from[136]); (b) schematic that illustrates the structure of an FFF 3D-printer extruder as it deposits melt strand onto a build-platform

Most FDM 3D printers are constructed similarly to a 3-axis computer numerically controlled (CNC) milling machine, where the workpiece and the cutting tool along three normal axes (XYZ) under computer control. Desktop

FFF 3D printers utilize 3 independent stepper motors to control linear motions along three orthogonal axes (X-, Y-, and Z-) as schematically shown in Figure 2-8(a). In a typical FFF 3D-printer setup, the extruder is mounted onto a gantry that moves in X-Y plane under the control of two stepper motor. A build-platform, alias print-bed, lowers down vertically (Z) under computer control every time the extruder finishes the printing of a layer. 5-axis FFF 3D-printers were also built to enable printing of curved layers.[137] It is demonstrated 5-axis machine can significantly improve the printing efficiency and mechanical properties of parts when print an curved shell-like structures. [138,139]

At the heart of an FFF 3D printer is the filament extruder where filament is melted and extruded. Unlike traditional extrusion process which uses pelletized thermoplastic feedstock, FFF extruders use a self-extruding filament feed mechanism. The extruder used in FFF 3D printer is generally composed of two key elements-a filament drive and a heated nozzle also known as liquefier or hot-end. The filament drive is composed of a stepper motor and two pinch rollers. As shown in Figure 2-8(b), the stepper motor is connected to one of the pinch rollers, so the controlled rotary motion of the pinch rollers feed polymer filaments into the liquefier. Typical pinch rollers are constructed with grooved or teethed surfaces, so they can apply enough friction to push the filament to flow through the liquefier without slippage at the rollers. The liquefier is usually a metal block with internal flow channels built for the feedstock to pass through. Disposable nozzles are used in connection liquefiers which facilitate easy replacement and switching between different orifice sizes for various resolution and build-speed needs. Coiled or cartridge heaters embedded into the liquefier

are used in conjunction with a thermocouple to maintain the liquefier at an elevated temperature. Sometimes, a cold-end is used to connect the liquefier to the extruder and thermally insulates the liquefier from the other parts of the machine, preventing filament softening beyond liquefier and overheating of the device.

As the solid filament enters the liquefier, it is rapidly heated and transforms into a viscoelastic polymer melt. The incoming solid section of the filament pushes the molten polymer out of the nozzle and deposits the melt onto a build-platform or the preceding layer in the form of a continuous thin strand. To prevent the object from coming off the platform in the process, most build-platform are installed with blanket heaters to maintain at an elevated temperature favourable for adhesion. Glass platforms are usually installed in FFF 3D-printers because it ensures a smooth finish of the bottom layer. Kapton tapes[140] are often applied to glass build-platform which maintain good adhesion to ABS plastics when print-bed is at 80°C-130°C.[141][142] Heated build platform helps the printed object to adhere strongly to the platform because it mitigates the temperature gradient between nozzle and build-platform, preventing internal stress induced warpage deformation resulted from uneven cooling.[143] High-end FFF 3D printer such as Stratasys F123[144] conducts the printing inside a temperature controlled build-chamber to mitigate the warping distortion. In addition, build-chamber filled with desiccant also helps to prevent the filament from absorbing moisture as moisture content in filaments can lead to degradation of the polymer chains and other problems[145].

2.2.2. Printing Parameters

Before printing, users need to use slicing software to slice the 3D model into multiple horizontal layers. Subsequently the software generates the toolpath for filament deposition and calculates the amount of materials to be extruded. The strategy of slicing and toolpath generation plays an important role in determining the build-time, dimensional accuracy and resolution [146]. Multiple parameters need to be set in the FFF 3D printing including temperature, speed, filament dimension and inflll strategy. It has been reported that these printing parameters significantly influence the mechanical properties and resolution of the final product[42,57].

Figure 2-8A shows the temperature and speed parameters that are commonly controlled in FFF 3D printing. Extrusion temperature (T_{ext}) is the temperature of the liquefier which is dependent on the thermal and rheological properties of the filament materials. T_{ext} must high be enough to transform the solid filament into viscous melt within the liquefier, therefore, T_{ext} must be well above the T_c or T_g of the filament polymers. Too low a T_{ext} might lead to incomplete melting or overly high viscosity of the polymer. Insufficient extrusion or buckling of filaments happens as the stress exceeds the strength of solid filaments or friction applied by pinch rollers[147]. The selection of build-platform temperature is dependent on the material and other printing parameters. High T_{bed} facilitates the polymer melt to stick to the build platform during deposition of the first layer and mitigates temperature vertical temperature gradient, preventing warping distortion.[36141,148] However, overly high T_{bed} could lead to softening and melting of the first several layers, resulting in deformation of the

bottom under the weight of subsequent layers. Printing speed(v) is the rate at which the extruder moves in the x-y plane and the machine controls the feed rate of the filament(V) according to the relation: $V = v \times A$ where A is the cross-sectional area of the filament.

Figure 2-8B shows the basic dimensional parameter that is controlled in FFF 3D printing. Layer thickness(d) is the thickness of each layer and the extrudate width(w) is the width of each strand. These two-dimensional parameters determine the resolution and surface roughness surface roughness of the printed parts[149]. The lateral resolution of the printed part depends on the width of filament (w). The vertical resolution and surface roughness. The printed part exhibits finer finish and better details as the extruded filaments is thinner (smaller w and d value).[37,149] The range of d and w is limited by the nozzle diameter. Layer thickness must set to be smaller than the nozzle diameter otherwise the strand must rely on the gravity to lay it onto the preceding layer. The width of a extrude filament cannot be smaller than 1.2-1.5 times the size of the nozzle diameter[150] due to the present of die swelling in melt extrusion[151]. Layer thickness of a printed part is controlled by the distance build platform lowers down upon completion of a layer deposition. The extrudate width is controlled by the filament feed speed V following the relationship: $V = v \times d \times w$.

Figure 2-8C shows a rectilinear infill toolpath for printing a rectangular cross-section. Rectilinear tool path is the most commonly used infill strategy in FFF. To print a layer, the extruder typically start with printing a contour around the perimeter of the layer and then infill the interior of the layer by depositing

raster of filaments at a fixed angle θ. Typically, to compensate for the anisotropic properties[40,152] induced by this infill strategy, the next layer usually is deposited transverse to its preceding layer as shown in Figure 2-9

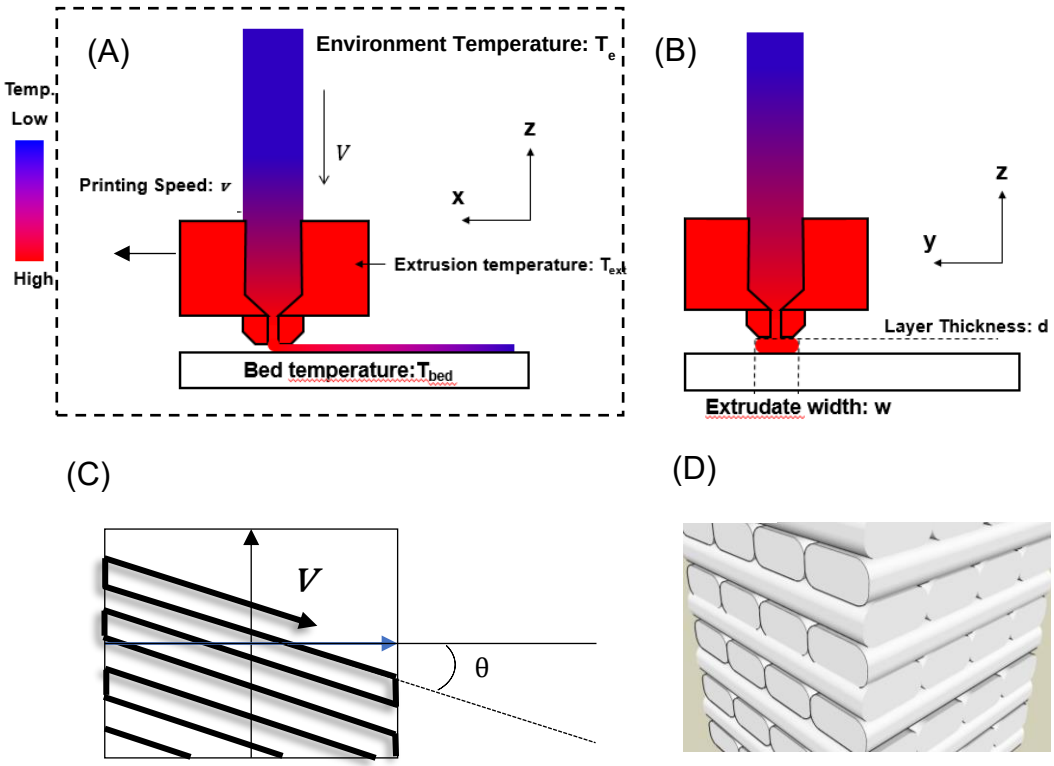

Figure 2-9 Schematic Illustration of printing parameters used in FFF (A) side view of an FFF extruder printing in x- direction that illustrates speed and temperature parameters; (B) front view of FFF printing process dimensional parameter; (C) schematic that illustrates a rectilinear infill toolpath at a raster angle θ; (D) 3D model shows the internal structure of an object printed at 0-90° alternating raster angle

2.2.3. Extrusion process

This FFF extrusion process is significantly different from traditional polymer filament extrusion process. In a conventional single-screw extruder, frictional heating from the screw is the dominant energy source to transform the solid polymer to the melt and the screw homogenizes the polymer melt as well as generates significant pressure to drive isothermal melt flow through the die [41]. In an FFF extruder liquefier, the polymer is heated solely by heat convection from the liquefier barrel. Analytical models of heat transfer occurring in the liquefier have been reported are based on either constant heat flux assumption[153] or constant wall temperature assumption[154].

Bellini et al.[153] proposed an approximation of the relationship between exit(T)/entrance(T_i) temperature and heat flow rate based on a constant heat flux assumption as follow:

$$q = (T - T_i) \cdot \frac{\rho v A c_p}{2\pi \frac{D}{2} L} \tag{2.3}$$

where ρ is the density of the material, c_p is the heat capacity of polymer, v is the average velocity of the flow, and the cylindrical hot end dimension D (diameter), L (length) and A (cross-sectional area).

Because most liquefiers used in 3D printers are made of a thermally conductive material such as aluminium or brass, Yardimci[154] proposed an analytical model of heat transfer in liquefier based on a constant wall temperature assumption. A hot end with a tubular flow channel (the diameter

of the tube is considered equal to the diameter of filament r_f) can be considered as a cylindrical coordinate ($P(z, r, \theta)$). The non-dimensional solution to the temperature distribution problem is given as:

$$\theta = 2\sum_{n=1}^{\infty} e^{(-\lambda_n^2 z')} \frac{J_0(\lambda_n r')}{\lambda_n J_1(\lambda_n)}, \quad J_0(\lambda_n) = 0, \quad \theta = \frac{T - T_0}{T_2 - T_0} \tag{2.4}$$

where $r' = \frac{r}{r_f}$ and $z' = \frac{\alpha}{V r_f}\frac{z}{r_f}$, V is the filament velocity, α is the thermal diffusivity, λ_n is the root of zero order Bessel function of first kind J_0, and J_1 is first order Bessel function of first kind. Yardimci[154] solved the melt front location z' for $r'=0$ and $T=T_m$:

$$\theta_m = 2\sum_{n=1}^{\infty} \frac{e^{(-\lambda_n^2 z_m')}}{\lambda_n J_1(\lambda_n)} \tag{2.5}$$

This model suggests that, for a hot end with a tubular flow channel, the temperature of a filament is a function of exit/entrance temperature, filament velocity and coordinates r and z. $T = f(T_0, T_2, V, r, z)$

Besides heat-transfer, Bellini et al.[153] has also introduced a flow model of FFF liquefier dynamics to predict the pressure drop in the liquefier which correlates with force needs to push a filament through the liquefier. In this model, the liquefier flow channel is decomposed into three different sections as shown in Figure 2-10.

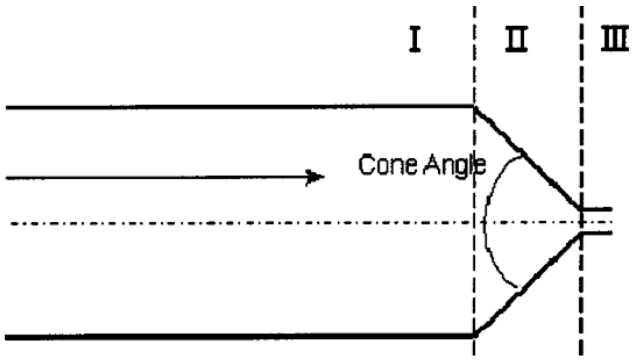

Figure 2-10 Regional decomposition of liquefier flow channel in FFF extruder(adapted from [153]).

Bellini establishes the total pressure drop based on a power-law fluid which follows the relationship: $\tau = (\frac{1}{\emptyset}\dot{\gamma})^n$ where *n* and *m* are material constants, τ is the shear stress and $\dot{\gamma}$ is the shear rate. By incorporating the heat transfer model and an Arrhenius temperature vs. viscosity relation

$$\eta(T) = \exp\left[a\left(\frac{1}{T - T_0} - \frac{1}{T_\alpha - T_0}\right)\right] \tag{2.6}$$

where T_α is a reference temperature and T_0 is the entrance temperature.

$$\Delta P_1 = 2L_1\left(\frac{V}{\emptyset}\right)^n\left(\frac{1/n + 3}{(\frac{D_1}{2})^{n+1}}\right)^n \cdot \exp\left[a\left(\frac{1}{T} - \frac{1}{T_\alpha}\right)\right] \tag{2.7}$$

$$\Delta P_2 = \left(\frac{2m}{3\tan(\frac{\beta}{2})}\right)(\frac{1}{{D_2}^{3n}} - \frac{1}{{D_1}^{3n}})^{n+1}\left(2^{\frac{3n+1}{n}}\left(\frac{D_1}{2}\right)^2(\frac{1}{n} + 3)\right)^n \cdot \exp\left[a\left(\frac{1}{T} - \frac{1}{T_\alpha}\right)\right] \tag{2.8}$$

$$\Delta P_3 = 2L_2\left(\frac{V}{\emptyset}\right)^n\left(\frac{\frac{3n+1}{n}\left(\frac{D_1}{2}\right)^2}{\left(\frac{D_2}{2}\right)^{\frac{3n+1}{n}}}\right)^n \cdot \exp\left[a\left(\frac{1}{T}-\frac{1}{T_\alpha}\right)\right] \quad (2.9)$$

$$\Delta P = \Delta P_1 + \Delta P_2 + \Delta P_3 \quad (2.10)$$

where $D_2,\ D_1,\ L_2,\ L_1$ is the diameter and length of section I and III and β is the converging angle of the conical region. With the ΔP obtained, force applithe ed to the filament for extrusion can be calculated as $F = \Delta P A$ where A is the cross-section of the filament. Then the torque required for the motor to apply is $\Gamma = F/2 \cdot R_r$ where R_r is the radius of the pinch rollers.

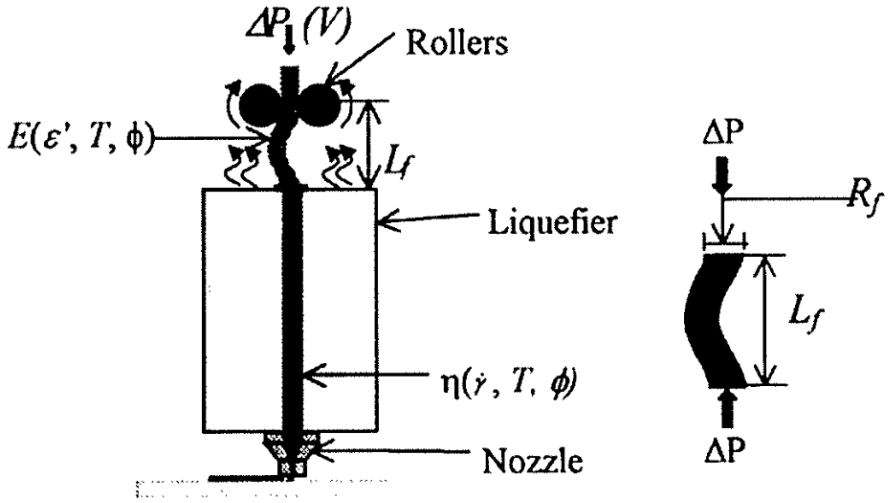

Figure 2-11 Buckling of a filament between the pinch rollers and then entrance of the liquefier.

Excessive pressure drop can lead to buckling of the filament as shown in Figure 2-11. Venkataraman et al. uses a Euler usela analysis for an approximation of the critical pressure for filament buckling:

$$\Delta P_{cr} = \frac{\pi^2 E d_f^2}{16 L_f^2} \tag{2.11}$$

Besides buckling, when force exceeds the traction (maximum friction) between rollers and filament, filament slip off the rollers resulting in insufficient materials extrusion.[150]

2.2.4. Bond formation

Bond formation between printed filaments and layers could play an important role in determining the mechanical properties of the printed parts. The bond formation process in FFF 3D-printing is similar to plastic welding processes[155,156] or often called “healing” of polymer-polymer interfaces. Many studies have been carried out to study isothermal[157,158] and non-isothermal healing process[159,160] at polymer-polymer interfaces that are brought into contact. “Reptation” model proposed by de Gennes[161] and later extended to explain the rheological behaviour of entangled polymers by Doi and Edward[161] considers a polymer chain with length *L* is topologically confined within a tube along at time t=0(Figure 2-12). The chain moves diffuse along the tube in a Brownian motion manner and at time $t=t_1$ one end of the chain escapes from the original tube forming a “minor chain” with length *l*. “Reptation” time t_R is the time it takes for an entire polymer chain to diffuse out of the tube as shown in Figure 2-12 and *l*=L at t= t_R. Based on the reptatiion theory, Yang et al. [162] studied the chain motion at a newly formed polymer-polymer interface. As shown in Figure 2-13. At $t=t_1$, minor chains of with an interpenetration length χ have diffused across the interface. A degree of healing at time

t($D_h(t)$) defined as the ratio of the instantaneous strength of the bond to ultimate bond strength is described as:

$$D_h(t) = \frac{\sigma}{\sigma_\infty} = \frac{\chi}{\chi_\infty} = (\frac{l}{L})^{1/2} = (\frac{t}{t_R})^{1/4} \quad (2.12)$$

This model works well in predicting the isothermal healing of AS4/PEEK in this study and the time for a fully healing is 2450 seconds at 390°C and 4800 seconds at 370°C. It suggests that healing time for entangled thermoplastic melt polymer-polymer interface is highly dependent on temperature.

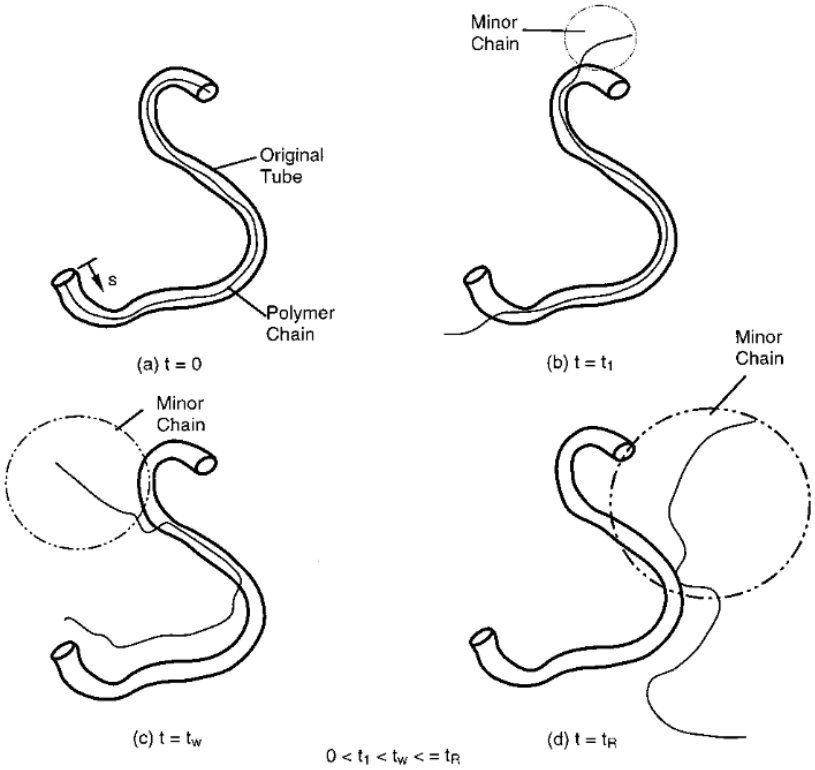

Figure 2-12 Movement of a linear polymer chain in polymer melt as described by “reptation model” (adapted with permission from [162])

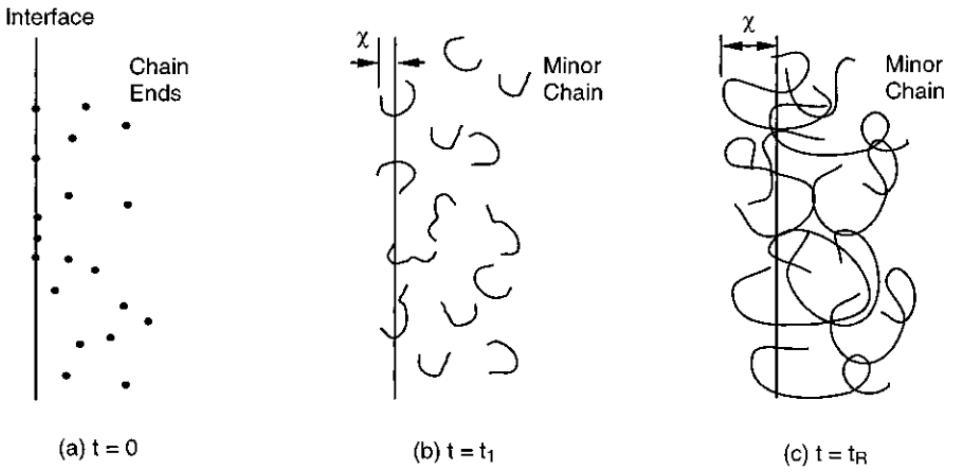

Figure 2-13 Schematic illustrates the process of interdiffusion of minor chains across a polymer-polymer interface that is brought to contact at t=0.

FFF 3D-printing is a highly non-isothermal process. Printed layers solidify well before the subsequent layer being printed onto them. As the melt being extruded out of the nozzle, it encounters air and the cold underlying layer, thus cools down very rapidly. Bond formation process is dependent, in part, on the cooling process. Thomas and Rodriguez[163] performed a 2-D transient heat transfer analysis of a single printed road (W-width, H-thickness), and proposed an eigenfunction expansion solution of averaged temperature over the width:

$$T_{\text{ave}}(x,y,t) = T_{\text{ext}} + \frac{2T_{\text{ext}}}{W}\sum_{m=1}^{\infty}\sum_{n=1}^{\infty}\left(\frac{a_{mn}}{\beta_n}\sin(\lambda_m y)\cos\left(\frac{\beta_n W}{2}\right)\right)e^{-\left(\frac{k}{C\rho}\right)^2\left(\lambda_m^2+\beta_n^2\right)} \tag{2.13}$$

where,

$$a_{mn} = \frac{4T_L^*}{E_m^2 F_n^2 \lambda_m \beta_n}\sin\left(\frac{9\lambda_m H}{2}\right)\sin\left(\frac{\lambda_m H}{2}\right)\sin\left(\frac{\beta_n H}{2}\right) \tag{2.14}$$

$$F_n^2 = \frac{1}{2}(W + \frac{\sin(\beta_n W)}{\beta_n}) \text{ and } E_m = \frac{1}{2}(5H - \frac{\sin(10\lambda_m H)}{2\lambda_m}) \quad (2.15)$$

$$\lambda_m \cot(5\lambda_m H) = \frac{-h}{k} \text{ and } \beta_n \tan(\frac{\beta_n W}{2}) = \frac{h}{k}, \quad (2.16)$$

where *t, C, k* and *ρ* are time, heat capacity, thermal conductivity and density respectively)

By using equation (2.13), temperature histories of filament during cooling were obtained for several different processing conditions as shown in Figure 2-14(A). Reptation time $t_R\ (t_\infty)$ at different temperature were obtained using a WLF model:

$$\log\left(\frac{t_\infty}{558.6}\right) = -\frac{8.86(T - 416.2)}{101.6 + T - 416.2} \quad (2.17)$$

as shown in Figure 2-14(B). By combining equation(2.13), (2.17) with polymer interface healing model in equation (2.12), bond strength development for different extrusion and environmental temperature are calculated and compared with experimental data as shown in Figure 2-14(C).

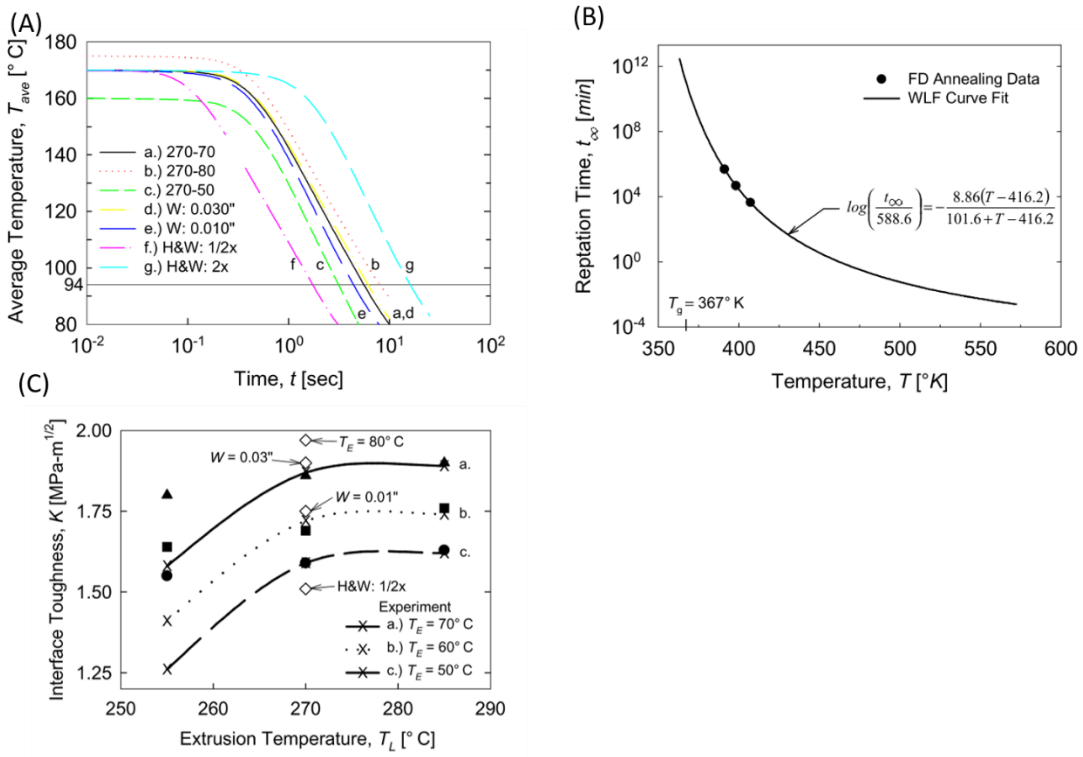

Figure 2-14 (A) Temperature histories of extruded filament for a number of processing conditions; (B) WLF plot showing the temperature dependence of reptation time; (C) Experimental and predicted interface toughness values for different environmental and extrusion temperature. (Adapted with permission from [163])

This model neglected the heat conduction from the print-bed which could be predominant for the printing of the first several layers.

Bellehumeur[60] et al. performed 1D transient heat transfer equation and presented a lumped capacity model, assuming uniform temperature distribution over the cross-sectional area of a printed strand. The analytical solution is:

$$T = T_L + (T_L - T_E)e^{-mx} \quad \text{with} \quad m = \frac{\sqrt{1+4\alpha\beta}-1}{2\alpha}, \quad x = vt \tag{2.18}$$

where $\alpha = \frac{k}{C\rho}$; $\beta = \frac{hP}{C\rho Av}$; A and P is the cross-sectional area and perimeter of a printed strand respectively.

As shown in Figure 2-15, inter-diffusion between two adjacent filaments is significantly limited by this rapid solidification process. A sintering model of coalescence of two Newtonian droplets proposed by Pokluda and co-workers[164], as shown in Figure 2-16(a), has been widely adopted to analyze bond formation in FDM 3D printing[53,60,165]. Sun[57] et al. investigated the bond formation between printed ABS filament by incorporating the sintering model and the lumped capacity cooling model[60]. Figure 2-16(b) shows tat the effective neck growth level (y/a) between two ABS filaments that are printed together at 260°C and 280°C proceeds significantly only above 200°C. Rapids cooling of printed strands allows only limited level of sintering. However, this sintering model assumes the bond formation process happens spontaneously between two fiber-like filaments, whereas real situation is the extruded filament is flattened by the nozzle when it is extruded.

(a)

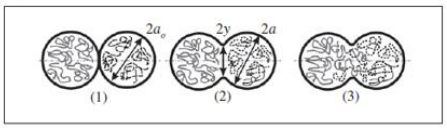

$$\frac{d\theta}{dt} = \frac{\Gamma}{a_o \mu} \frac{2^{-5/3} \cos\theta \sin\theta (2 - \cos\theta)^{1/3}}{(1 - \cos\theta)(1 + \cos\theta)^{1/3}}$$

$\theta = \sin^{-1} y/a$

μ– Viscosity

Γ– Surface Tension

(b)

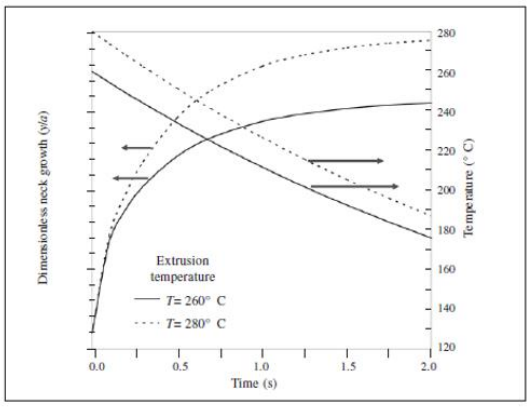

Figure 2-16 bond formation process between two filaments and sintering models of coalescence of two Newtonian droplets; (b) dimensionless neck growth between ABS filaments at different print temperature (adapted with permission from[60]*).*

2.2.5. Mechanical properties

Because of the incomplete healing during the bond formation process, the mechanical strength of objects printed by FDM 3D printer is not comparable to a part made by conventional processing methods such as injection moulding [45–48].

Because FFF 3D printer deposits polymer filament directionally in the x-y plane, the mechanical properties of the printed parts are usually highly anisotropic. FFF manufactured parts show better mechanical strength when the load is applied paralleled to the filament deposition direction than when load is applied normal to printed layers[34,51,166–168169]. Anh[51] et al. investigated the anisotropic mechanical properties of FFF 3D-printed ABS parts. It is reported that when the raster angle is set along the long axis of a tensile specimen, the

tensile strength of the printed tensile specimen can be close to that of an injection moulded part because the load is not applied normal to the weak filament bonding interfaces. On the contrary, when the raster angle is set 90° to the tensile direction, tensile strength is significantly lower. Parts printed with alternating 0°/90° and 45°/45° raster angles show close tensile strength, proving that multiple raster angles can mitigate the property anisotropy in the x-y plane. Because extruder in FFF can only deposit polymer strands in the x-y plane, mechanical strength along z-axis fully relies on the bond strength between each printed layer. Many studies have demonstrated the mechanical strength along z-axis of a printed sample is much lower than along the other directions[40,46,169]. Such inherent anisotropic mechanical properties associated with parts fabricated by FFF have become one major challenge to apply FFF to engineering parts manufacturing.

Additionally, Polymer melts extruded by printer's extruder often could not fills the space within adjacent strands. Due to the circular opening of the printer's nozzle, the extruded strand tends to have an elliptical cross-section as shown in Figure 2-9(B). Unlike, rectangular or hexagonal shaped body, elliptical bodies cannot be perfectly stacked, thus making complete part filling even more difficult. Rezayat et al. [52] studied the relationship between gap size and mechanical performance via finite element analysis simulation. Simulation mapping of strain energy distribution in FDM part for different raster angle and air gaps between each strand shows larger gaps inside the sample could result in a more severe concentration of strain energy when a load is applied. Corresponding experimental data in also confirms that gaps in the samples

result in huge a decrease of mechanical strength of the sample. It also agrees with results of several other experimental studies[45,46,48,50,51] when a gap exists, raster angle of deposited filaments results in more anisotropic mechanical properties of printed parts.

2.3. Magnetic field assisted assembly of particles

Conductive polymer composites are in high demand for applications such as flexible electronics[170–173], conductive adhesives[174–176] and electromagnetic field shielding[174–176]. To achieve electrical conductivity, conductive filers can be added into non-conductive polymer matrix to achieve electrical conductivity[176,177]. In such a system, concentration of conductive fillers must be higher than a critical concentration, percolation threshold, in order to form percolated networks for electron transfer. For systems containing randomly dispersed particles, high loading of conductive particles are often required to reach percolation threshold[178].

Magnetic[179] or electric field[70] assisted alignment of particles in the polymer matrix is an efficient way to in achieving directional percolated particle networks[180]. Application of electric field to samples often requires direct contact with electrodes, which could introduce geometrical constraints to the sample. Moreover, breakdown of the materials has limited the range of operational voltage[181] and utilizing conductive materials in electric field application could impose the danger of electrodes short-circuits[182]. Magnetic field is particularly appealing in assembly of conductive structures as it can be applied in a non-contact fashion and magnetic field is not limited by a upper limit of intensity. Faraudo and his coworkers[183] reviews the magnetic field assembly of

superparamagnetic particles in colloids. In a strong magnetic field, superparamagnetic particles gain induced magnetic dipole as shown in Figure 2-17. The induced dipole drive particles to organize in chain structures aligned along the direction of the external field due to dipole-dipole interaction as shown by the heat map in Figure 2-17 where red colour corresponds to attractive region and green colour corresponds to repulsive regions.

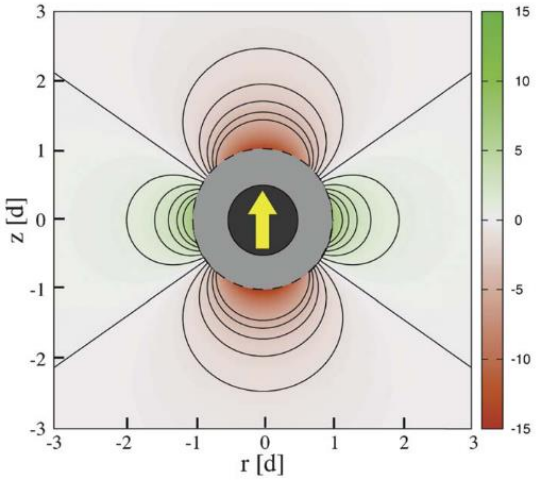

Figure 2-17 Induced magnetic dipole in a superparamagnetic particle. The heat map shows the magnetic dipole-dipole interaction energy experienced by an imaginary test particle induced by the superparamagnetic particle. (Adapted with permission from [183])

Like superparamagnetic particles, ferromagnetic materials can also acquire magnetic dipole in an external magnetic field. However, there is an essential difference between the two materials because ferromagnetic materials are composed of multiple magnetic domains each of which possesses its own direction of aligned magnetic spin. At rest, the spins of different domains are aligned along different direction, therefore, the large-scale

magnetic dipole is cancelled out. The other difference is ferromagnetic material can be permanently magnetized and retain remnant magnetic dipoles in the absence of an external field. Therefore, ferromagnetic particles can align into anisotropic structures in the same manner as superparamagnetic particles in an external magnetic field, except the particles remains to be magnetized after removal of external field. Additionally, due to the low susceptibility of Ferromagnetic materials, ferromagnetic materials don't require high magnetic field for assembly of chain structures. The process can be carried out by using a pair of permanent magnets[184].

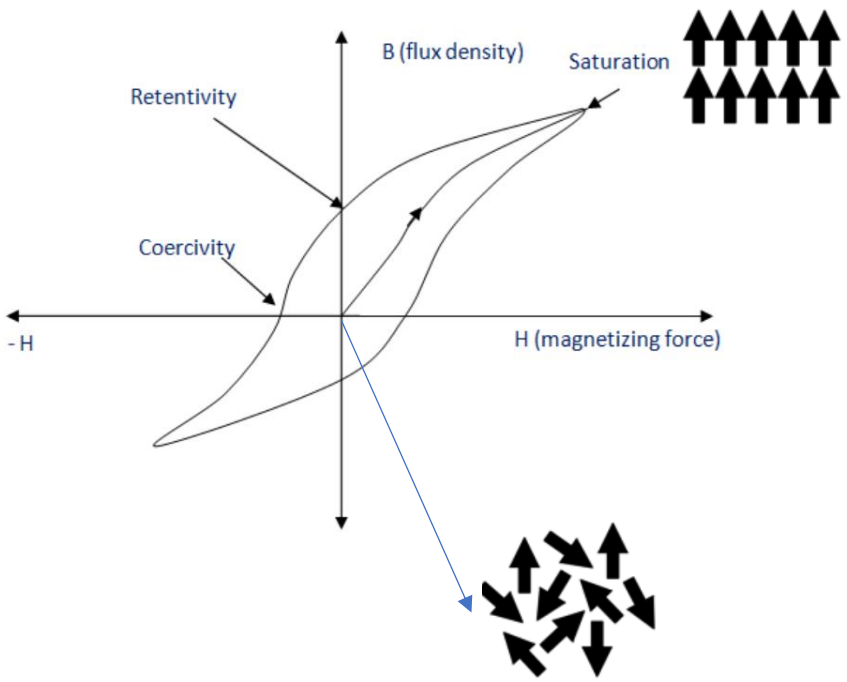

Figure 2-18 Magnetic flux of ferromagnetic particles while magnetizing force is changing.

Because nickel (Ni) is a ferromagnetic material that is also electrically conductive, Ni can be used to achieve anisotropic electrical conductivity using magnetic field assisted assembly. Researchers[185] [152] have studied the process

of magnetic field assisted assembly of nickel fillers in polydimethylsiloxane(PDMS) resin. Figure 2-19 shows the assembly process of Ni particles in low-viscosity PDMS matrix. External field drives ferromagnetic Ni particles to quickly organize into chain structures aligned along the direction of the applied magnetic field, connecting the initially isolated Ni particle aggregates (Figure 2-19-a). Consequently, Electrical conductivity of the system in the direction paralleled to the magnetic field is found to be significantly higher than that of perpendicular direction because the chain structures percolating through the system enables electron transfer along the particle chains. Conductive material coated ferromagnetic particles[179,186] or ferromagnetic particles decorated conductive metal nanowires[180] have also been used to achieve directional conductivity in polymer composites.

In Cakmak's group, the magnetic field assembly of conductive Ni fillers has been applied to the large-scale R2R fabrication of conductive and piezoresistive films[73,74]. Compression along the alignment direction can decrease the gap distance between particles, leading to a reduced the tunneling distance and consequently contact resistance between particles. The pressure sensitivity are found to be controlled by both particle shapes and particle loadings[73]. Besides conductive magnetic particles, by providing the advantage of non-contact application, magnetic field is also used various roll-to-roll processes for application including assembly of block copolymer[184] and carbon materials[187], fabrication of magnetoelastic membrane[188,189].

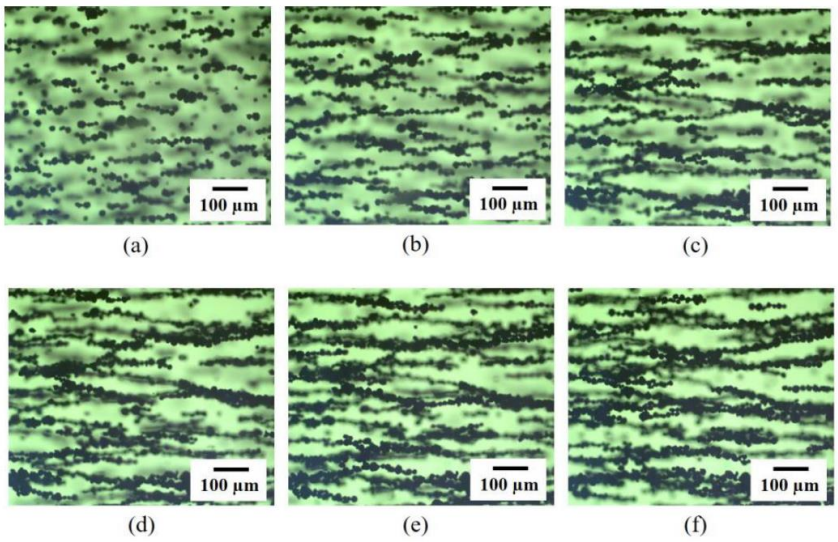

Figure 2-19 Alignment process of spherical Ni particles in the matrix (10 vol. %) with magnetization times: (a) 1 second; (b) 5 seconds; (c) 10 seconds; (d) 15 seconds; (e) 20 seconds; and (f) 25 seconds. (Adapter with permission from [152])

CHAPTER III

COMPLEX FLOW AND TEMPERATURE HISTORY DURING MELT EXTRUSION IN FUSED FILAMENT FABRICATION

(Content in this chapter is partially reproduced with permission from *Additive Manufacturing* 22 (2018): 197-206.[190])

3.1. Introduction

Fused filament fabrication(FFF), or Material Extrusion(ME)[191], is one of the most popular additive manufacturing (AM) techniques due to its low cost and accessibility for the consumer market. FFF is a well-defined AM process where molten polymer is deposited onto the build platform to produce three-dimensional objects [192] through control of the x-y motion of the extruder and z (height) position of the build platform. The process parameters associated with this polymer melt based AM technique can significantly impact the properties and quality of the printed part [147167]. This strong dependency on the processing conditions can lead to high variability in part properties if process control is insufficient [42,48,54,55,193].

At the heart of the Fused filament fabrication (FFF) process is the extruder where the solid filament is melted and deposited. The solid polymer filament is continuously fed into a temperature-controlled heated barrel (often referred to as liquefier or hot-end), generally using two pinch rollers. Conductive heating transforms the solid filament into a viscous melt in the liquefier, while the incoming cold solid filament pushes the melt through the nozzle to be deposited on the build platform. Self-extruding filament acts as both feedstock and plunger

to simplify the design of an ME-AM extruder. This simple design allows the extruder to be integrated with a common desktop CNC gantry for x-y control of the position of the extruder. This ME-AM extrusion process is significantly different from traditional polymer filament extrusion process, such as a single-screw extruder where frictional heating from the screw is the dominant energy source to transform the solid polymer to the melt and the screw homogenizes the polymer melt as well as generates significant pressure to drive isothermal melt flow through the die [41]. Commercial extruders for bulk polymer processing are carefully designed to ensure complete mixing and isothermal properties of the polymer melt prior to exit.

Conversely in an FFF extruder, the polymer is heated solely by conduction from the liquefier barrel. The poor thermal conductivity of polymers leads to a large temperature gradient as the polymer filament is pushed through the extruder. This gradient will lead to complexities in flow and thermal histories for the filament from surface to axis center of the filament that are not present in typical single-screw extruders. This temperature history will impact the properties of the printed part, but we have a limited understanding of the temperature profiles associated with the FFF process. Understanding the extrusion process could facilitate the development of feedstock material, optimization of processing conditions and design of manufacturing hardware.

Due to its importance for FFF, mathematical models associated with roller feeding mechanisms [150], heat transfer [154] and pressure drop [153] in the liquefiers have been proposed to understand the extrusion process in FFF. Bellini et al. [153] estimated the pressure drops in three geometrically distinct sections of a

liquefier by solving the momentum flux balance in each section. This work used a power-law shear-dependent flow to describe the polymer melt and incorporated a thermal convection model based on a constant heat flux and an Arrhenius temperature-viscosity relationship. However, the Arrhenius law is suitable only for linear semi-crystalline above its melting point or amorphous polymers at temperature significantly greater than its glass transition temperature ($T>T_g+100°C$) [194]. An additional limitation is that the power-law model is generally only valid for a limited range of shear rates. An additional challenge in correctly assessing the pressure gradient and flow patterns in the extruder is the temperature gradient induced by conduction from the liquefier that will affect the spatiotemporal flow behavior. The complex temperature profile leads to widely varying polymer melt properties as the filament is melted that makes modeling of the melt flow behavior in the liquefier difficult.

To understand better the temperature complexities, Yardimici *et al.* [154] employed finite element analysis (FEA) [195] simulations to determine the temperature gradient in the extrusion phase of FFF using a computational model. By examining the steady state heat transfer and flow behavior of the FFF extrusion process of poly-ε-caprolactone with FEA, Ramathan et al. [43] demonstrated a much smaller pressure drop than predicted from the mathematical models proposed by Bellini [153]. These results provide evidence of the need to understand the temperature profile in order to accurately model the FFF process. With the development of more functional materials in FFF, such as ABS-Iron composite [196], the melt flow behavior in the FFF extrusion process will require understanding of the temperature-heat capacity relationships, such as that proposed by Marcus et al. [197]. Although FEA can

effectively analyze the fluid dynamics and the heat-transfer when boundary conditions are known, there are other complexities in the FFF process that could lead to discrepancies between the simulated results and the actual process. Notably the abrupt changes in physical properties at melting point or T_g, such as heat-capacity, density and rheological properties, will occur as the filament enters the liquefier, which can lead to challenges in the convergence of the FEA. In addition, as discussed previously, the Power-law model, which is commonly used in FEA to describe the flow properties, works only for a limited range of shear rate and temperature. Moreover, the air gap between the filament and the barrel at liquefier entrance complicates boundary conditions in FEM for examining the polymer flow for the FFF process. Carefully understanding the temperature profiles for FEA could help to refine the properties of FFF fabricated parts, such as residual stress [38], part distortion [55] and mechanical behaviors [54,198,199].

In order to better understand the FFF process, there has been several experimental studies in this area, which include in-situ monitoring of strain and temperature distributions during the FFF melt deposition on a platform [200]. Similarly, infrared imaging [201] and thermocouples (TC) [57] have been used to monitor the cooling and re-heating during the melt deposition process as the molten fibers are deposited. However, the melt flow behavior of the polymer in the FFF extruder has not been reported experimentally to the best of our knowledge.

In this work, we present an experimental method to analyze the flow behavior and temperature history during the extrusion process for FFF. To

visualize the flow, inorganic pigments are selectively included in the filament as flow indicators to illustrate the flow history of the polymer during the extrusion process. The pigment distribution is tracked both in extruded filament as well as the filament remaining in the extruder nozzle using both optical microscopy and X-ray micro computed tomography (MicroCT). The flow profiles can be rationalized through *in-situ* real-time temperature measurements during filament extrusion, which uses embedded ultra-fine thermocouples (TC) in the filaments. These measurements provide insight into the flow and temperature evolution through liquefier during FFF printing, which can be used to help refine models to better predict the properties of additive manufactured parts with FFF.

3.2. Material & Methods

3.2.1. Materials

The polymer was in this study was a bisphenol-A polycarbonate (PC) (Covestro Inc., Makrolon 3208). Prior to any melt processing, PC pellets (as obtained from Covestro, Inc.) or PC filaments were dried in a vacuum-oven at 110°C for 12 hours to remove residual water. This water can lead to a reduction of the molecular weight of the PC during melt processing. Inorganic pigments (ultramarine, LANSCO UPL-2905) were used as flow indicators to reveal the flow history of PC filament during printing.

3.2.2. Viscosity measurement

The viscosity of PC at different shear rate was measured using a Rosand RH7 capillary rheometer at 325°C. Results are shown in Figure 3-4. The PC

pellets were dried in a vacuum-oven at 110°C for 12 h to remove residual water prior the measurement.

3.2.3. Filament Extrusion

Filaments of PC were extruded using a HAAKE single screw extruder (Model Rheomex 252p) that was equipped with a gear pump and a simple circular die (diameter = 2.2 mm). This extruder has 3 independently controller temperature zones that can be used to modulate the viscosity of the PC during the extrusion. For the filament extrusion, a temperature profile from the feeding section to metering section was set at 280°C, 290°C, 275°C; while the gear pump and circular die were set to 280°C and 240°C. The extruded PC melt was quenched in a room temperature water bath and then drawn onto a take-up wheel. The diameter of extruded filament was drawn down to 1.7 mm. by controlling the take-up speed relative to the extrusion rate. The diameter of the filaments was controlled to 1.70 ± 0.03 mm for these studies.

3.2.4. 3D Printer

For the FFF, a customizable 3D printer was used in this study: Cartesio 3D printer (Model: W09). This printer was equipped with an E3D-v6 (1.75mm-type) hot-end(liquefier) assembly with a 0.4-mm nozzle. The liquefier was heated using a 24V-40W cartridge heater (E3D).

3.2.5. Flow Indicator

PC and blue inorganic pigments were dried in vacuum oven for 12 hours at 110°C before mixing. Then PC pellets and blue inorganic pigments were melt blended at a weight ratio of 4:1 in a Brabender mixer at 280°C and 40 rpm for

10 min. This blue colored polymer was then pelletized, dried, and melt-spun using a capillary rheometer at 280°C into 0.3 mm-fiber. These blue fibers were inserted into the non-pigmented PC filaments. To facilitate this, holes at intervals of 3 mm were drilled radially through the axis of PC filaments with a drill press equipped with a 0.3mm-drill bit while utilizing a specially designed holding jig. The blue PC fibers were inserted into the drilled holes and trimmed to length as illustrated in Figure 3-1. To eliminate air gaps between the inserted blue fibers and PC filaments, the inserted fiber was lightly heated with hot air. This heat allowed the melt spun fiber to relax, which led to a decrease in the lengthwise direction, while slightly expanding radially to close the gap inside the drilled holes.

The filaments containing the radially placed blue PC fibers were extruded as illustrated in Figure 3-1. The influence of extrusion speed (v) and temperature (T_{ext}) was systematically investigated. To understand the flow patterns, some filaments were fully extruded from the nozzle and cooled to enable the blue pigment distribution to be visualized. In addition, the extrusion was paused while the filament section with blue PC fibers remained inside the nozzle. This allowed the polymer in the extruder to be vitrified to examine the flow profile. The nozzle was unscrewed from the liquefier and then the metal nozzle was cut with an LECO VC-50 diamond saw to allow the solidified PC to be removed from the nozzle in one piece for further characterization.

Pigment distribution in extruded filaments and was examined using optical microscopy (Olympus BX51). A 35-mm long section of each extruded filament was placed on a glass slide and immersed with refractive index matching oil

(Cargille Series A, n=1.57) to minimize the refraction of light and associated scattering. Images were taken systematically along the length, and then stitched into one image to fully characterize the whole section of the filament.

Pigment distribution in the extruded filaments and the solidified PC removed from the nozzle were both measured by MicroCT (Bruker Skyscan1172). The high Z content of the pigment enables its distribution to be assessed with X-Ray tomography. The scans were operated at 50kV/200 μA. Transmission X-ray images were recorded at 0.4° rotational steps for 180° of rotation. The resulting 2-D transmission images were imported into **NRecon** software to reconstruct the cross-section images. The resulting 2-D cross-section images were imported into Skyscan CT Analyzer(V1.1) to reconstruct the full 3D-image.

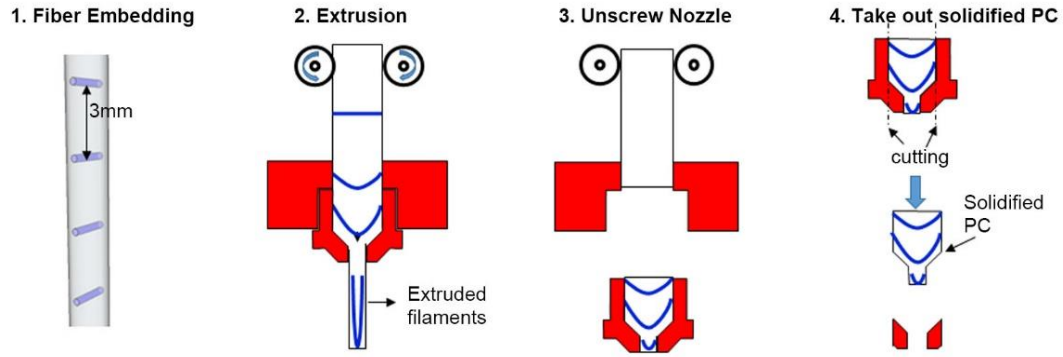

Figure 3-1 Schematic illustration of the procedure for removing the solidified polymer remaining inside the nozzle. The PC filament contained embedded melt-spun blue PC fibers to visualize the flow profile.

3.2.6. Measurement of temperature history during extrusion

The temperature of the center of the filament during the printing extrusion process was directly measured as illustrated in Figure 3-2 using OMEGA

CHAL-002 K-type fine-gauge thermocouples (0.05 mm diameter). The thermocouples were coated with a heat-resistant insulation layer from RUST-OLEUM heat-resistant primer spray to prevent short-circuiting during the measurements. The thermocouple was embedded in the center of the filament that contained a pre-cut groove for the thermocouple. The connecting wires of the thermocouple were fed through the opening of the printer's nozzle. The potential of the thermocouple was measured using National Instrument TI SC2345 with the temperature recorded every 0.1 s. As the filament was extruded, thermocouple embedded in the filament was drawn into and through the liquefier at the same speed as the PC filaments.

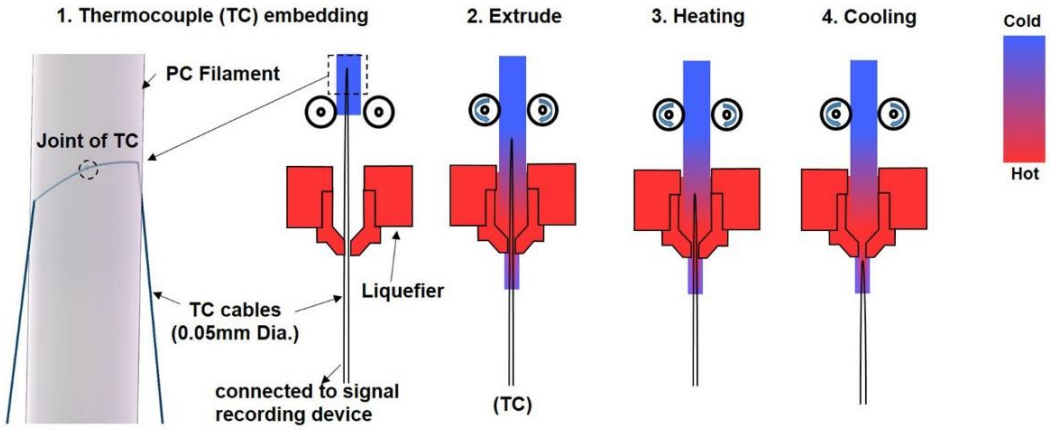

Figure 3-2 Schematic diagram of the real-time melt temperature measurement of filament extrusion by embedding the tip of a fine thermocouple into the center of the filament

3.3. Theory and calculations for polymer flow in extruder

The flow of the PC in the liquefier can be described in terms of pressure driven flow as the rollers of extruder pull the filament to act as a plunger to press on the molten PC within the liquefier. The blue fibers embedded in the PC

filament provide a route to visualize the flow field from the relative lateral displacement of the pigment as illustrated in. At the entrance to the liquefier, the filament remains vitrified and the velocity is uniform radially (plug flow). The melting of the filament leads to a decreased velocity near the wall due to the no slip condition at the wall (v_z (r/R=1) =0).

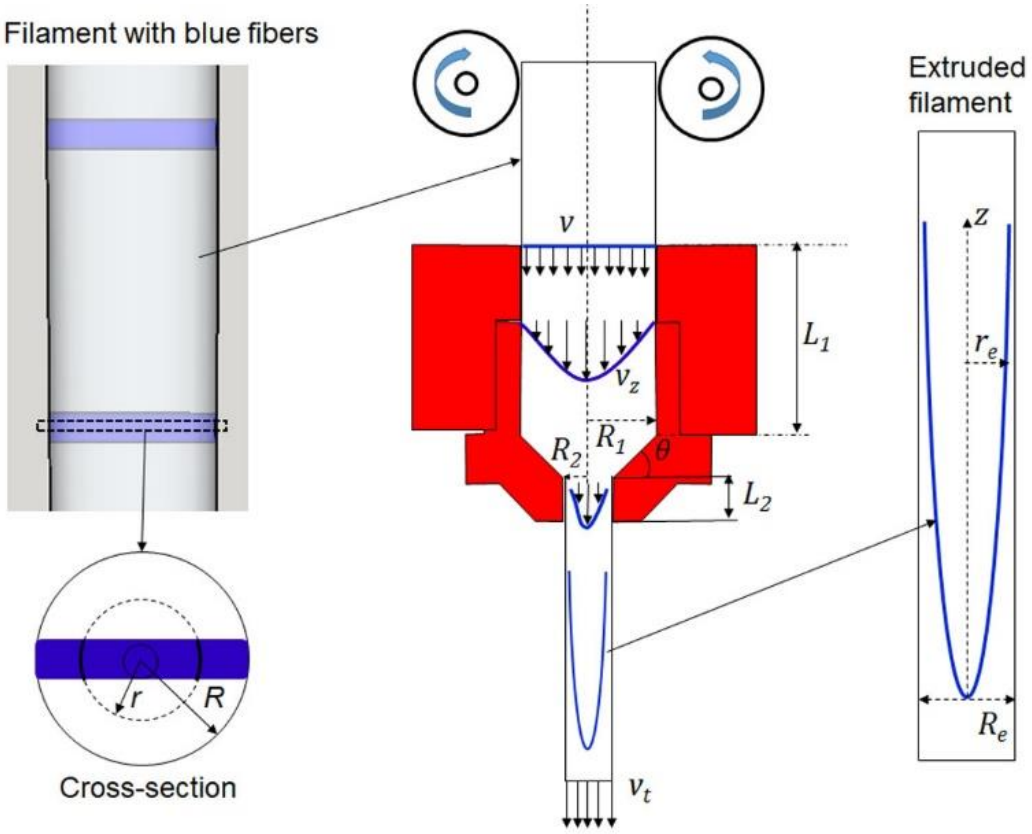

Figure 3-3 Schematic of velocity profile, v_z(r/R), determined from the deformation of the pigment distribution during extrusion process.

As shown in Figure 3-3 due to the pressure applied by the incoming filament section, a velocity profile $v_z=v_z$(r/R) is developed with the maximum velocity at the center $v_{z,max}=v_z(0)$ and zero velocity at the wall v_z(r/R=1)=0. The pigment particles at position *r* will move with velocity v_z(r/R). Pigment particles near the center of the filament will be extruded through the nozzle first. As the

extruded filament exits the nozzle, it obtains an effectively uniform velocity, v_t, through the uniaxial elongation. Thus examination of the pigment profile of the extruded filament profiles information that is almost exclusively associated with the flow within the liquefier and through the nozzle.

Due to the high viscosity of polymers, the flow in the liquefier should be pressure driven laminar flow. For the uniform diameter section of the liquefier, the flow should be unidirectional with $v=v_z$, $v_r=0$, and $v_\theta=0$. Due to this simple flow profile, a pigment particle initially at r/R as it enters the liquefier will remain at the same radial location, $r_e/R_e=r/R$, in the extruded filament with the center of the extruded fiber (r/R=0). The relative displacement of the pigment can be normalized by a reference frame of $v=v_{z,max}$ such that the pigment in the center of the extruded filament is located at z=0 as shown in Figure 3-3. As illustrated in Figure 3-3, the relative pigment particle displacement z at r_e/R_e should be related to the residence time difference, Δt, between the pigment particles at $r/R=r_e/R_e$ and those at the center (r/R=0) as:

$$z = \Delta t \times v_t \tag{3.1}$$

For flow in a cylindrical pipe of length L:

$$\Delta t = \left(\frac{L}{v_z\left(r/R\right)} - \frac{L}{v_{z,max}} \right) \tag{3.2}$$

For a conical cylindrical region of total length L and tangent angle θ, v_z undergoes an acceleration process:

$$\frac{dl}{dt} = v_z \tag{3.3}$$

$$t = \int_0^L \frac{1}{v_z} dl \tag{3.4}$$

l is the distance from the entrance of the conical region. Therefore l can be directly related to R by:

$$l = (R_1 - R) \times \tan\theta \tag{3.5}$$

Thus, residence time difference in a conical region associated with the end nozzle can be expressed as:

$$\Delta t = \int_{R_2}^{R_1} \frac{\tan\theta}{v_{z,max}} dR - \int_{R_2}^{R_1} \frac{\tan\theta}{v_z(r/R)} dR \tag{3.6}$$

For a liquefier with a cylindrical region (Region I) of length L_1 that is connected to a capillary region of length L_2 (Region III) at the nozzle by a conical region(Region II), the position of the pigment on the extruded filament, z, can be expressed as:

$$\begin{aligned} z\left(\frac{r}{R}\right) = \Delta t_{total} \times v_t = v_t \times \left(\frac{L_1}{v_{z1}(r/R)} - \frac{L_1}{v_{z1,max}}\right) + v_t \times \\ \left(\frac{L_2}{v_{z3}(r/R)} - \frac{L_2}{v_{z3,max}}\right) + v_t \times \left(\int_{R_2}^{R_1} \frac{\tan\theta}{v_{z2,max}} dR - \int_{R_2}^{R_1} \frac{\tan\theta}{v_{z2}(r/R)} dR\right) \end{aligned} \tag{3.7}$$

where v_{z1}, v_{z2} and v_{z3} are the velocities in corresponding regions of the liquefier. If the volumetric flow rate is constant Q, thus $v_t = \frac{Q}{\pi R_e^2}$ and the expression can be re-written as:

$$z\left(\frac{\mathrm{r}}{\mathrm{R}}\right)R_e^2 = \frac{Q}{\pi}L_1\left(\frac{1}{v_{z1}\left({}^{r}/_{R}\right)} - \frac{1}{v_{z1,max}}\right) + \frac{Q}{\pi}L_2\left(\frac{1}{v_{z3}\left({}^{r}/_{R}\right)} - \frac{1}{v_{z3,max}}\right) + \frac{Q}{\pi}\left(\int_{R_2}^{R_1}\frac{\tan\theta}{v_{z2,max}}dR - \int_{R_2}^{R_1}\frac{\tan\theta}{v_{z2}(r/R)}dR\right) \quad (3.8)$$

For an isothermal Power-law fluid ($\tau_{rz} = m(-\frac{dv_z}{dr})^n$), the velocity profile of the flow in a cylindrical pipe or conical region can be expressed as[202]:

$$\frac{v_z}{V} = \frac{3n+1}{n+1}\left[1 - (\frac{r}{R})^{(n+1)/n}\right] \quad (3.9)$$

where the mean velocity is $V = Q/\pi R^2$.

For a Power-law ($\tau_{rz} = m(-\frac{dv_z}{dr})^n$) fluid, the velocity component parallel to axis in a cylindrical-conical region can be expressed as:

$$v_z = \frac{3n+1}{n+1}\frac{Q}{\pi R^2}\left[1 - (\frac{r}{R})^{(n+1)/n}\right] \quad (3.10)$$

thus, we can obtain for an isothermal power-law fluid:

$$\mathrm{z(r/R)}R_e^2 = \frac{n+1}{3n+1}\left[L_1R_1^2 + L_2R_2^2 + \frac{(R_1^3 - R_2^3)\tan\theta}{3}\right]\left[\frac{(\frac{r}{R})^{1+n/n}}{1 - (\frac{r}{R})^{1+n/n}}\right] \quad (3.11)$$

This expression provides the ideal profile for the pigment particles and can be used to assess any corrections that might be necessary to describe the flow through the extruder for 3D printing by FFF. This expression show that the pigment profile is only dependent on the power-law factor-n and the liquefier geometry.

The rheological properties measured using a capillary rheometer at 325°C is shown in Figure 3-4. At this temperature, a power law index of 0.80 can be

obtained via fitting the data using the power-law model. The geometry of the flow channel in the liquefier is shown in Figure 3-5. With the liquefier geometry and power law index obtained, $\mathrm{z(r/R)}R_e^2$ vs. $\frac{r}{R}$ can be calculated using equation (3.11).

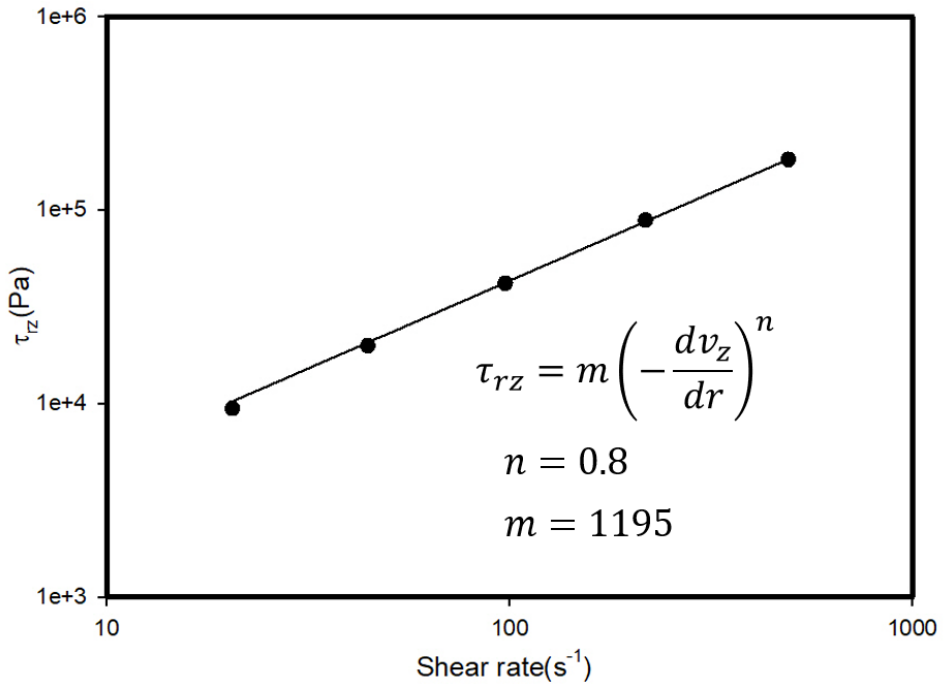

Figure 3-4 Shear stress vs. shear rate measured with a capillary rheometer (Rosand RH7 by Malvern) at T=325°C.

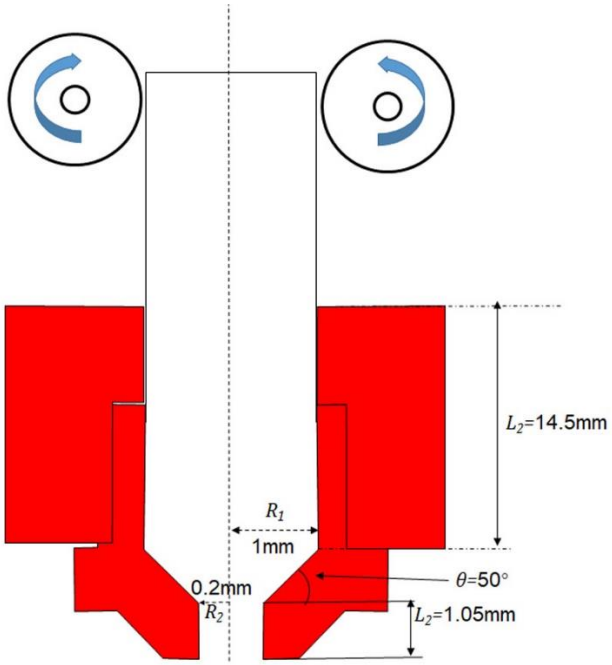

Figure 3-5 Dimensions of the liquefier

3.4. Results and Discussion.

3.4.1. Pigment distribution in extruded filament

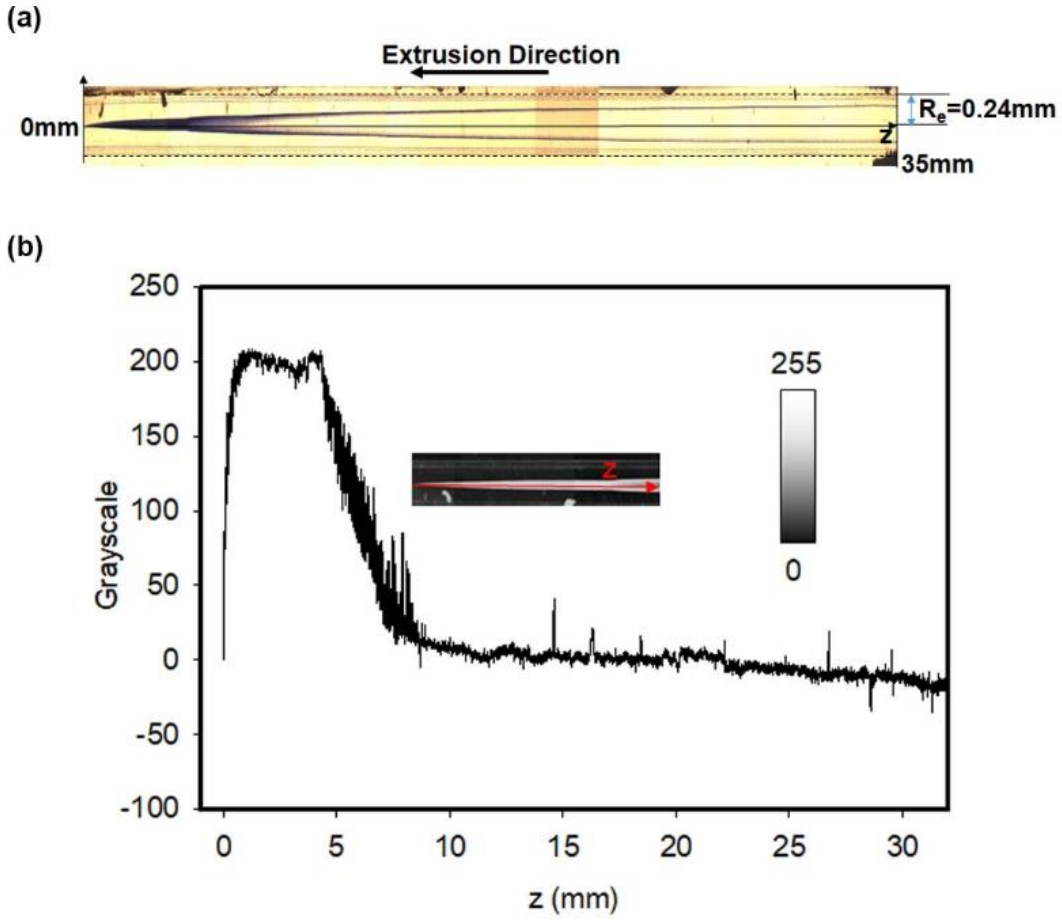

Figure 3-6 (a) Optical micrograph of filament with pigment extruded at T_{ext}=275°C and v=140mm/min (image is expanded radially to allow the distribution to be visualized as noted by the scales). (b) Quantifying the pigment distribution using 8-bit grayscale along the length of the extruded filament @ center (r=0)

Figure 3-6(a) shows a composite optical micrograph of an extruded filament that contained the blue pigment. The pigment is distributed in a tapered shape along the extruded filament, which suggests that velocity profile $v_z=v_z(r/R)$ developed in the liquefier during extrusion is reflected in the

location of pigmented regions. In order to quantify the distribution of pigment, the micrograph in Figure 3-6(a) was converted to a grayscale image with inverted color as shown in the inset in Figure 3-6 (b) for a section of the microscope image. For these grayscale images, the areas with high pigment concentration are bright and thus the corresponding grayscale value is high. Figure 3-6 (b) shows the relative concentration of pigment along the center of the filament (r=0). As the length of the filament is probed from the first extruded region, the pigment concentration rapidly increases, which corresponds to the tip of the tapered-shape distributed blue pigments. The high pigment content appears to persist for approximately 4 mm, which is much greater than the 0.3 mm initial diameter for the pigment. This broadening is attributed to the combination of dispersion [203] and the radial distribution of the pigment, which leads to some concentration in the center as can be visualized in Figure 3-6 (a). This latter point is likely partially responsible for the long decay along z in the apparent pigment concentration at r =0. However, the grayscale images as shown in Figure 3-6 provide an integrated measure of the pigment particle concentration through the full thickness of the filament slice examined. The optical microscope images do not show the exact location of the pigment within extruded filament.

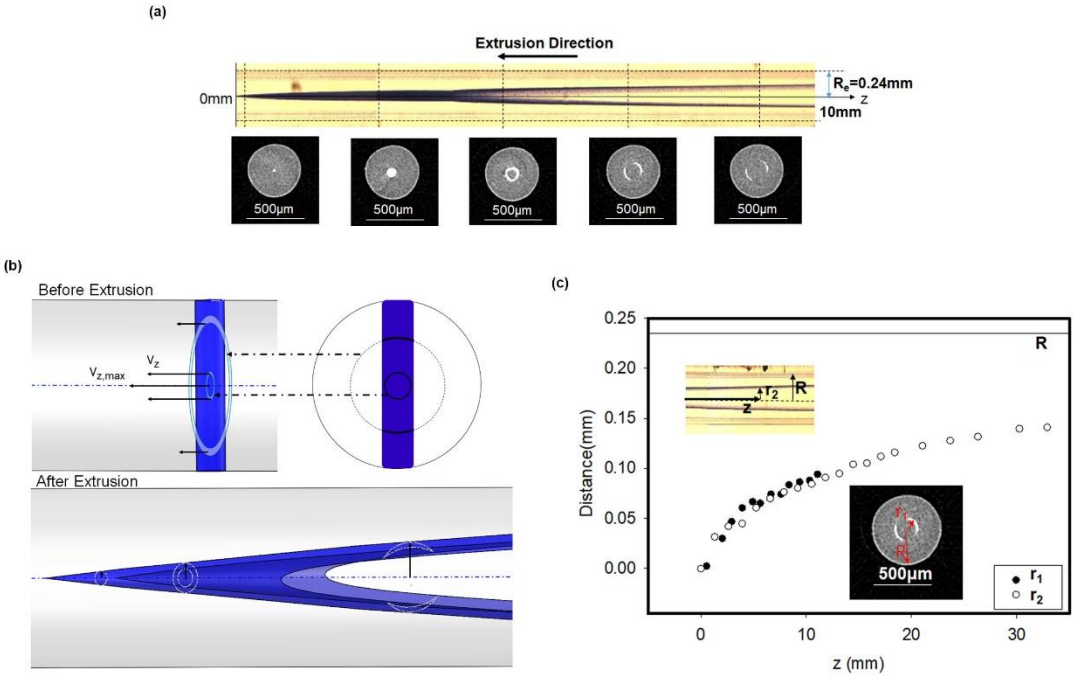

Figure 3-7 (a) MicroCT cross-section images at z-position of the extruded filament; (b) Schematic of deformation of the pigment during extrusion; (c) Measured distances from the outline of pigments to the center of the extruded filament from (●) MicroCT image and (○) optical microscope image vs. the corresponding distance along the length of filament (T_{ext}=275°C, v=140 mm/min). The insets in (c) show an example of how the distances are measured.

In order to determine if the optical images can be used for quantifying the pigment distribution, the internal structure of the extruded filaments was characterized by X-ray micro-computed tomography (Micro-CT) [42] 20] as there is sufficient contrast (X-ray absorption) between the pigment and the PC. Slices of the 3D image determined from Micro-CT at different positions (z) along the length of the extruded filament are shown in Figure 3-7(a). As a result of the developed velocity field $v_z=v_z(r/R)$ in the nozzle, each liquid volume element experiences a different residence time through the liquefier.

The MicroCT cross-section images at smaller z (initial pigment out of liquefier) show only the pigments near the center, and as we progressively move upstream the pigmented regions expand outward. As the 0.3mm-wide pigmented fiber is initially a line profile, the ring associated with the pigment transitions to two symmetric arcs at a sufficient distance that is associated with the width of the pigment in the filament as illustrated in Figure 3-7 (b).

However, Figure 3-7 (a) proves that at each cross-section the pigment distribution is symmetric about the center. Therefore, the distance from the outline of pigments to the center of the extruded filament (r_e) could be quantified, which should be equivalent to the distance determined by the optical images (Figure 3-7). To verify the validity of the r_e as a function of z measured from the microscope images, the distance from the outline of pigments to the axis of the extruded filament measured on microscope image (r_2) and the radius of the arc measured on MicroCT cross-section image (r_1) are compared as a function of z in Figure 3-7 (c). Figure 3-7 (c) shows r_1 is consistent with r_2 at all measured points. This consistency proves the r_e measured from 2D microscope images can be used to accurately quantify the pigment distribution, which allows measurement of r_e over a larger range of z than possible for Micro-CT.

3.4.2. The effect of temperature and flow rate on the pigment distribution in extruded filaments

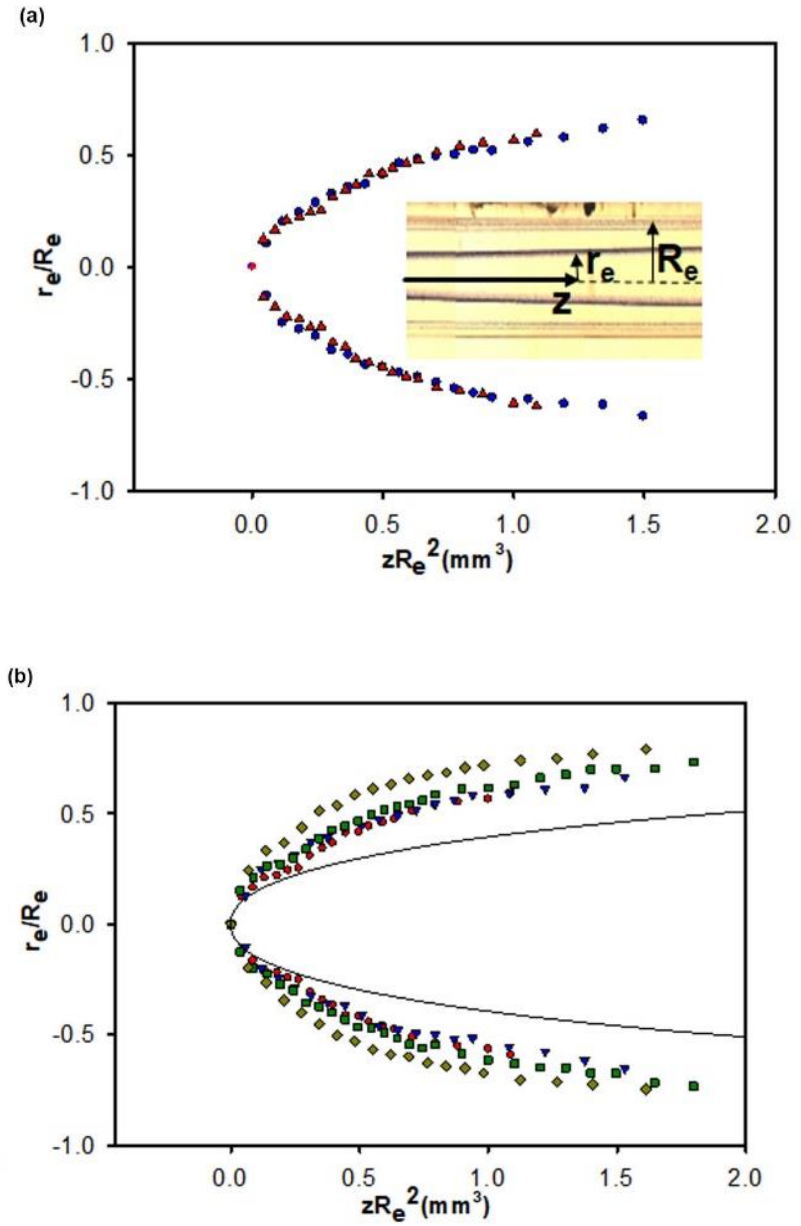

Figure 3-8 Location of maximum pigment in the extruded filament: (a) constant extrusion speed (v=140mm/min) @ T_{ext}= (●)275°C and (▼)325°C; (b) constant extrusion temperature (T_{ext}=325°C) @ (●)v=90mm/min, (▼)140mm/min, (■)180mm/min, (◆) 270mm/min, and (—) calculated distribution based on an isothermal Power-law fluid

Figure 3-8(a) illustrates how the location of the maximum pigment concentration depends on the axial distance as determined by optical microscopy for two extrusion temperatures (T_{ext}). In order to readily compare between samples, normalized variables are used for the radial coordinate, r_e/R_e, and the axial coordinate, $z_eR_e^2$. The pigment particles that were initially extruded in the filament (set as z=0) are located at the center of the filament, which is due to the maximum velocity at the center $v_{z,max}=v_z(r/R=0)$ during extrusion through the liquefier. At larger $|r_e/R_e|$, the pigment particles are located at larger zR_e^2, as expected from the resistance from the liquefier surface as depicted in Figure 3-7(b). Figure 3-8(a) shows that pigment distribution in filaments extruded at different T_{ext} is the same, suggesting that changing the temperature of the liquefier (T_{ext}) does not significantly impact the velocity profile within the temperature range investigated.

Conversely as shown in Figure 3-8 (b), the pigment distribution in filaments extruded at T_{ext}=325°C depends on the extrusion speed. At the highest velocity examined, the pigments appear to move in a more plug-flow like manner with the pigment at large $|r_e/R_e|$ being found at smaller $z_eR_e^2$. In addition to the differences in the profiles at different extrusion speeds, the calculated pigment distribution for an isothermal power-law fluid, eq. (11), deviates substantially from all of the measured distributions as shown in Figure 3-8(b) (see 3.2.6 for information about the power law fluid model). The calculated pigment distribution depends only on the power-law factor n and liquefier geometry, while the measured distribution shows the distribution is dependent on the extrusion speed. The reasons for the deviation are likely complex and associated with the design of liquefiers for FFF in general. First, the molten

filament in the liquefier does not instantaneously reach its fully developed velocity profile illustrated in Figure 3-3, instead there is a transient start-up flow with the velocity profile initially being approximately flat that progressively changes until the flow is fully established [202]. This transition at the entrance to the liquefier reduces the relative displacement, *z*, for pigment particles at r/R, as the velocity is initially similar to that for the pigment at the center (r/R = 0). In addition to the start-up flow issues at the entrance, the heating of the filament is non-uniform due to the low thermal conductivity of the polymer. The surface of the filament heats to T_{ext} rapidly as it contacts the liquefier while the center of the filament remains cold and thus exhibiting higher viscosity than the polymer near the liquifier surface. As the polycarbonate is heated through its T_g (150°C), the viscosity difference between the surface and the center of the filament can be orders of magnitude. When the center is below T_g, a flat velocity profile would be maintained, as the PC is solid-like. Even when $T>T_g$, but before reaching the uniform temperature, the shear rate ($\frac{dv_z}{dr}$) of the fluid near the center of the filament would be smaller than calculated for isothermal flow, due to its higher viscosity at a lower temperature. All these effects could reduce the difference between maximum velocity at the center of the filament and velocity at r>0, thus decreasing the relative displacement z.

Figure 3-8(b) shows that as the extrusion speed v increases, the deviation from an ideal isothermal flow becomes larger. Increasing the extrusion speed reduces the relative displacement z for pigment particles, which suggests a smaller difference to the maximum velocity $v_{z,max}$ during extrusion and a more flat velocity profile. However, the average residence time in the liquefier

decreases as the extrusion speed increases and thus the flow profile becomes less developed due to the slow heat transfer. Both the entrance effect and the heat transfer process effectively reduce the shear rate near the center of the filament to generate a less steep velocity profile.

3.4.3. Real-time melt temperature measurement

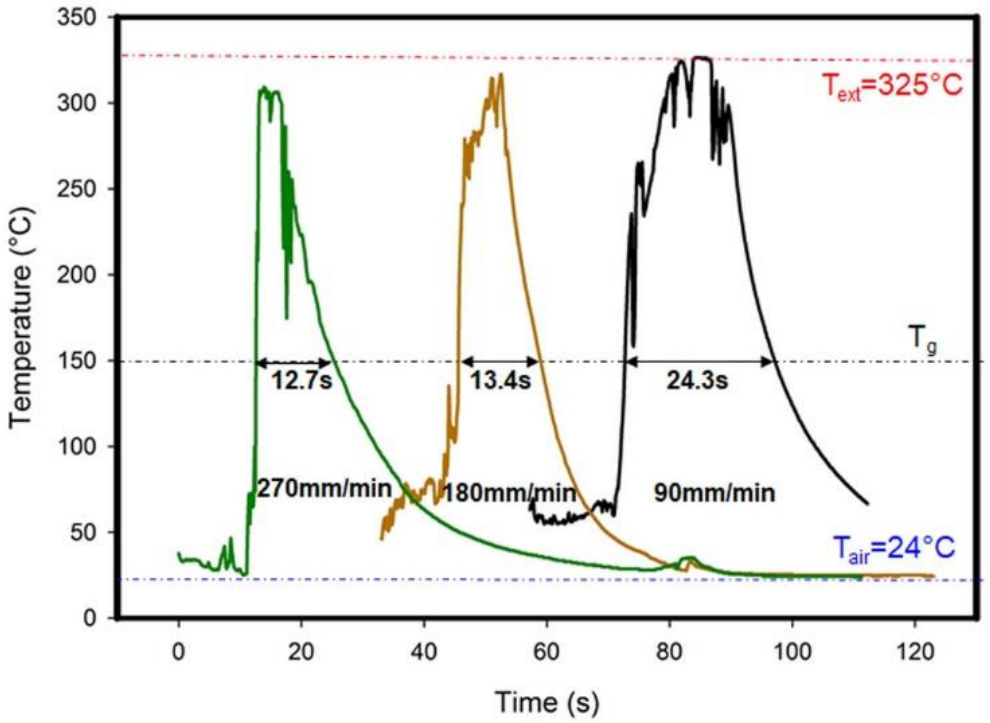

Figure 3-9 Temperature history of PC filaments during extrusion as a function of print speed (90-270mm/min) @ T_{ext}= 325°C. Each condition is offset by 30 s for clarity.

One source for the pigment distribution differing from the ideal profile is the temperature difference between the flow near the surface and that at center during extrusion. Because the viscosity of a polymer melt is highly dependent on temperature especially near T_g, a direct measurement of the temperature history could be helpful for understanding the flow behavior in FFF extrusion.

To measure the temperature history of the filaments during extrusion, miniature (diameter: 0.05 mm) thermocouples were embedded in the filament, as illustrated Figure 3-9, due to their ability to detect subtle temperature variations [58,204,205]. As the filament is extruded, thermocouple moves with the PC filament and records the temperature history of the center of the filament center as the filament is extruded through the nozzle. As shown in Figure 3-9, the filament is rapidly heated as it enters the liquefier then gradually cools to ambient temperature after it is extruded out of the nozzle with the polymer melt.

One interesting point from these measurements is that the total time the filament stays above its T_g is very short (12.4s, 13.3s, 24.3s) with the heating period decreasing as the extrusion speed increases. Due to the limited residence time, the maximum temperature at the center of the filament is dependent on the extrusion speed due to limitations of heat transfer. The maximum temperature measured for extrusion speeds of 90 mm/min, 180 mm/min, and 270 mm/min are 325°C, 314°C and 306 °C, respectively. The measured stationary melt temperature is 325°C, which equals to T_{ext}. Thus at v=90 mm/min, the center of the filament reaches its thermal equilibrium for the given liquefier geometry, but in general the center of the filament remains cooler than the inner surface of liquefier when printing at high extrusion speeds. Even at v=90 mm/min, the temperature history of the center of the filament shows that the equilibrium temperature of T_{ext} is maintained for a relatively short period (< 10 s). This radial temperature gradient from the center to the surface will affect the flow behavior of polymer melt through the extrusion process. As discussed previously in section 3.4.2, the lower temperature near the center of the filament leads to a higher melt viscosity and a lower shear rate (dv_z/dr),

which results in a smaller relative displacement z compared to that expected for isothermal flow as experimentally shown in Figure 3-8(b).

3.4.4. Pigment distribution inside the liquefier nozzle

In section 3.4.1, the discussion of the influence of velocity profile $v_z(r/R)$ on the pigment distribution in extruded filaments assumes a fully developed flow, where the velocity profile is independent of time. As the temperature history shown in Figure 3-9 is evidence of temperature gradients during extrusion, the velocity profile may not be fully developed, which could provide an additional explanation beyond entrance effects and non-isothermal conditions for the large difference between calculated and measured pigment distributions in Figure 3-8(b). As the pigment distribution in extruded filament is a result of average velocity difference through the whole extrusion process, it cannot reveal how the velocity profile changes inside the liquefier during extrusion.

The velocity profile inside the liquefier was elucidated by removing the polymer inside of the liquefier after partial extrusion of filaments at high speed (v=270mm/min). Figure 3-10(a) shows the X-ray projection of the filament perpendicular to the extrusion direction. A series of projection images were used to generate cross-section images that are shown at different distances along the filament and a reconstructed 3D image of the solidified polymer melt removed from the nozzle as shown in Figure 3-10(a). The bright regions in the cross-section images and the 3D image correspond to the pigment. As multiple pigment fibers were added to the filament, it is possible to examine the flow at different locations in the liquefier with a single Micro-CT scan, where two different embedded blue PC fibers are shown in Figure 3-10(a).

The flow in the wider section of the liquefier is illustrated in the cross-section images. The distribution of the pigment is pseudo-conical closest to the nozzle exit. The bottom cross-section image shows effectively a circular point at the center of the filament associated with the highest velocity in the middle of the nozzle. Moving up the filament away from the nozzle end, the diameter of this center point increases until the diameter of the pigment matches the width of the pigment dyed fiber embedded in the filament. The cross section then becomes a rounded rectangle as shown in the middle image. The width of the short side of this rounded rectangle is 0.41 mm, which is slightly larger than the original fiber diameter (0.3 mm). Moving further from the nozzle exit, leads to pigment distributed in two arcs that are symmetric about the center of the filament. This distribution of pigment is qualitatively consistent with expectations for flow in a cylinder. By examining the reconstructed 3D model in Figure 3-10 (a), the 3D distribution pigments from two different blue PC fibers can be observed. In the wide cylinder region, the pigment distribution appears to be parabolic, while there appears to be a rapid acceleration in the converging region as the pigment distribution is stretched.

Figure 3-10 (b) quantifies the difference in the pigment profiles for these two fibers as a function of the distance from the liquefier entrance. In addition, the ideal profile in the cylindrical region for isothermal pressure driven flow is shown in Figure 3-10(b), which is based on the velocity profile given by eq. (10). The profile for the pigment in the cylindrical region approximately 9-11 mm from the entrance is relatively flat near the center of the filament in comparison to the calculated parabolic profile for isothermal pressure driven flow. However, at

high speed, the center of the filament remains colder than the surface (T_{ext}) throughout the liquefier (Figure 3-9). The lower temperature of the center of the filament increases the local viscosity to decreases the shear rate (dv_z/dr) that leads to the blunted velocity profile.

The particle profile in the converging region illustrates how the flow field is impacted by the capillary region of the nozzle as shown in Figure 3-10(b). The polymer inside the capillary region of the nozzle could not be removed from the nozzle, which is the reason for no pigments in the center of the filament from this fiber. The pigment particles that have entered the converging region are drawn out along the filament as a result of the larger shear rate from the narrowing wall of the nozzle. In addition, the channel diameter decreases facilitating more efficient heat-transfer, which should decrease the viscosity in the center of the filament. However after the filament exits the nozzle, the distribution near the center appears to remain blunted (Figure 3-8).

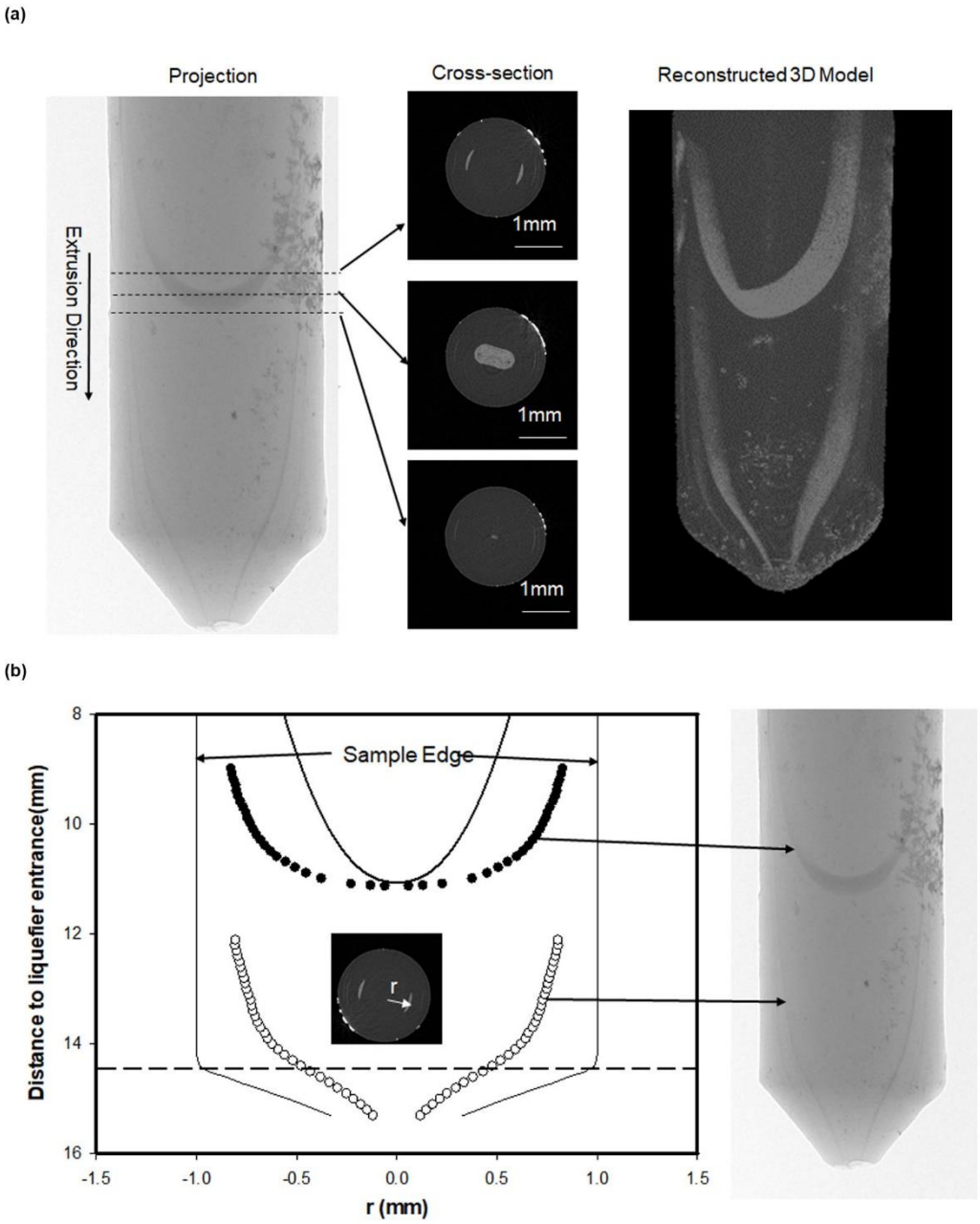

Figure 3-10 (a) MicroCT X-Ray projection image, cross-section image and reconstructed 3D model of the solidified PC within the nozzle after extrusion @ Text=325°C and v=270mm/min; (b) Quantification of the pigment particle distribution(○,●) within the filament as a function of distance from the liquefier entrance. The center of the filament is at r = 0. The solid line (—) illustrates the predicted flow profile based on the isothermal power-law model.

3.5. Conclusions

This paper reports an experimental approach to elucidate the temperature and flow history in the FFF extrusion process. The measured pigment distribution in extruded filaments is indicative of a smaller shear rate near the center, which leads to more blunted velocity profile as compared to that expected for an isothermal Power-law fluid. The measured temperature history demonstrates the FFF extrusion process is highly non-isothermal, especially at high extrusion speeds. The deviations in the pigment distributions from ideal isothermal flow can be attributed to both entrance effects and the temperature gradient in the nozzle.

CHAPTER IV

POLYCARBONATE-BASED CORE-SHELL FILAMENTS MANUFACTURED VIA CO-EXTRUSION

4.1. Introduction

Fused Filament Fabrication(FFF) builds 3D objects by depositing melt polymer filaments onto a growing workpiece. In this process, the hot polymer melt filament re-melts the preceding layer so that two adjacent layers are bonded together through interdiffusion of polymer chains before the melt cools down and solidify. Because interdiffusion of polymer chains occur only at temperature well above its solidification temperature, limited time at high temperature in this process results in poor bond strength at the layer interface[57,60,165] Therefore, mechanical properties of the FFF manufactured parts are inferior to parts fabricated by conventionally polymer processing techniques[45,206].

There has been a push to enhance the mechanical properties of FFF manufactured parts through adding reinforcement filler[169,206,207]. However, improvement of the mechanical strength of bulk material does not overcome the interfacial bond weakness in FFF manufactured parts. It is reported that higher operating temperature[57,60] or increased heating time[208] can promote the bond strength and thus mechanical properties. However, high temperature leads to a trade-off in dimensional fidelity due to distortion induced by overheating of printed parts[208]. Therefore, there has been a difficulty in

thermally bonding printed filament better without sacrificing the shape accuracy of the parts.

In this Chapter, we introduce an approach to overcome this difficulty which is utilizing core-shell structured filaments as feedstock in FFF 3D printing. These core-shell filaments are composed of shells with lower viscosity or T_g and a core with high T_g and high mechanical strength. When a core-shell filament is extruded by the FFF 3D-printer, low-T_g/low viscosity shell layers deposited at the filament interface improves the interdiffusion and gap filling performance, while the core solidifies fast to prevent the shape from being deformed by the melt flow as shown in Figure 4-1 .

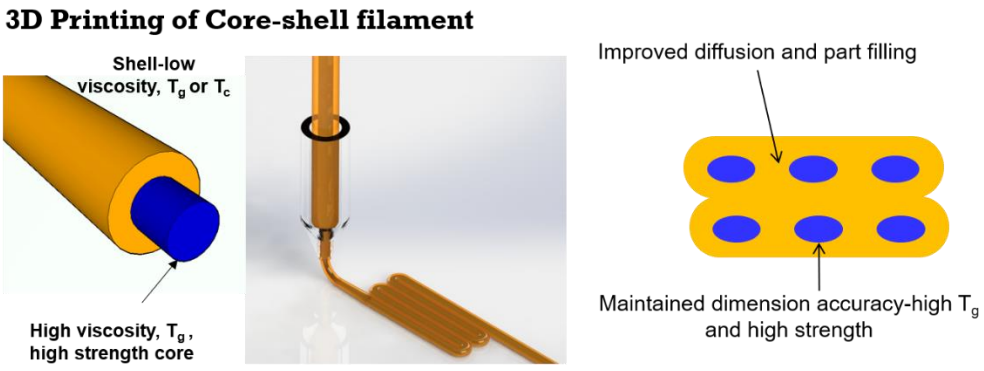

Figure 4-1 Schematic illustrates that 3D-printing of a core-shell filament improves the diffusion and part filling by using a shell layer with low viscosity, T_g or T_c

Single-screw extruder can efficiently produce continuous thermoplastic objects with fixed cross-section, therefore is often used for FFF filament fabrication [209,210]. One single-screw extruder can only extrudes one kind of thermoplastic at a time. To produce core-shell structure filaments, we developed a co-extrusion system composed of two single-screw extruders that

can melt core and shell material seperately and deliver their melt to co-axial circular die to form the core-shell structure.

4.2. Experimental

4.2.1. Materials and Characterization

Bisphenol-A polycarbonate Makrolon 3208 and 2205, and PC copolymer APEC 1895, PC/ABS blend T65PG and FR3010 were received from Covestro LL and were used for fabrication of 3D printing filaments. Prior to extrusion or 3D printing, pellets (as obtained from Covestro, LLC) or filaments were dried in a vacuum oven for 12 h to remove residual water at 110 °C. which can lead to a reduction in the molecular weight of polymers during melt processing. Differential scanning calorimetry (TA Instruments DSC, model Q2) used to analyze the thermal properties of the materials. DSC scan was performed at a heating and cooling rate of 10 °C min−1 under a nitrogen atmosphere. Rheology properties of the polymer was measured using a Rosand RH7 capillary rheometer at different temperature.

4.2.2. Filament extrusion

Extrusion of single component monofilament were carried out using a HAAKE single screw extruder(Model Rheomex 252p) that was equipped with a gear pump and a simple circular die (diameter=2.2 mm). This extruder has 3 independently controller temperature zones that can be used to modulate the viscosity of the PC during the extrusion. For the filament extrusion, a

temperature profile from the feeding section to metering section was listed in Table 4- 1.

Table 4- 1 Temperature profile for filament extrusion using Rheomex 252p.

Sample	Zone 1 T (°C)	Zone 2 T (°C)	Zone 3 T (°C)	Die T (°C)
Bayblend T65PG	240	250	255	250
Makrolon 2205	280	270	250	210
Makrolon 3208	280	290	275	240

Alternatively, single component filaments of Bayblend FR3010 and Apec 1895 were extruded using a different single screw extruder (Akron Extruder, Model M-PAK 125) equipped with a gear pump and a filament die (diameter=2mm). The temperature profile for the extrusion process for the materials is shown Table 4-2.

Table 4-2 Temperature profile for filament extrusion using M-PAK125.

Sample	Zone 1 T (°C)	Zone 2 T (°C)	Zone 3 T (°C)	Metering Pump T (°C)	Die T (°C)	Extruder (rpm)
Bayblend FR 3010	240	250	260	240	240	6
APEC 1895	300	290	270	300	285	6

Core-shell filament were fabricated using a customized co-extrusion system that is composed of two single-screw extruders (Rheomex 252p and Akron Extruder M-PAK 150) with a co-axial circular co-extrusion die. Each extruder was connected to a separate gear pump to control the flow rate ratio of the core and shell melt flow. The extruded filaments were quenched in a room-temperature water bath and drawn onto a take-up wheel. The diameter

of the filaments was controlled to 1.65-1.70mm. The temperature profiles for coextrusion shown in Table 4-3.

Table 4-3 Temperature profile for filament co-Extrusion

Extruder 1(core)	Zone1	Zone2	Zone 3	Melt Pump
APEC 1895	280°C	295°C	310°C	320°C
Makrolon 3208	300°C	290°C	280°C	290°C
Extruder 2(shell)	**Zone1**	**Zone2**	**Zone 3**	**Melt Pump**
FR3010	210°C	225°C	240°C	240°C
Makrolon 2205	290°C	275°C	260°C	275°C
Die: Core/Shell	**Connector1 (to Core)**	**Connector2 (to shell)**	**Die Body**	**Die Nozzle**
APEC 1895/FR3010	270°C	240°C	270°C	250°C
Makrolon 3208/FR3010	250°C	230°C	240°C	230°C
Makrolon 2205/FR3010	240°C	230°C	230°C	220°C
Makrolon 2205/FR3010HF	230°C	230°C	220°C	210°C

4.2.3. 3D Printing.

A customizable 3D printer (Cartesio 3D printer model: W09) equipped with an E3D-v6 hot-end (1.75mm-type) assembly with a 0.4 mm nozzle was used to print the samples. For impact tests, samples in accordance with ASTM-D256 were 3D- printed at three different orientations. The thickness of the samples

printed in XY and XZ directions was 3 mm, whereas the thickness in the YZ direction was 12.7 mm.

During printing, the print bed (build-platform) was covered with a Kapton tape heated to 150°C. Each sample was built in a 0°/90° or +45°/-45°C infill pattern with a 100% infill density.

4.2.4. Characterization

The notched Izod resistance of the 3D-printed samples, notched with a 2.54 mm deep tapered notch using a standard notch cutter, was measured following ASTM D-256. A standard ASTM D-256 Izod pendulum impact machine used a 2.5 lb load for the impact tests.

The internal structures of 3D-printed sample were assessed with X-ray Microcomputed tomography (μCT) scanner (Bruker Skyscan1172) operating at 60 kV/167 μA. The difference in electron density between PC and PC/ABS allowed the core and shell structure to be resolved with X-ray tomography. Transmission X-ray images were recorded at 0.4° rotational steps over 180° of rotation. The NRecon software was used to reconstruct the cross- sectional image, which was imported into a Skyscan CT Analyzer (V1.1) to construct the full 3D images. Field emission scanning electron microscopy (SEM, JEOL-7401) was used to further assess the structure of the objects after impact. Before the SEM imaging, the samples were sputter-coated with silver for good surface electrical conductivity.

4.3. Results and Discussion

4.3.1. Effect of printing conditions on the part-filling performance.

During FFF 3D-printing, when a polymer melt filament is deposited onto a workpiece or print-bed, it cools down and solidifies fast to prevent the part from being deformed by melt flow. Therefore, the melt flow often cannot fill the part completely and leaves voids in the finished part. To understand the effect of printing conditions, Bayblend T65PG PC/ABS blend filament were printed in the form of tensile specimen in accordance with ASTM-D638V.

Figure 4-2 shows the X-ray microCT cross-sectional images of 3D-printed PC/ABS Bayblend T65PG tensile samples printed at different extrusion temperature. Careful examination of

Figure 4-2A) illustrates that voids and gaps exist between adjacent filaments in the sample printed at T_{ext}=260°C, while no large voids are observed in the sample printed at T_{ext}=310°C(

Figure 4-2B). Integration of the unfilled area in every cross-section in the scanned section (9mm long) of specimen yield a porosity (unfilled volume percentage) of 6.59% for T_{ext}=260°C and 0.95% for T_{ext}=310°C. The lower porosity at higher extrusion temperature agrees with the lower melt viscosity at higher temperature. Lower viscosity enables the melt to flow more easily during deposition of the filament. It is also reported[60] that the solidification process of polymer melt slows down at higher extrusion temperature because it stays above T_g for longer time, allowing the melt flow fill the part.

Figure 4-3 compares the internal structures of parts 3D-printed at different printing speed (A-20mm/s, B-70mm/s). MicroCT cross-section image of the sample printed at 20mm/s (Figure 4-3 (A)) shows a dense cross-section with only small voids at the bottom of the sample, while the sample printed at 40mm/s (Figure 4-3 (B)) shows big void (>100µm) in the center. It is demonstrated in CHAPTER III that filament extruded at high extrusion speed tends to show radial temperature gradient. Higher porosity obtained for sample printed at faster speed could be attributed to its cooler center that has limited the melt flow during filament deposition.

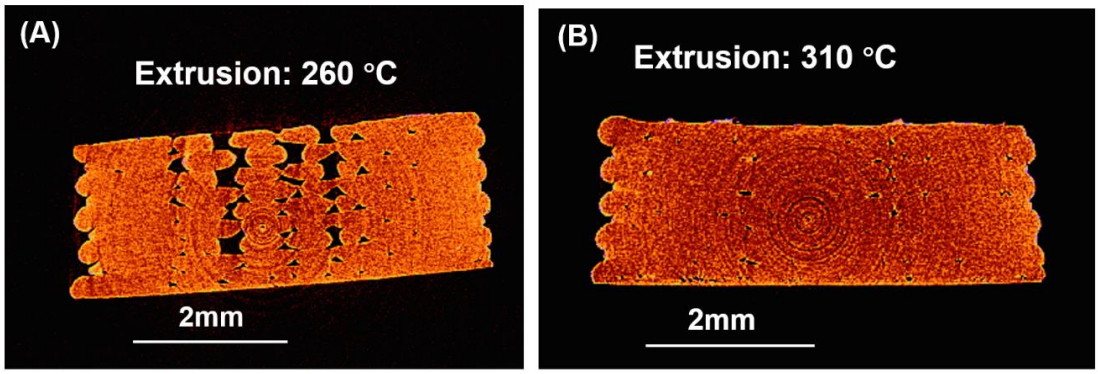

Figure 4-2 X-ray MicroCT cross-sectional images of Bayblend T65PG tensile specimens printed at (A) T_{ext}=260°C; (B) T_{ext}=310°C (T_{bed}=110°C, 45°-45°orientation, v=40mm/s printing speed, d=0.22mm). The porosity calculated

using CTAnlyzer software is: (A) 6.59%; (B) 0.95%

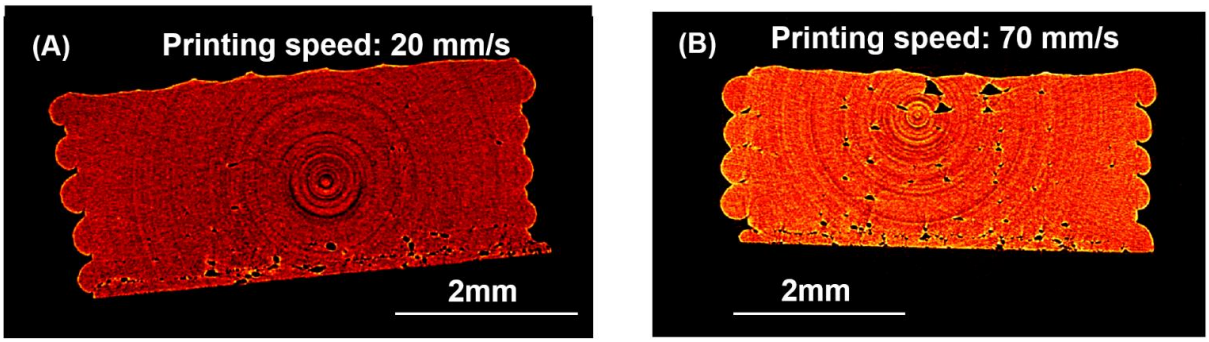

Figure 4-3 X-ray MicroCT cross-sectional images of Bayblend T65PG tensile specimens printed at different speeds (A) v=20mm/s; (B) v=70mm/s at T_{ext}=310°C. (T_{bed}=110°C, 45°-45°orientation, T_{ext}=310°C, d=0.15mm) The porosity calculated using CTAnlyzer software is: (A) 0.75%; (B) 0.91%

Figure 4-4 compares the X-ray microCT images of sample printed at different build-platform temperature (T_{bed}). Higher T_{bed} is expected to slow down the cooling of extruded filament and thus promtes melt flow to infill the part more completely. The microCT cross-section images show more voids in sample printed at higher T_{bed} than lower T_{bed}, which is consistent with total volume porosity. It is noted that the samples printed at T_{bed}=130°C and T_{bed}=150°C, the sample shows an expanded bottom as compared to that printed at T_{bed}=110°C, which is an indicative of sample deformation under the weight of printed parts. The T_g of the Bayblend T65PG PC/ABS is 145°C as measured by DSC (Figure 4-11). At high T_{bed} near the T_g of the polymer, because sample is significantly softened, the bottom of the sample flow outwards under the weight of successive layers. Because the amount of material extruded is fixed to fully infill the part, material flow outwards could lead to insufficient materials in the center.

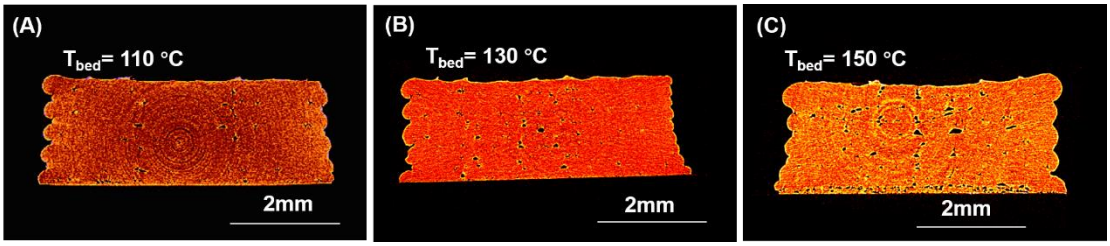

Figure 4-4 X-ray MicroCT cross-sectional images of Bayblend T65PG tensile specimens printed at build-platform temperature (A) T_{bed}=110°C; (B) T_{bed}=130°C; (C) T_{bed}=150°C . (T_{bed}=110°C, 45°-45°orientation, v=40mm/s printing speed, d=0.15mm) The porosity calculated using CTAnlyzer software is: (A) 0.95%; (B) 1.27%, (C) 2.01%.

4.3.2. Effect of printing conditions on the tensile properties of 3D printed PC/ABS

The processing temperature significantly impact the mechanical properties of FFF printed parts.

Figure 4-2 demonstrates that porosity can range from 6.59% to 0.95% as T_{ext} increases from 260°C to 310°C. Figure 4-5 illustrates the tensile properties of PC/ABS samples printed at different extrusion temperature. Elastic modulus and yield stress of the sample increases with increasing T_{ext}, while yield strain doesn't show a clear trend with increasing $T_{ext.}$ The increase of modulus and yield stress at higher T_{ext} can be attributed to the lower porosity of the sample. Unfilled volume in the tensile samples do not bear load. When load is applied to the sample, voids in a printed sample can lead to stress concentration, resulting in mechanical strength inferior to a dense part.[139] Fracture surface of the tensile samples were assessed by using SEM. The fracture surface of tested sample printed at T_{ext}=260°C (Figure 4-6

(A)) shows filament-like structures with separated fracture surfaces. Individual layer and filament can be easily distinguished, which is a indicative of filament delamination during stretching. As T_{ext} increases, the flatter fracture surfaces with less signs of filament-like structures (Figure 4-6 B, C) suggests that less filaments have delaminated because stronger interfaces are formed at higher temperature.

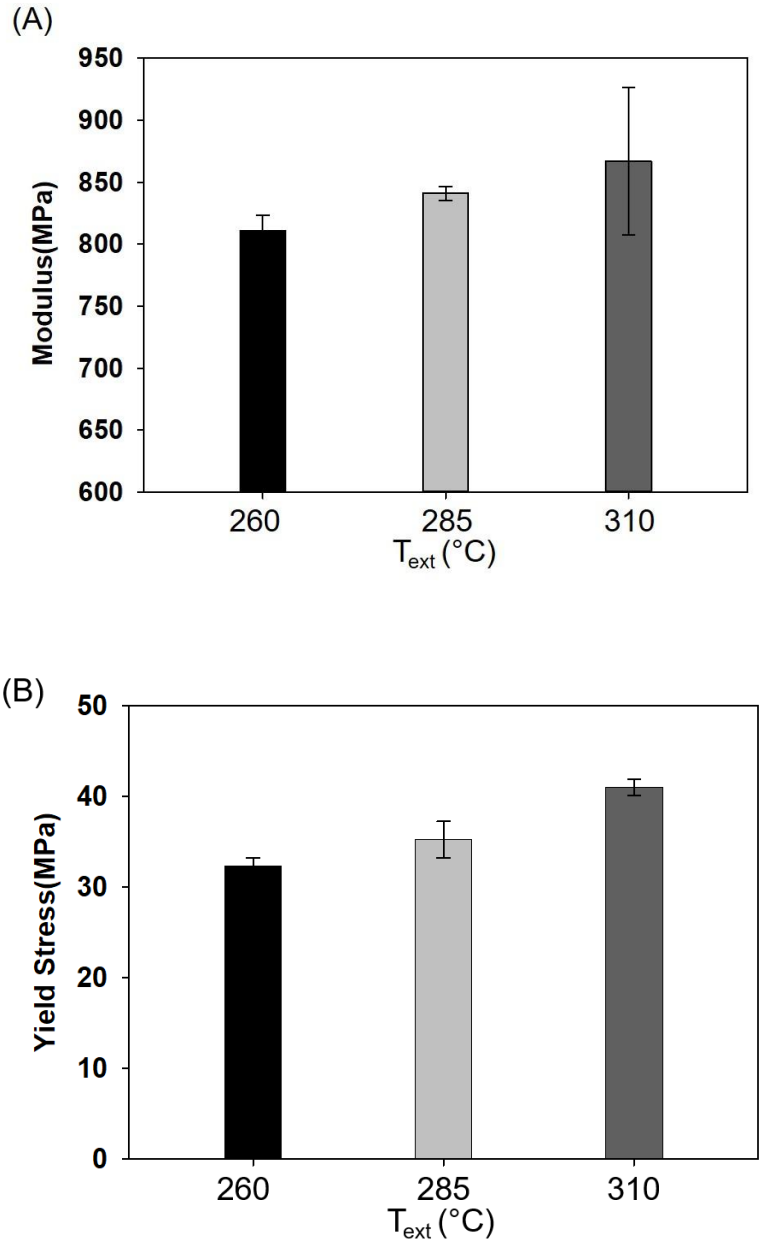

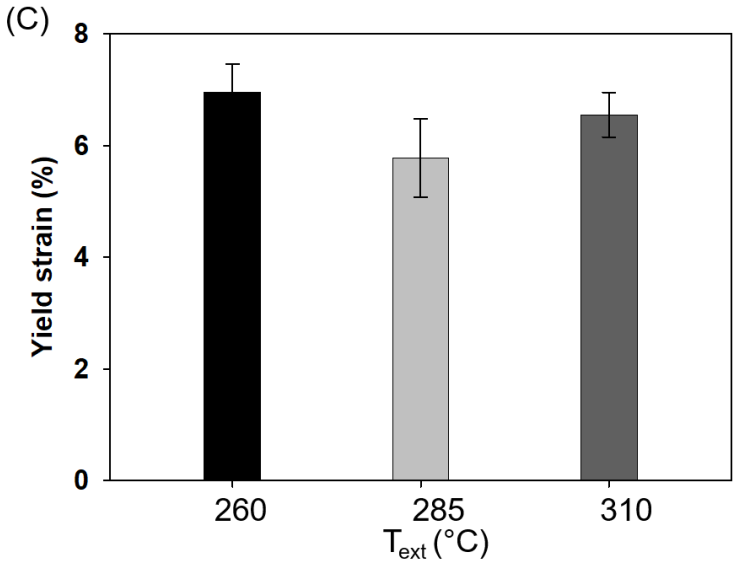

Figure 4-5 Tensile properties of 3D-printed T65PG PC/ABS blend. (A) elastic modulus, (B) Yield stress, (C) Yield strain

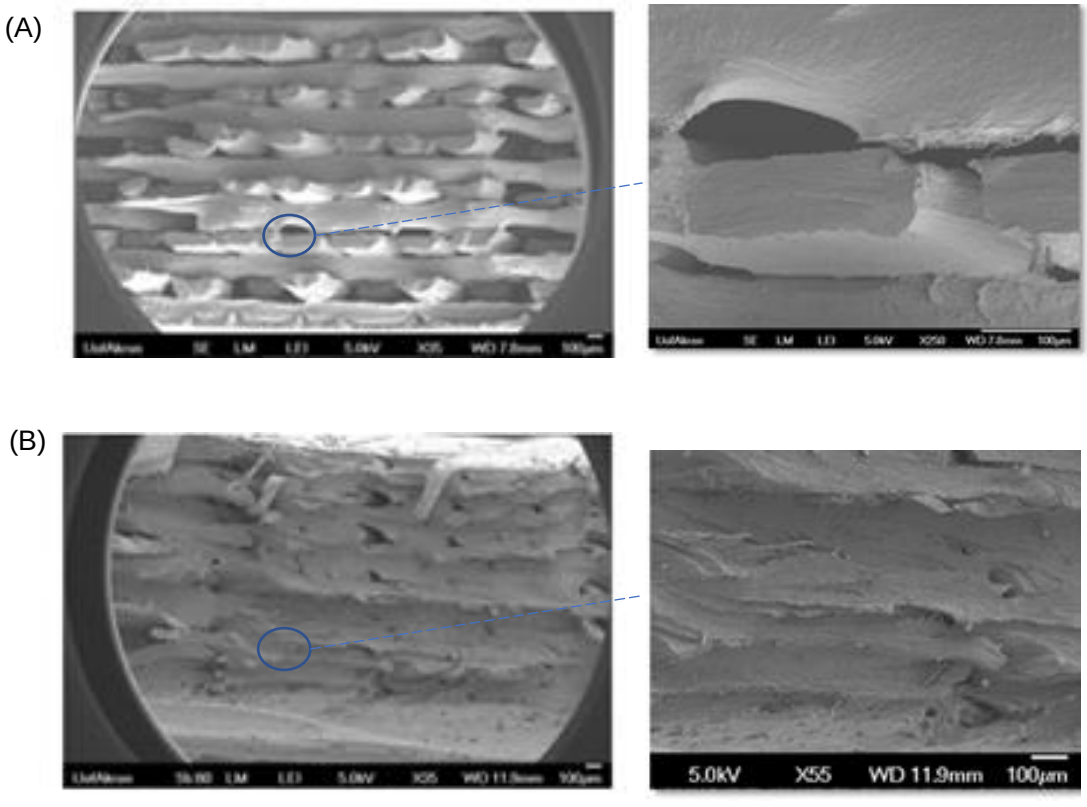

(C)

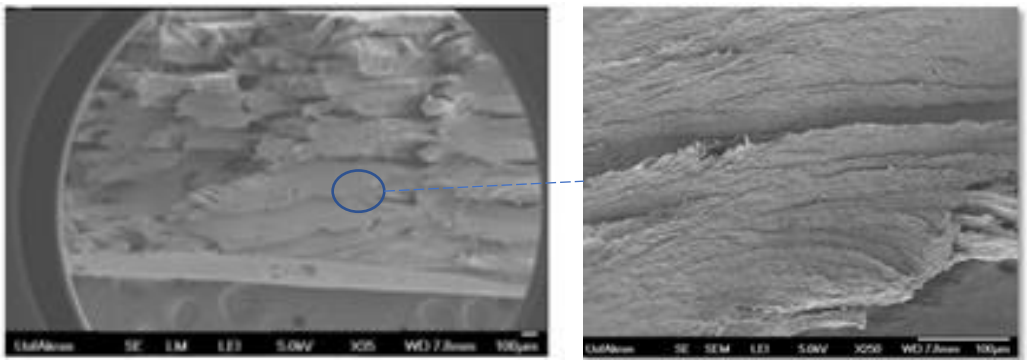

Figure 4-6 SEM fracture images of Bayblend T65PG tensile specimen printed at different extrusion temperatures (T_{ext}): (A) 260°C, (B) 285°C, (C) 310°C

4.3.3. Co-extrusion of core-shell filament

For fabrication of bi-layer core-shell filaments, a co-extrusion system composed of two single-screw extruders, two gear pumps, one co-axial circular die and a cooling bath equipped with a filament-winding roller as illustrated in Figure 4-7.

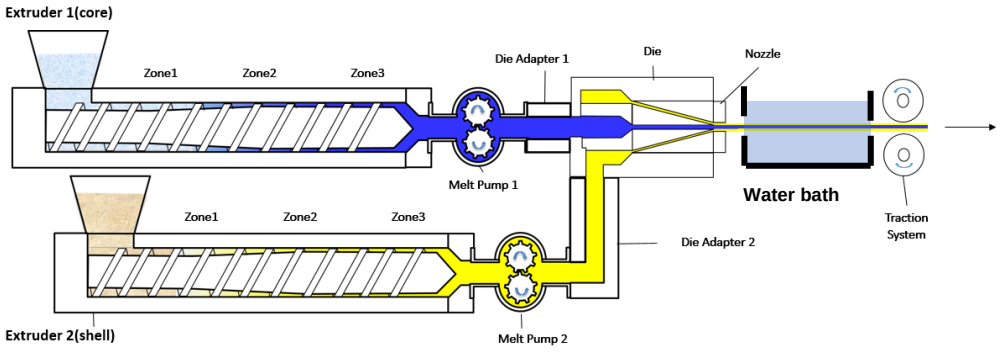

Figure 4-7 Setup of the co-extrusion line and schematic of process to generate core-shell filaments.

Two general-purpose single-screw thermoplastic extruders with three heating zones are used in the co-extrusion system as shown in Figure 4-8. In

the first zone, the screw has deep flights which is designed for deliver solid thermoplastic pellets forward. As the material moves forward, solid heated up and melts by frictional heat and heat conducted from the barrel, and a growing melt film is formed at the barrel surface. In the second section, the depth of the screw flight gradually reduces, thus resulting in a compression of material between the screw and the barrel which favors the homogenization of polymer melt. In the third section, the screw has constant flight depth which generates a stable constant drag flow to deliver melt to the exit. Both extruders are equipped a gear pump at the exit. The advantage of using a gear pump is that it can generate and maintain a relatively constant outlet pressure, improving the consistency of output rate. It has been proved that an independently driven gear can effectively eliminating surges and fluctuation in the output rate of an conventional plasticating extruder[211].

(A)

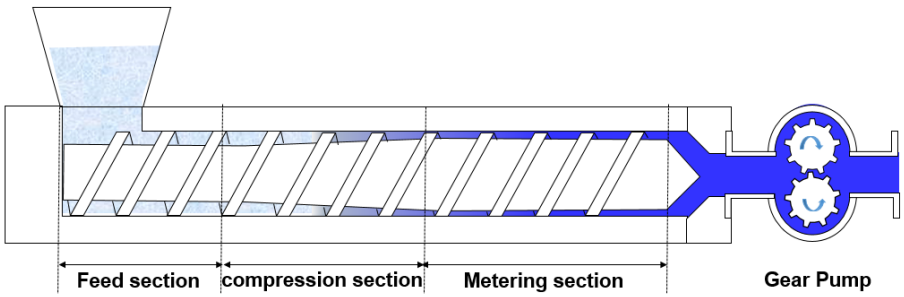

(B)

(C)

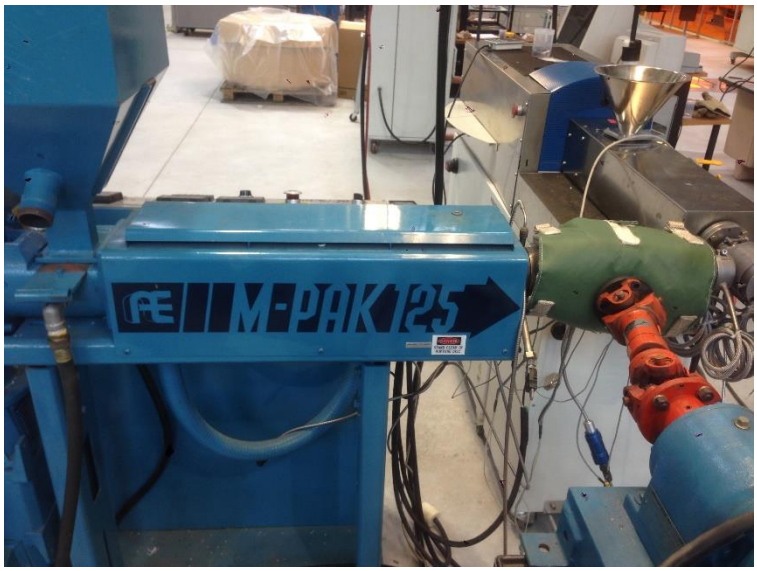

Figure 4-8 (A)Schematic illustrates the three different heating zone of the single screw extruder with a gear pump stabilizing output pressure; Photos of the extruder and gear pumps for (B) core-material (Rheomex 252P), (C) shell-material (Akron Extruder M-PAK 125)

Figure 4-9(A) shows the engineering drawing of the die in the co-extrusion system that can combine the two melt flows from two extruders at the exit of the die in a core-shell form as illustrated in Figure 4-9(B). The melt flow of core-material flows into the die through the flow channel in the center of the die, while

the shell melt flows in the die through the adapter on the side of the die. Due to the asymmetric feeding channel, the shell melt in the die must flow through a spiral flow channel before merging with the core melt flow to prevent uneven pressure across the die.

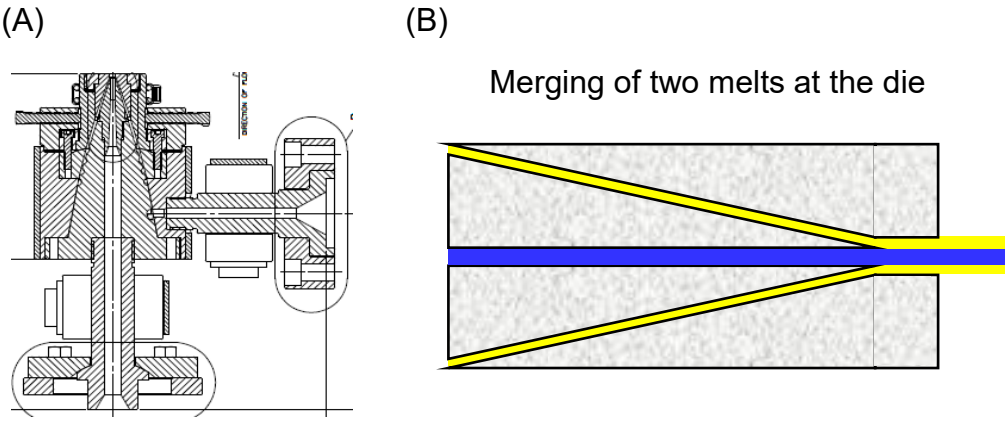

Figure 4-9 (A) Engineering drawing of the co-axial circular coextrusion die; (B) schematic illustrating melt flow of core- and shell- materials at the exit of the die.

Four adjustment screws are installed around the nozzle of the die at a 90 degree-interval for the alignment of the core and shell flow channel. Misalignment of core and shell flow channel would result in eccentric core-shell structures as shown in Figure 4-10(A) and (B). Besides eccentric core-shell structures, bubbles are also observed inside the filament. Because as the hot core-shell melt flow exits the die, it was quickly immersed in a water bath. Rapid cooling leads to sharp temperature gradient across the filament. Uneven cooling generates internal stress that leads to void defects in extruded filament as illustrated in Figure 4-10(B). This problem is set the quenching bath at a

distance larger than 100cm from the die exit, so the filament can be gradually cooled down to a lower temperature in the air prior to entering water bath as demonstrated by Figure 4-10(C) and (D).

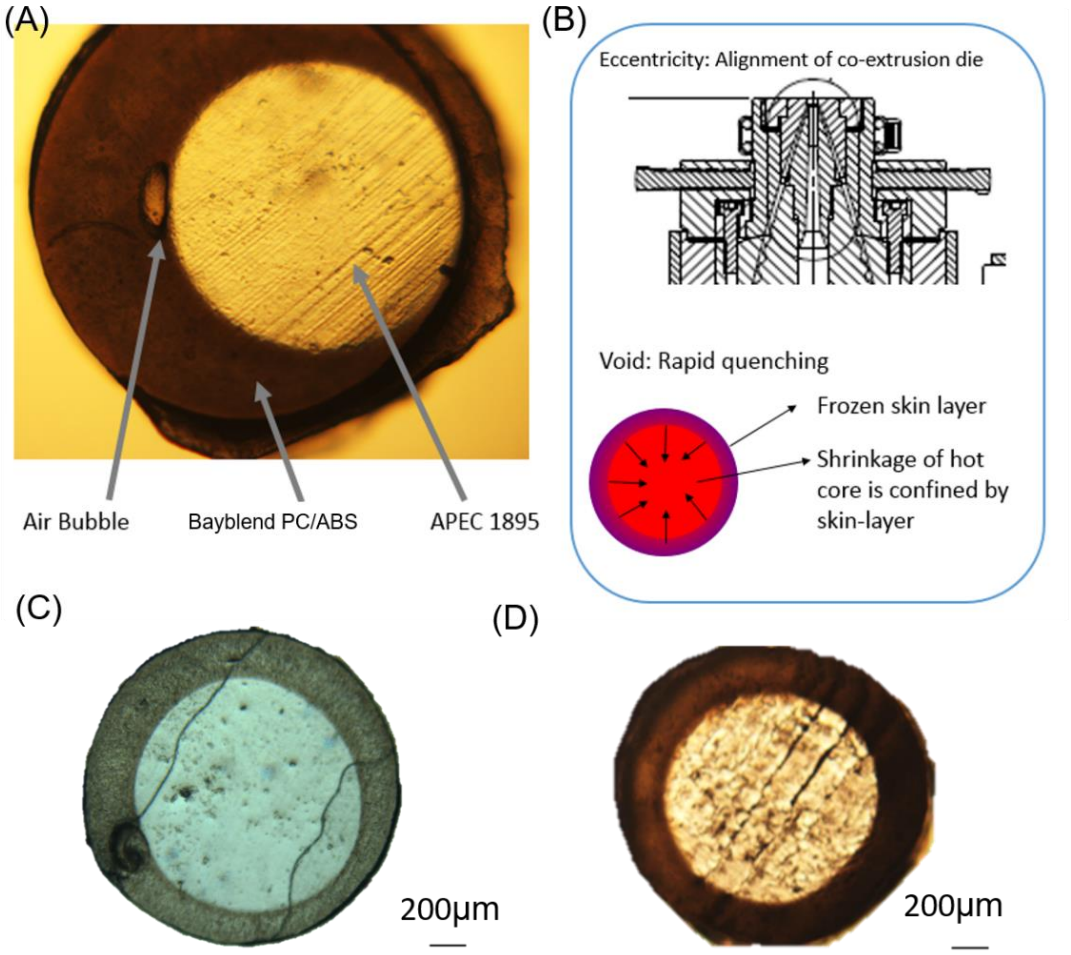

Figure 4-10 (A) Cross-section image of an co-extruded Polycarbonate (APEC 1895)@ PC/ABS blend (Bayblend FR3010) filament with eccentric core-shell structures; (B) Schematic showing misalignment of the die leads to eccentricity in extruded filament as well as showing rapid cooling results in void inside extruded filament; Cross-section image of co-extruded filament with quenching bath set at a distance to the die. Distance range: (C)<50 cm, (D) >100cm

4.3.4. 3D-Printing of PC Core-shell filament

Figure 4-12 (A) and (B) shows the optical microscope and X-ray microCT cross-section image of a tensile sample 3D printed using a PC (APEC 1895)@45%PC/ABS (Bayblend T65PG). In the optical microscope image, the opaque PC/ABS shell remains conformal around transparent PC core. Because of the different electron density between PC and ABS, the bright PC/ABS shell surrounding the darker PC core can be distinguished in Figure 4-12 (B) as well. It demonstrates core-shell structure of the feedstock filament can be maintained throughout the printing process. Figure 4-4 has demonstrated that 3D-printing of PC/ABS(Bayblend T65PG) at a T_{bed}>130°C will lead to a deformed bottom due to the softening of materials at high temperature. In Figure 4-12 (B), the cross-section of the tensile sample printed using PC@PC/ABS filament maintains its rectangular geometry at T_{bed}=180°C, which suggests the high T_g PC core (T_g-APEC1895= 189°C) can maintain the geometry of the PC/ABS matrix even above its T_g (145°C).

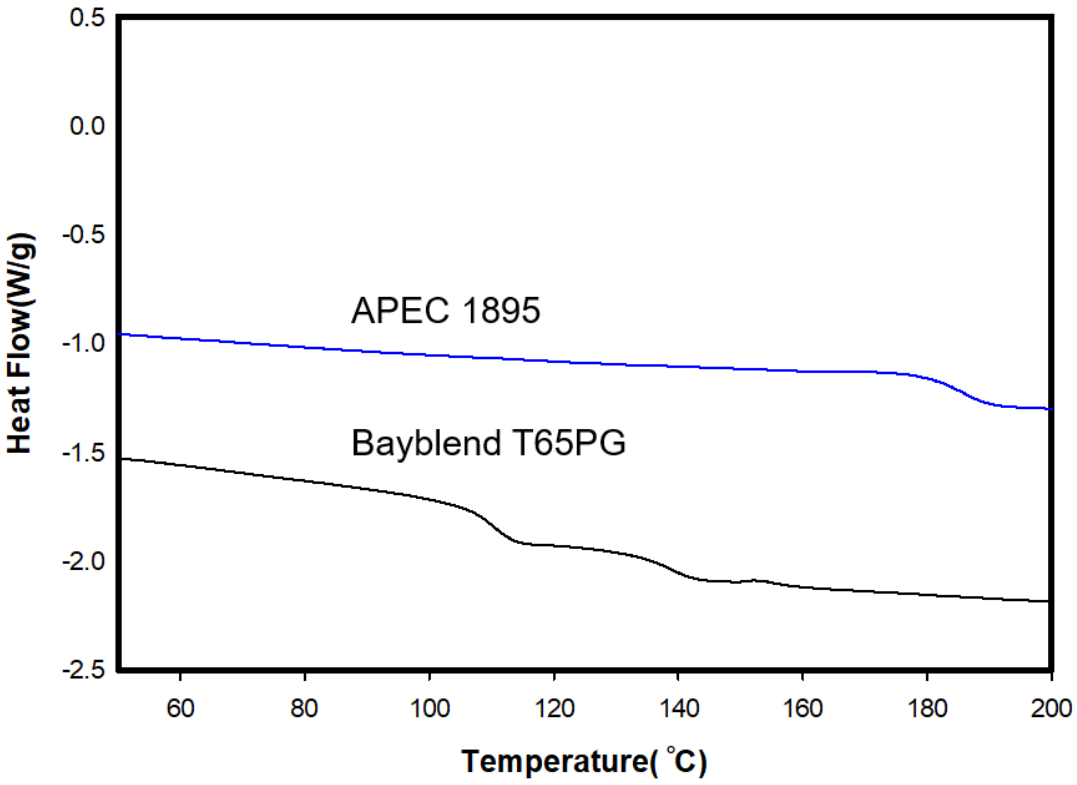

Figure 4-11 DSC thermograms of APEC 1895 showing a T_g of 189³C and Bayblend T65PG showing its highest T_g at 145°C

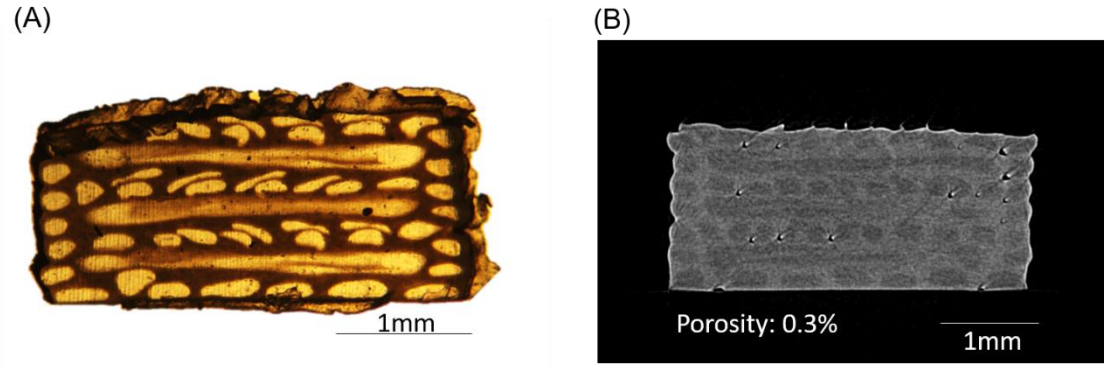

Figure 4-12 (A) Optical microscope image, (B) MicroCT cross-section image of a tensile bar printed from APEC 1895(55%)@Bayblend T65PG core-shell filament under following conditions: T_{ext} = 310°C, T_{bed} = 180°C, 0/90° infill, d=0.21mm, v=40mm/s.

4.3.5. Impact resistance of 3D-printed core-shell samples

Mechanical properties of 3D-printed parts are highly anisotropic due to the existence of weak bonding interfaces between layers and filaments.[51] In order to understand the anisotropy of the impact resistance that develop through 3D printing of core-shell filaments, impact test samples were printed in three different orientations as illustrated in Figure 4-13(A). Figure 4-13(B) illustrates how the printing orientation affect the impact resistance of 3D-printed APEC1895@FR3010 specimen. At different PC core concentration, YZ alignment exhibit the worst impact resistance. Because the load is applied normal to the layer interfaces for sample printed at YZ orientation, the impact strength in this case relies significantly on the bonding strength between layers.

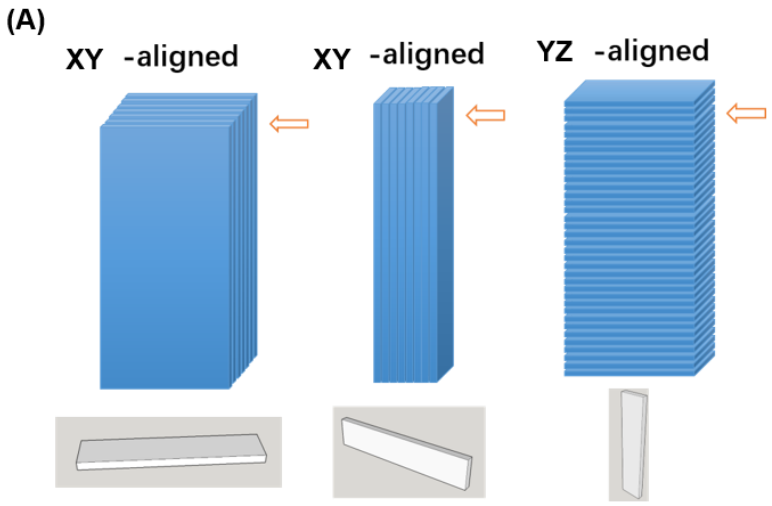

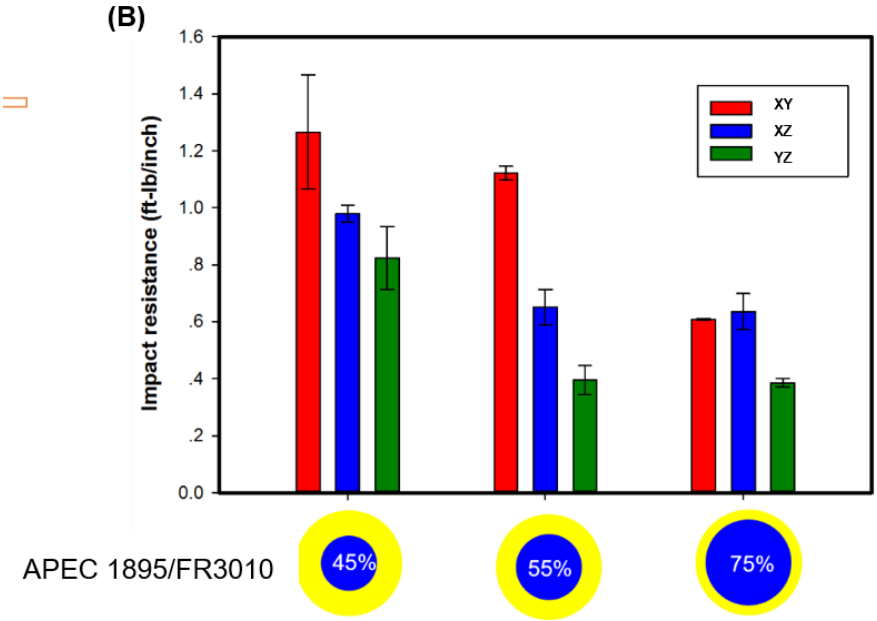

Figure 4-13 (A) schematic illustration of (XY-flat, XZ-edge on, YZ-end on) (B) Impact resistance of APEC1895@FR3010 core-shell samples printed in different orientations(T_{ext} = 310°C, T_{bed} = 180°C, 0/90° infill, d=0.21mm, v=40mm/s).

To demonstrate that a shell with lower viscosity and lower solidification temperature can increase the interfacial bond strength, impact resistance of samples printed at YZ orientation are compared. High viscosity Makrolon 3208 BPA polycarbonate (PC) is used as the core, while low viscosity Makrolon 2205 BPA-PC and low T_g/low viscosity Bayblend FR3010 PC/ABS blend are used as shell materials. Figure 4-14 illustrates the thermal properties and viscosity of the selected polymers. Both high- and low- viscosity PC show a T_g of 150°C while Bayblend FR3010 PC/ABS blend shows a T_g of 110°C (Figure 4-14 A). The viscosity of Makrolon 3208 is one order of magnitude higher than that of Makrolon 2205, which is an indicative higher molecular weight.

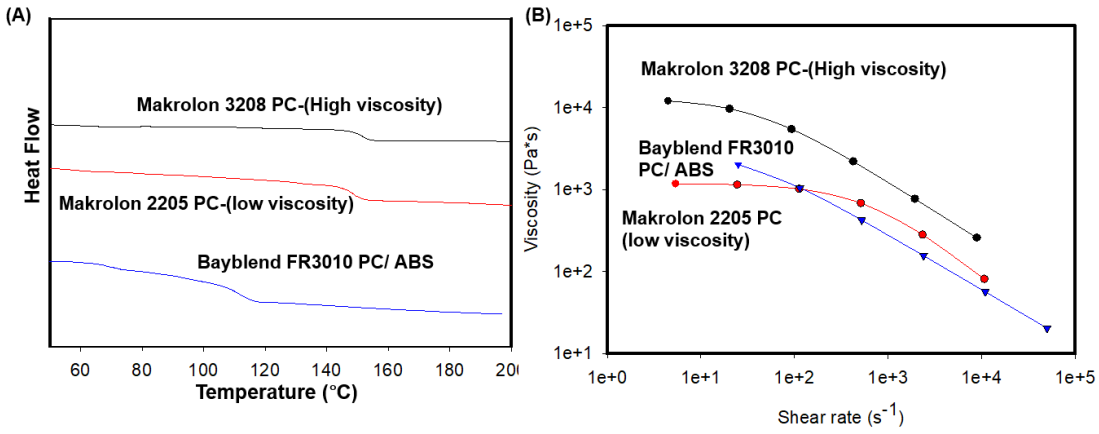

Figure 4-14 (A) DSC thermograms for Makrolon 3208, Makrolon 2205 and Bayblend FR3010. (B) Shear viscosity of Makrolon 3208, Makrolon 2205 and Bayblend FR3010 at 280°C from a capillary rheometer.

In Figure 4-15 (A), the impact resistance of samples printed with core-shell filaments are compared with that of samples printed with pure low Makrolon 3208 and Makrolon 2205. Because chain self-diffusion coefficient in polymer melt) is dependent on molecular weight ($D \sim M^{-2}$ for entangled polymer chain according to reptation theory[161,212]). Makrolon 2205 shows higher impact resistance as compared to Makrolon 3208 because its lower molecular weight promotes the chain diffusion at the layer interface and improves the interfacial strength. Sample printed with core-shell Makrolon 3208(55%)@Makrolon2205 and Makrolon 3208(45%)@Makrolon2205 filaments both show impact resistance superior to that of single component samples. It demonstrates that utilizing high-viscosity@low-viscosity core-shell filament enables incorporation of a core with better bulk mechanical properties. Therefore, 3D printing with core-shell filament could achieve synergistic improvement of mechanical properties by combining the bond strength of shell material and bulk properties of core materials.

Figure 4-15 (B) compares the impact resistance for samples printed with PC@PC/ABS core-shell filaments, pure PC and PC/ABS at two different T_{ext}. Due to the low T_g of PC/ABS blend, printing vertically aligned impact specimen with PC/ABS at T_{ext}=280°C leads to severe overheating-induced distortion. Therefore, impact specimen of PC/ABS were only printed at 240°C. Because the viscosity of Makrolon 3208 PC is too high for extrusion at T_{ext}=240°C, the impact samples were only printed at T_{ext}=280°C. In contrast, PC@PC/ABS core-shell filaments with different PC content can be printed at both T_{ext}=240°C and 280°C, which is an indicative of broadened processing window of core-shell filament. It is reported that for polymer melt flow in a cylindrical tube, a low-viscosity outer layer that covers the high-viscosity core layer can significantly decrease the pressure required to drive the flow [213]. In this case, a thin layer (25vol%) can be enough to allow the high-viscosity PC to be extruded through the 3D-printer liquefier at T_{ext}=240°C. For the samples printed at T_{ext}=240°C, the impact resistance of the sample printed with pure PC/ABS is at the same level as compared to PC@PC/ABS. However, impact resistance of the samples printed with PC@PC/ABS at T_{ext}=280°C is higher than that of PC samples. It suggests that at the PC/ABS shell, which shows lower T_g and viscosity, can lead to a stronger layer-interfaces at T_{ext}=280°C. Meanwhile, the impact resistance of the core-shell samples when they are printed at T_{ext}=280°C is much higher than when printed at 240°C. The improvement of mechanical properties at high T_{ext} proves that a core with higher T_g can enable a low T_g material to be printed at higher temperature, which favors the bond strength development during printing.

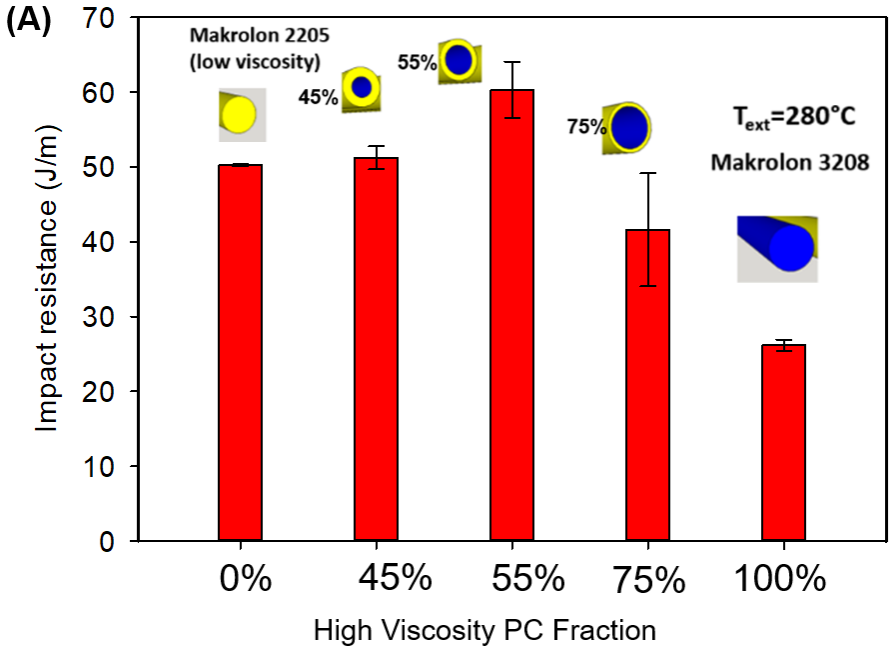
(A)
Impact resistance (J/m)
70
60
50
40
30
20
10
0
Makrolon 2205
(low viscosity)
45%
55%
75%
T_{ext}=280°C
Makrolon 3208
0%
45%
55%
75%
100%
High Viscosity PC Fraction

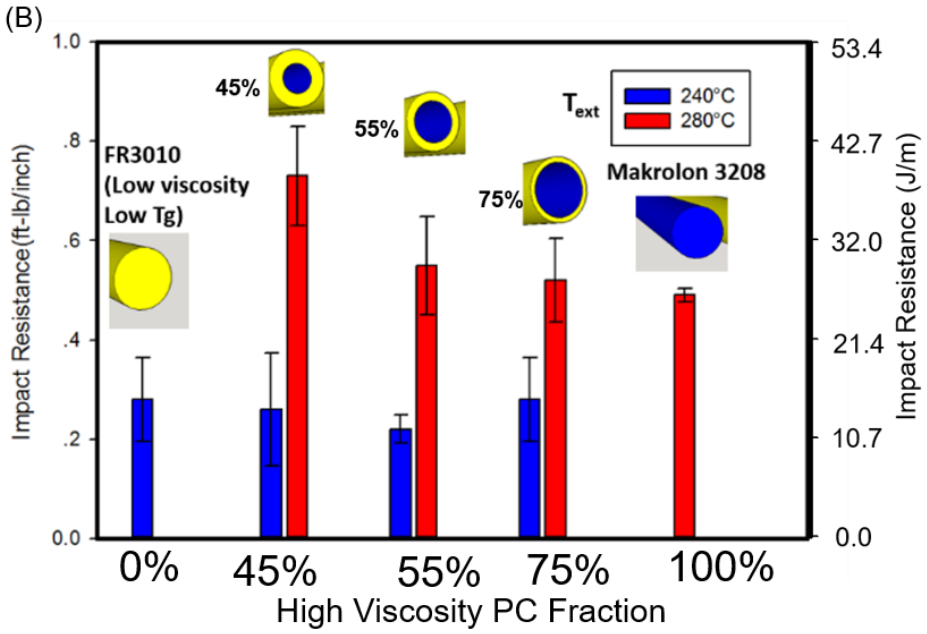

Figure 4-15 Impact resistance of impact samples printed at YZ orientation (T_{ext} = 310°C, T_{bed} = 180°C, 0/90° infill, d=0.21mm, v=40mm/s): (A) Makrolon3208@Makrolon2205; (B) Makrolon3208@FR3010;

4.4. Conclusion

In this chapter, we demonstrate that high processing temperature can improve the part-filling and mechanical properties of FFF manufactured parts by prompting melt flow and chain diffusion during filament deposition. However, high processing temperature can also lead to overheating-induced part distortion. Using core-shell filament fabricated by co-extrusion technologies is demonstrated to be an effective approach overcome the inherent poor thermal dimensional accuracy associated with low T_g materials and the poor bond strength associated with high viscosity/T_g materials. An outer shell with low T_g or low viscosity and promotes the chain diffusion during bond formation in FFF, while the high T_g/high viscosity PC core can maintain shape accuracy at high

temperature and provide better bulk mechanical properties to the 3D-printed part.

CHAPTER V

ENHANCED IMPACT RESISTANCE OF 3D PRINTED PARTS WITH STRUCTURED FILAMENTS

(The content in this chapter is partially reproduced with permission from ACS Appl. Mater. Interfaces 2018, 10, 16087−16094[142])

5.1. Introduction

Three-dimensional (3D) printing has been a key enabler of rapid prototyping for developing new designs and concepts,[214] but the production of functional objects by 3D printing has been limited by the availability of high-performance feedstocks and poor understanding of topology optimization.[215] Recently, there has been a significant push toward bridging the gap to enable 3D printing to be extended to final products.[216] Most technologies to print plastic parts build in a layer-by-layer manner, which leads to weak points at the interfaces of each layer.[81] These internal interfaces, similar to weld lines, act to limit the performance of 3D-printed parts. Despite this challenge of the interfacial strength during the part build, significant advances have been made in the past decade, especially with respect to the potential for personalized medical devices made to fit the patient.[217] These can range from models to aid in complex surgeries[76] to scaffolds for bone[218] and soft tissue[219] engineering. Beyond the biomedical potential, 3D printing offers advantages of

lightweighting by printing cellular solids that can outperform standard materials[220] and the ability to generate complex, multicomponent objects with advanced functionality such as soft, autonomous robots.[21] For plastic materials, there has been a push to enhance the functionality of the material being printed. This has included increased maximum operating temperature,[221] improved elasticity,[222] increased stiffness,[220] and responsiveness of the printed parts.[223224] In particular, responsive materials enable four-dimensional printing,[225] which represents a new paradigm for adaptive structures. Similarly, functionality enabled by 3D printing has been exploited in the production of lightweight metamaterials that exhibit unique properties including negative coefficient of thermal expansion.[226] However, the printing method tends to remain a limitation where the mechanical properties of 3Dprinted parts are inferior to those from traditional manufacturing methods.

One common technique for 3D printing of polymers is fused filament fabrication (FFF) where a thermoplastic filament is rapidly melted through a rastering hotend and deposited on the build stage to build the part in a layer-by-layer fashion.[147] This simple technique relies on the deposited molten polymer melting the underlying layer to generate a viable interface, whereas the flow of the molten polymer must be limited to prevent deformation of the part. The orthogonal nature of these requirements leads to trade-offs between shape accuracy and the mechanical properties of the part.[37] Much of the work on FFF has focused on trying to optimize the processing conditions to generate the best mechanical properties in the 3D-printed part, [147] but these are inferior, generally by almost an order of magnitude, to the comparable injection molded

part. Most efforts to date to improve the properties of FFF parts have focused on using new polymers and engineering designs of the printers,[147,227]but these approaches fail to address the intrinsic underlying flaw in FFF of the poor interfaces between layers. In particular, these 3D-printed parts suffer from poor impact performance, which limits their use in demanding applications.

Here, we describe a novel approach that directly addresses the weak interfaces through a material design approach using core−shell structured filaments. These filaments overcome the general trade-off between shape accuracy and the mechanical properties through a high glass-transition temperature (Tg) core that acts as a “stiff skeleton” to reinforce the printed shape and a low Tg shell that enables improved interdiffusion of polymers between adjacent printed layers. The shell polymer contains both crystallinity and ionic functionality to further improve these interfaces as these functionalities provide routes to improve the bridging across the interface. These attributes enable 3D printing of polymeric parts with unprecedented impact resistance (>800 J/m) with the immiscibility between the core and the shell layer, providing an additional mechanism for energy dissipation through local delamination on impact. This material design approach using structured filaments opens a new paradigm for the 3D printing of functional polymeric objects.

5.2. Experimental Section

5.2.1. Materials and Characterization.

Bisphenol-A polycarbonate (PC, Covestro Inc., Makrolon 3208) and an ionomer of partially zinc-neutralized polyethylene-co-methacrylic acid (DuPont, Surlyn 9910) were used as the polymers for 3D printing. Prior to extrusion or 3D printing, pellets (as obtained from Covestro, Inc., and DuPont) or filaments were dried in a vacuum oven for 12 h to remove residual water (PC at 110 °C; Surlyn 9910 at 60 °C), which can lead to a reduction in the molecular weight of PC during melt processing. Differential scanning calorimetry (TA Instruments DSC, model Q2) with hermetic aluminum pans performed at a heating and cooling rate of 10 °C min−1 under a nitrogen atmosphere was used to assess the thermal properties.

5.2.2. Filament Extrusion.

Filaments of pure PC or Surlyn were extruded using a HAAKE single-screw extruder (Model Rheomex 252p) that was equipped with a gear pump and a simple circular die (diameter = 2.2 mm). The temperature profile used for extrusion of each filament is shown in Table 5-1.

Table 5-1 Temperature profile for filament extrusion

Filament	Zone 1 [°C]	Zone 2 [°C]	Zone 3 [°C]	Gear Pump [°C]	Die [°C]
PC	280	290	275	280	240

Surlyn		220	230	240	240	200
PC@Surlyn	PC	280	290	275	280	220
	Surlyn	220	230	240	240	

Two single-screw extruders (Rheomex 252p and Akron Extruder M-PAK 150) with a coextrusion die with a circular opening (diameter = 2 mm) as shown in were used to fabricate the core−shell PC@Surlyn filaments. Each extruder was connected to a separate gear pump to control the flow rate ratio of the PC and Surlyn melts (25, 45 and 55% Surlyn). The extruded filaments were quenched in a room-temperature water bath and drawn onto a take-up wheel. The diameter of the extruded filament was drawn down to approximately 1.7 mm by controlling the take-up speed relative to the extrusion rate. The diameter of the filaments was controlled to 1.70 ± 0.03 mm.

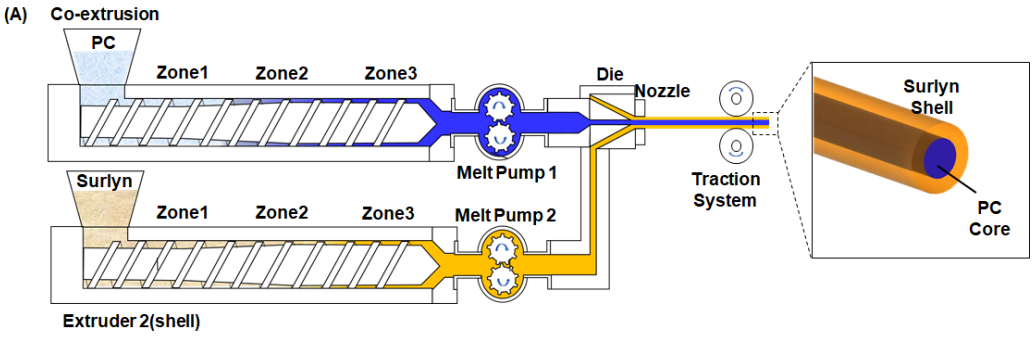

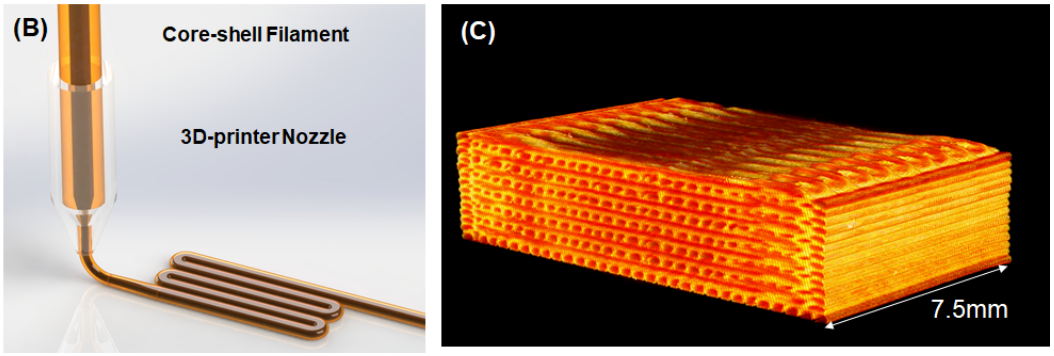

Figure 5-1 (A) Schematic of the coextrusion process to fabricate PC@Surlyn core-shell filaments; (B) Schematic illustrating 3D printing of the core-shell by FFF; (C) X-ray tomography of 3D printed core-shell (PC@45%Surlyn) filament to illustrate the maintenance of the structure in the printed part. The low electron density of Surlyn (bright) relative to PC(dark) provides contrast to distinguish components with X-rays.

5.2.3. 3D Printing.

A customizable 3D printer, Cartesio 3D printer model: W09, equipped with an E3D-v6 (1.75 mm type) hot-end (liquefier) assembly that was heated using a 24 V−40 W cartridge heater (E3D) and a 0.4 mm nozzle was used to print the samples. For impact tests, samples in accordance with ASTM-D256 were 3Dprinted at three different orientations, as shown in Figure 5- 2. The thickness of the samples printed in XY and XZ directions was 3 mm, whereas the thickness in the YZ direction was 12.7 mm. All samples in XY and XZ directions were printed with an extrusion temperature of 280 °C at 20 mm/min. Because of the localization of the heat from the extruder in the YZ direction, these samples were printed at 260 °C at 10 mm/min to maintain the shape of the part. For tensile tests, samples were 3D-printed in the XY direction with a thickness

of 1.5 mm in accordance with ASTM-D638V. For the production of tensile bars, the print bed was covered with a Kapton tape and heated to 100 °C during printing. A thin layer of washable poly(vinyl alcohol) adhesive (Elmer's glue stick) was applied to the Kapton to enhance adhesion of the part to the print bed. Each sample was built in a 0°/90° infill pattern with a 100% infill density. After the build, the part was rinsed with water to remove any residual PVA adhesive.

5.2.4. Characterization

The notched Izod resistance of the 3D-printed samples, notched with a 2.54 mm deep tapered notch using a standard notch cutter, was measured following ASTM D-256. A standard ASTM D-256 Izod pendulum impact machine used a 5 lb load for the impact tests. Tensile properties of the 3D-printed samples were tested using an Instron 5567 with a crosshead velocity of 10 mm/min during the tensile experiment. The structure of the impacted samples was assessed with an X-ray Microcomputed tomography (μCT) scanner (Bruker Skyscan1172) operating at 50 kV/200 μA. The difference in the electron density between PC and Surlyn allowed the structure of the core and shell to be resolved with X-ray tomography. Transmission X-ray images were recorded at 0.4° rotational steps over 180° of rotation. The NRecon software was used to reconstruct the crosssectional image, which was imported into a Skyscan CT Analyzer (V1.1) to construct the full 3D images. Field emission scanning electron microscopy (SEM, JEOL-7401) was used to further assess the structure of the objects after impact. Before the SEM imaging, the samples were sputter-coated with silver for good surface electrical conductivity. The shape of the 3D-printed parts was interrogated with an ATOS Core 200 3D

scanner (GOM). Before scanning, the sample was primed (RUST-OLEUM White Primer) and decorated with six reference points to improve the geometry capture. The samples were scanned from both the top and the bottom. The 3D images were reconstructed by combining these two scans using ATOM Hotfix 6 software.

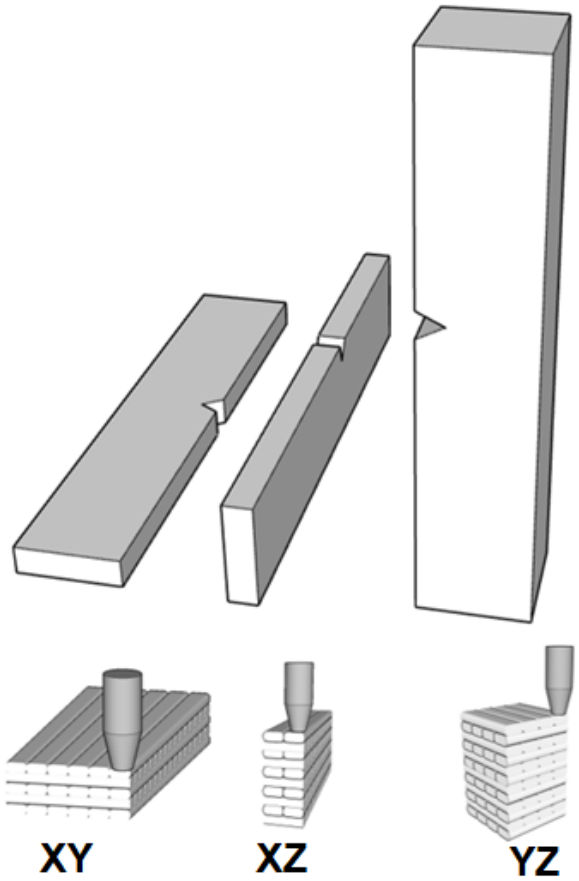

Figure 5- 2 Schematic illustrating the 3 different printing orientations examined: XY (flat), XZ (edge-on), and YZ (end-on).

5.3. Results and Discussion

The enhancement in the mechanical properties of the 3Dprinted parts relies on the improvement in the interfacial properties between printed layers enabled by the structured filaments. Figure 5-1A illustrates the extrusion

process by which the structured filaments are produced. Both PC, which comprises the core, and Surlyn, which is an olefin ionomer and comprises the shell, are melted in standard extruders with the volumetric output from each extruder controlled by melt pumps. These melt pumps are critical to both maintain a constant filament diameter in the product and control the relative composition of the filaments produced and hence the thickness of the shell. By individually determining the relationship between volumetric throughput and motor speed for each melt stream at their respected processing temperatures, the relative volume fractions of the core−shell filament can be precisely controlled. The two melt streams are combined in a specially designed coextrusion die to generate the core−shell filaments. These thermoplastic structured filaments are then used as the feedstock for 3D printing via FFF.

5.3.1. Printing of Objects Using Structured Filaments.

Figure 5-1B illustrates schematically the printing process for the structured core−shell filament. The printing process with these core−shell filaments is identical to the standard FFF printing where the filament is fed into a heated nozzle where it is melted and then deposited on the build platform. The extrusion temperature for the core−shell material is set to be the same as an optimized temperature for printing of simple filaments of PC. This temperature is greater than can accurately print the Surlyn alone (Figure 5-3) due to the much lower thermal transition in Surlyn in comparison to PC (Figure 5-4) for solidification (approximately 90 °C). This inability to accurately print Surlyn at the extrusion conditions is associated with the flow of the material, which leads to significant deviations in the shape for the pure filament, but this ability of the Surlyn to flow (diffuse) substantially at these print conditions should act to improve the quality of the interface between printed layers. It should be noted that these print conditions are not suitable for printing complicated geometries with pure Surlyn, whereas these are optimized for the elastic modulus of pure PC while maintaining the shape accuracy. Figure 5-1C illustrates the X-ray μCT image of a printed part using a PC@45% Surlyn filament, where PC is the core and the Surlyn shell is 45 vol % of the filament. Because of the difference in electron density, the bright Surlyn shell surrounding the PC core in the printed layers can be clearly distinguished. The shell remains conformal around the PC core even as the total diameter decreases from 1.65 to 0.61 mm as the filament is extruded in the 3D print process. To better illustrate that the extruded materials are consistent with the initial filament, cross-sectional images of the

coextruded filaments and the corresponding 3D printer-extruded filament are compared in Figure 5-5. After being extruded by the 3D printer, the dimension of the core decreases from 1.22 mm (54.6 vol % PC) to 0.45 mm (54.4 vol % PC). This indicates that the volume fraction of PC remains constant during the 3D printing process. This consistency is despite the differences in the rheological properties of PC and Surlyn at 280°C (printing temperature) as shown in Figure 5-6, where the viscosity of PC is higher than that of Surlyn. This configuration is favorable as the stress from the high shear rate near the wall is lowered by the low viscosity shell.[228] Careful examination of the micrograph in Figure 5-1C illustrates that there are no observable gaps or voids in the printed part, which is consistent with the flow of Surlyn to fill these gaps. A 0.23% unfilled volume fraction is obtained by integrating the void area across the sample with a series of CT cross-sectional images. Despite the high flowability of Surlyn at the processing temperature, the shape of the printed object is remarkably close to the digital input with no statistical difference in the fidelity of the shape between the core−shell and pure PC filaments. One additional advantage of the core−shell material in comparison to the pure materials is the warpage of the final part. As shown in Figure 5-7A, a printed wedge-shaped bar using PC@45% Surlyn remains flat after the removal from the build platform, whereas bars printed with the individual components exhibit significant bending. Figure 5-7B illustrates a comparison between the original 3D file and the 3D scanned image of the printed wedge-shaped bars. It demonstrates that the geometry of the original 3D model file is replicated by printing of the core−shell filament, whereas bars printed with individual component show bent length or distorted edges. This bending is associated

with the residual stress developed in the part; the isolation of the high-Tg and high-modulus PC decreases the stress transfer on cooling during the 3D printing process. The limited bending in the core−shell materials is even more remarkable given the semicrystalline nature (15.9% of polyethylene segments) of Surlyn that leads to some contraction on crystallization. This demonstrates that the structured filament can provide some advantages in terms of the printed structure accuracy. To explain the improved printed accuracy of the part, the solidification process and stress accumulation must be considered. For the PC@Surlyn filaments, both components are printed in the melt state and PC solidifies much more rapidly than Surlyn. The solidification of PC occurs with the PC surrounded by a melt of Surlyn, so any volume changes associated with PC are not transferred to the bulk structure as it is floating in the Surlyn melt to dissipate the stress. As PC continues to cool, the typical stresses associated with the thermal expansion can be dissipated by the surrounding melt. The crystallization of Surlyn tends to lead to major deformation of the structure for the pure Surlyn filaments, but the structure of objects from the core−shell appears to not be impacted by this crystallization. The high relative modulus of the PC core minimizes the deformation associated with the crystallization of Surlyn because of the energetic penalty associated with the bending of the PC fiber core. This combination of properties minimizes the bending and deformation of the parts printed from the core−shell filaments.

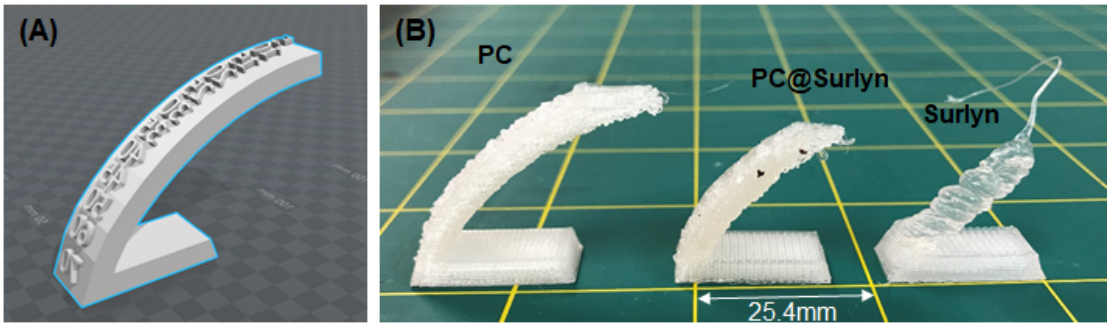

Figure 5-3 **.** (A) Design of overhang test specimen; (B) Printed overhang test specimens using pure Surlyn, core-shell (Surlyn@ 45% PC), and pure PC filaments. Maximum overhang angle for PC is 35°, for PC@45% Surlyn is 25° and for Surlyn is 60° (The extrusion temperature of the hot-end was set to 280°C, nozzle speed is 20mm/min, and the temperature of the print-bed is set to 60°C)

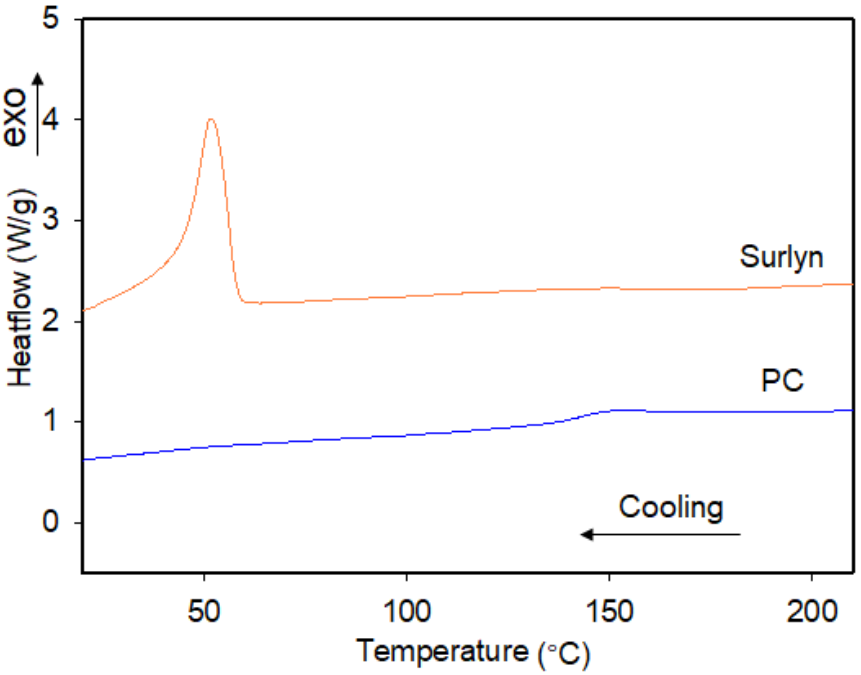

Figure 5-4 Thermograms for PC and Surlyn that was obtained by separating the components from the fabricated filaments of PC@ Surlyn. Here, the heat flow of PC is offset by 1 W/g.

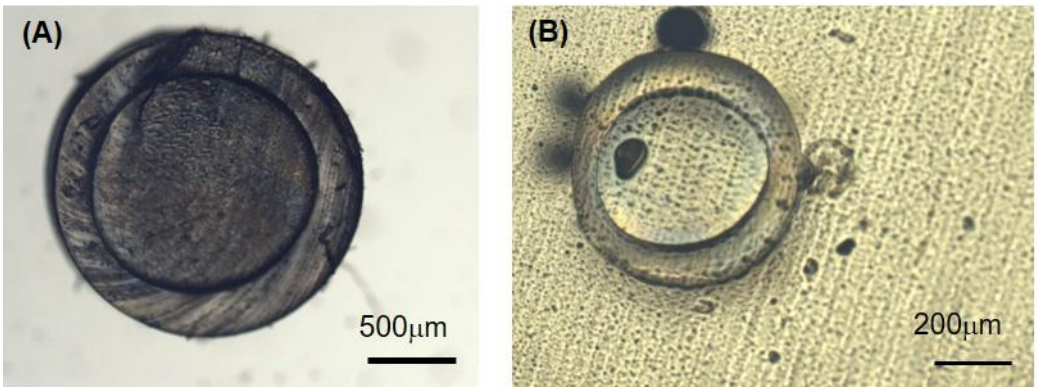

Figure 5-5 Cross-section images: (A) co-extruded filaments with 45% Surlyn; (B) core-shell filament extruded by 3D-printer

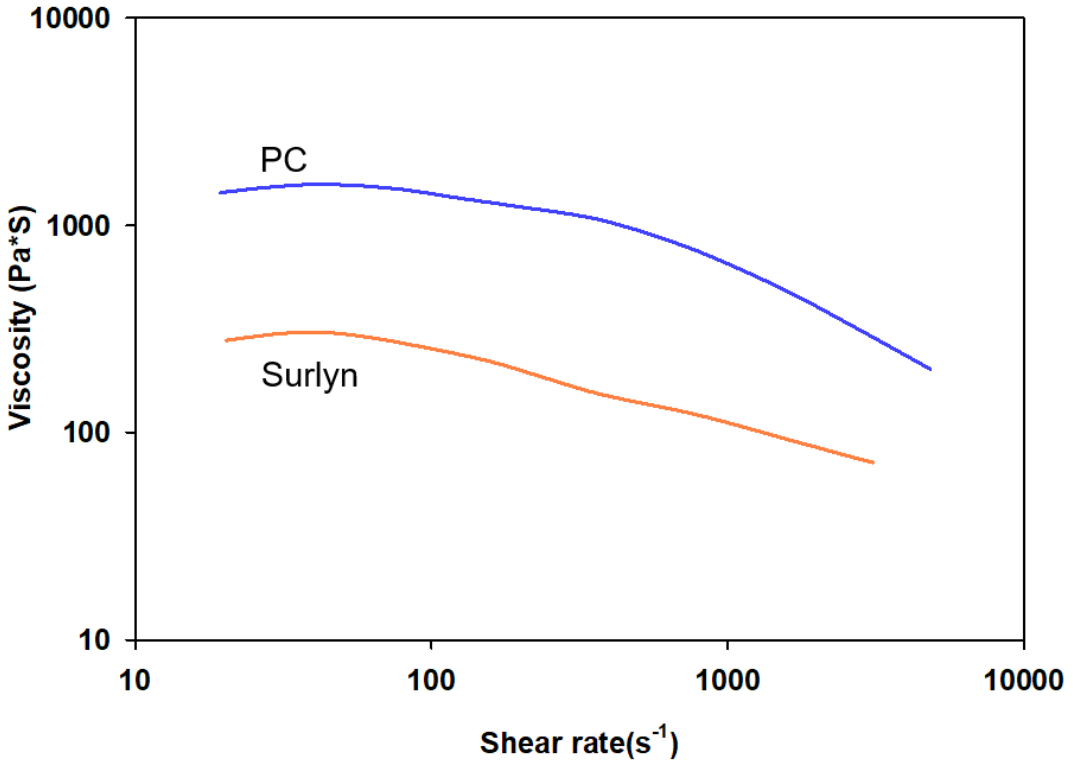

Figure 5-6 Shear Viscosity of PC and Surly measured at 280°C by using a capillary rheometer (Rosand RH7 by Malvern)

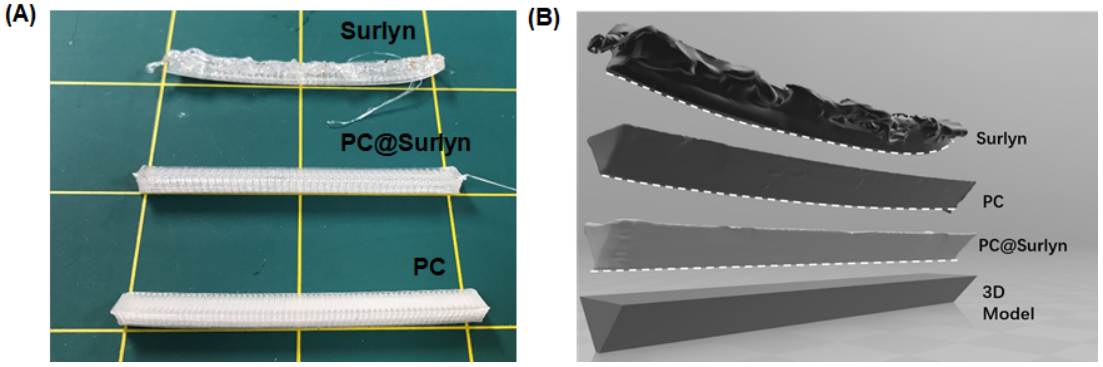

Figure 5-7 (A) Comparison of the bending of 3D printed parts using pure PC, pure Surlyn, and core-shell (PC@ 45 % Surlyn) filaments; (B) Comparison of the printed parts and the original 3D model

5.3.2. Impact Properties from Structured Filaments

When examining the properties of 3D-printed parts, the orientation of the object during the print can dramatically influence the observed properties. Here, three common print orientations as illustrated in Figure 5- 2 are examined, where the printer hotend is rastered in the XY plane as the build platform moves in Z as the layers are built. Figure 5-8 illustrates how the composition of the filament as well as the print orientation influences the impact resistance of the printed part. For the pure PC, the impact resistance of the 3D-printed specimen is less than 60 J/ m irrespective of the part geometry, which is greatly inferior to the standard reported properties of this PC from injection molded parts (807 J/m).[229] This large decrease in the mechanical properties of 3D-printed parts in comparison to their injection molded analogues is commonly reported and is one of the grand challenges associated with additive manufacturing. For the pure Surlyn, the impact resistance of the 3D-printed part is much larger (300 J/m), but still less than the impact resistance for injection molded parts (362 J/m).[230] The structured filaments in general provide a significant enhancement in impact resistance. As shown in Figure 5-8A for the XY geometry, increasing the proportion of Surlyn within the structured filament leads to an increase in the impact resistance from 497 J/m with 25% Surlyn to a maximum of 742 J/m with 55% Surlyn. In this case, the core−shell material outperforms either of the individual components irrespective of the composition. This improvement in the impact properties with the core−shell structure is consistent with expectations based on the consensus view of the interfaces between layers being the limiting factor for the mechanical performance of 3D printed parts, [57] but this core-shell

concept has not been previously applied to address this limitation. The impact resistance of the PC@55% Surlyn exceeds the impact resistance of injection molded Surlyn, whereas it is within 10% of the injection molded PC.

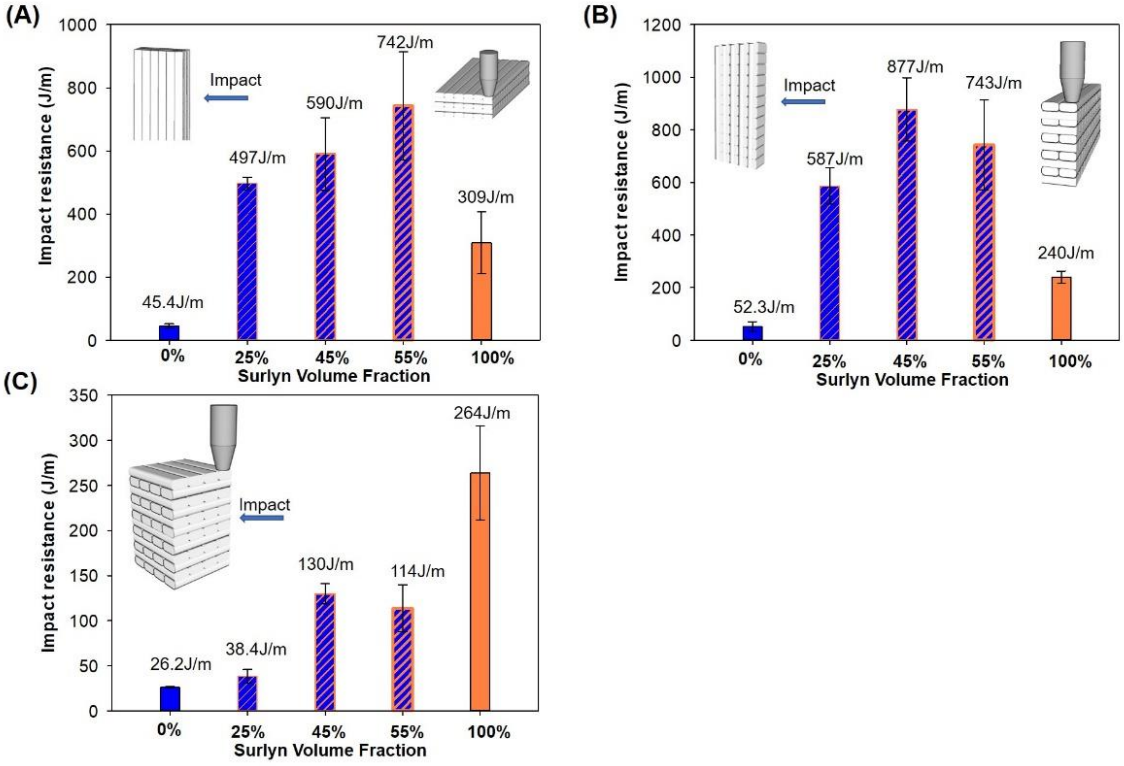

Figure 5-8 Impact resistance of 3D printed PC, PC@Surlyn, and Surlyn as determined from the Notched Izod test when the test specimen is printed in the (A) XY (flat); (B)XZ (edge-on); and (C) YZ (end-on) orientation. The specimen is notched after printing to ensure a pre-crack is formed

Figure 5-8B illustrates how changing the print geometry for the specimen to XZ affects the impact resistance. Interestingly, this geometry adversely affects the impact resistance for the pure Surlyn, but the impact resistance for PC@25% Surlyn and PC@45% Surlyn increases in comparison to that of the XY geometry. In this geometry, the specimen printed from PC@ 45% Surlyn

exhibits the greatest impact resistance (877 J/m). This impact resistance significantly exceeds that of any other previously reported 3D-printed polymer part and demonstrates the effectiveness of this core−shell approach to enhance the mechanical properties of parts printed by FFF. This impact resistance even exceeds that of the injection molded PC, which points to synergies in the impact properties through the use of the structured filament.

The weakest direction generally for FFF parts is in the YZ geometry,[51] and this is also true for the core−shell materials, as shown in Figure 5-8C. Unlike the other geometries, the impact resistance of the pure Surlyn exceeds that of the core−shell materials, but there remains a marked improvement for the PC@Surlyn in comparison to the pure PC. The orientation and filament composition dependence on impact properties are summarized in Table S1. To explain the orientation dependence, how the structures respond to impact must be understood.

5.3.3. Mechanisms for Energy Dissipation in 3D-Printed Objects.

Figure 5-9 illustrates the structure of the damage zone after impact for a specimen printed at the XY geometry with PC@45% Surlyn. The printed structure buckles through the sample is near the crack tip (Figure 5-9A), but the crack only propagates about 40% of the thickness of the specimen from a 2.67 kg impact event. This further demonstrates the efficacy of this core−shell design for enhancing the mechanical performance of 3D-printed parts. Nearest to the crack tip, the PC core material is stretched and bridges across the crack. This buckling at the crack tip can be better resolved by SEM, as shown in Figure 6-6B. Careful examination of the buckled fibers in the impact zone indicates that

they are thinner than the unbuckled regions at the edges. There is an abrupt change in the thickness in the impact zone, which we attribute to debonding and delamination of Surlyn from the PC core. As Surlyn and PC are immiscible, the adhesion between these two polymers is limited[231] and thus this interface appears to be the weakest link in the printed part, not the weld line interface between subsequently printed layers, which tends to fail.[147] To confirm the ease of delamination of Surlyn from the PC core, a 90° peel test of thermally welded PC/Surlyn films was performed (Figure 5- 10), which indicates that only a small force is required to delaminate PC and Surlyn. The failure of the Surlyn−PC interface on impact is consistent with our speculation that the high temperature to promote diffusion enabled by the core− shell filament and the specific functionality of Surlyn promote a strong interface for the 3D-printed parts. However, the delamination of Surlyn from PC will provide an additional energy dissipation mechanism for the 3D-printed part.

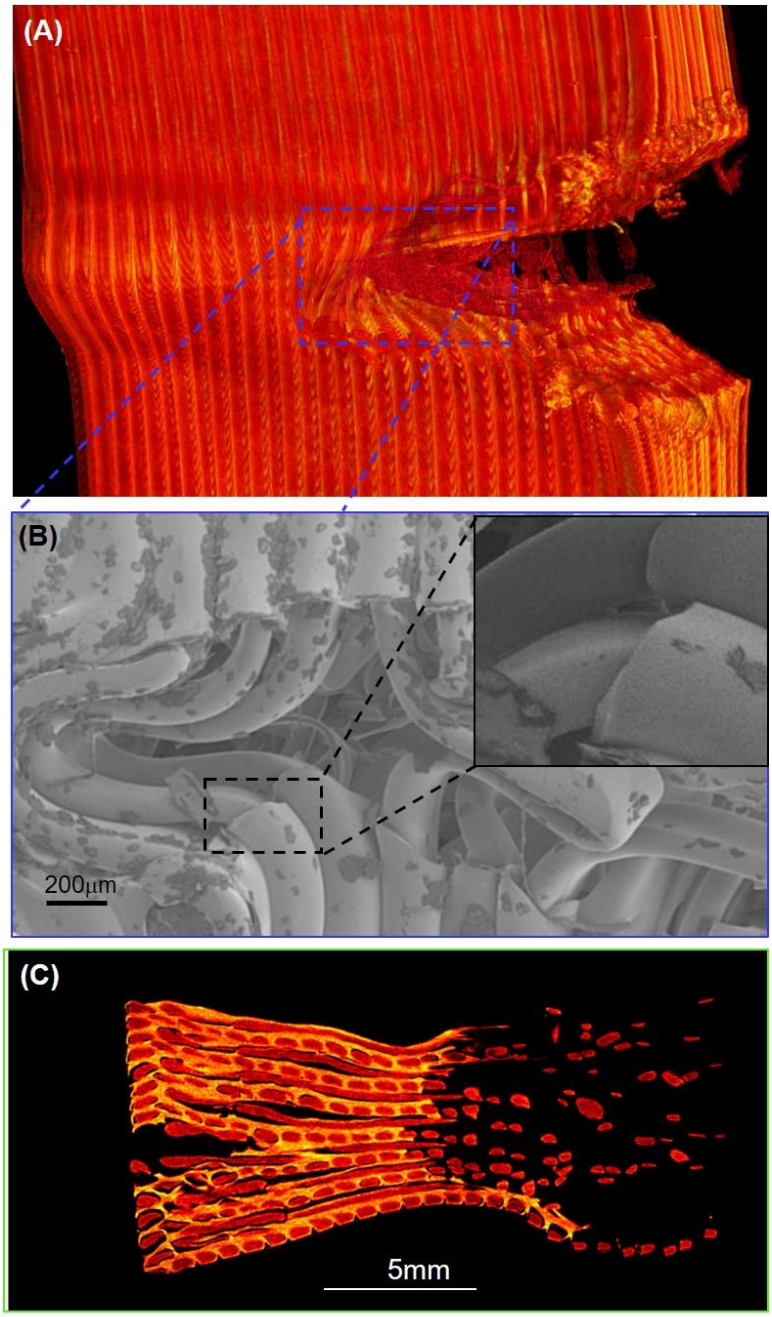

Figure 5-9 (A) X-ray μCT image of notched area after impact test for PC@45% Surlyn printed in XY orientation. (B) SEM micrograph illustrates the buckling of the PC fiber at the crack front (area in black dashed box); (C) X-ray μCT image of the cross-section of the specimen at the center of the notch illustrates the remaining PC fibers at the crack front, while the Surlyn has delaminated.

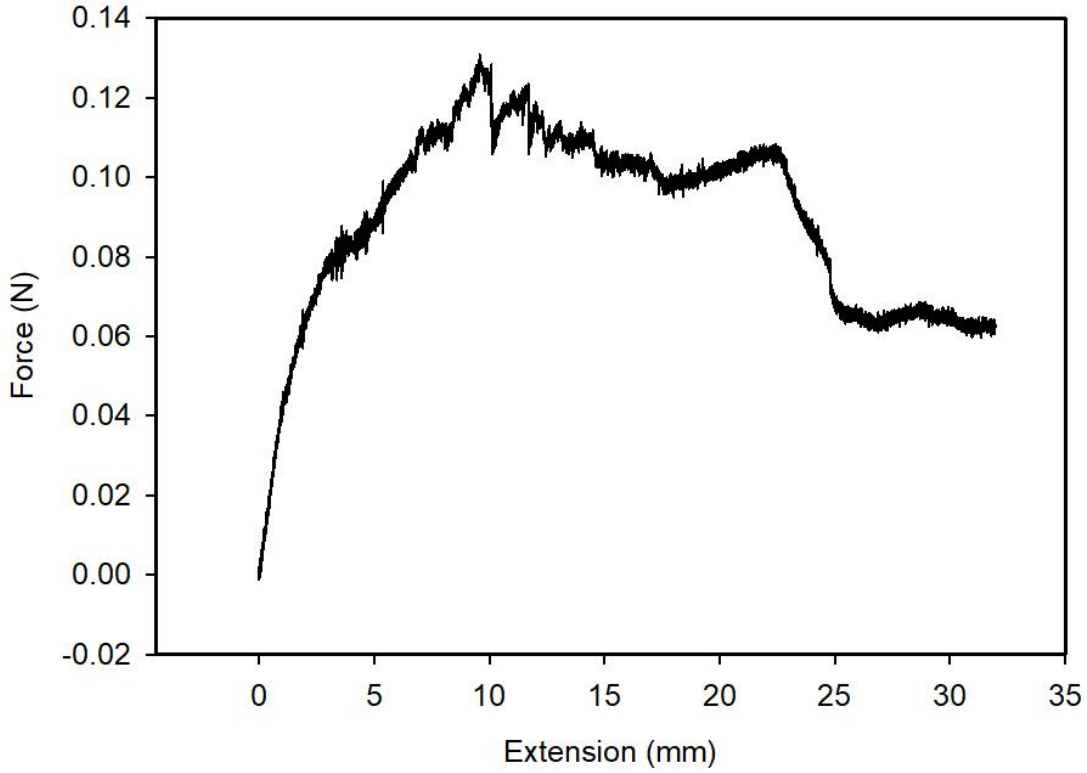

Figure 5- 10 Peeling test of PC/Surlyn films(10mm-wide) welded at 280°C for 10 seconds。

Additionally, the buckled structure near the crack tip provides evidence of plastic deformation of PC to further dissipate the energy of the impact. To confirm this delamination of Surlyn for the fibers bridging the crack, the plane of the crack is examined with X-ray μCT, as shown in Figure 5-9C. In the crack region, the isolated fibers are only darker orange, associated with PC, which is consistent with our expectation of delamination of Surlyn. This structure is distinct from the intact region of the specimen where there is a bright continuous phase (Surlyn) surrounding the isolated dark phase (PC). These failure structures are only present in the parts printed with the core−shell filaments, whereas the fracture surfaces from pure PC or Surlyn (Figure 5-11) are nearly

flat, which indicates the crack propagates through the sample along the direction of impact. These results demonstrate a likely change in the failure mechanism when parts are printed with the core−shell filaments.

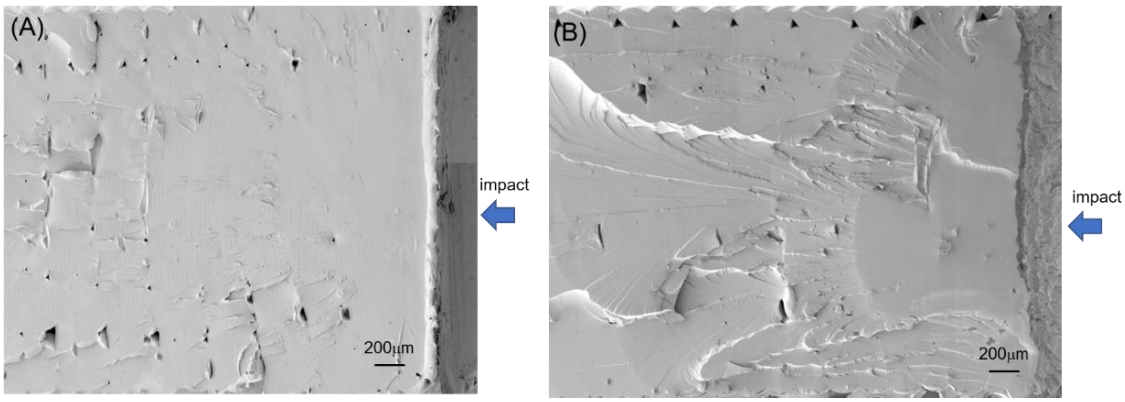

Figure 5-11 SEM micrograph of the impact fracture surfaces: (A) PC; (B) Surlyn。

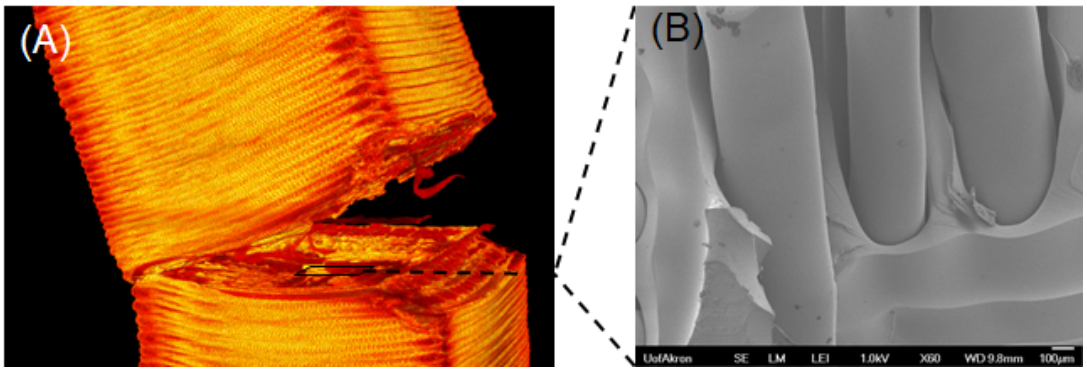

Figure 5-12 (A) X-ray μCT image of notched area after impact test for PC@45% Surlyn printed in YZ orientation. (B) SEM micrograph illustrates the core-shell debonding at the crack surface (area in black dashed box)。

From the careful examination of the deformation zone after impact, energy dissipation mechanisms have been identified that explain the geometry dependence of the impact resistance for the core−shell materials (Figure 5-8).

When the PC core fibers run perpendicular to the impact direction (Figure 5-8A,B), the delamination of Surlyn and the deformation of the PC fibers provide significant energy dissipation to toughen the printed structures. When the PC core is parallel to the impact direction (Figure 5-8C), there is no normal component for PC to deform to limit the crack propagation. Additionally, the PC− Surlyn interface is weaker than the weld lines, which provide a path for the crack to grow through the sample. Core−shell debonding can be observed at and near the crack tip (Figure 5-12). This difference in the strength of the interface is responsible for the lower impact resistance of the core−shell materials in comparison to pure Surlyn (Figure 5-8C).

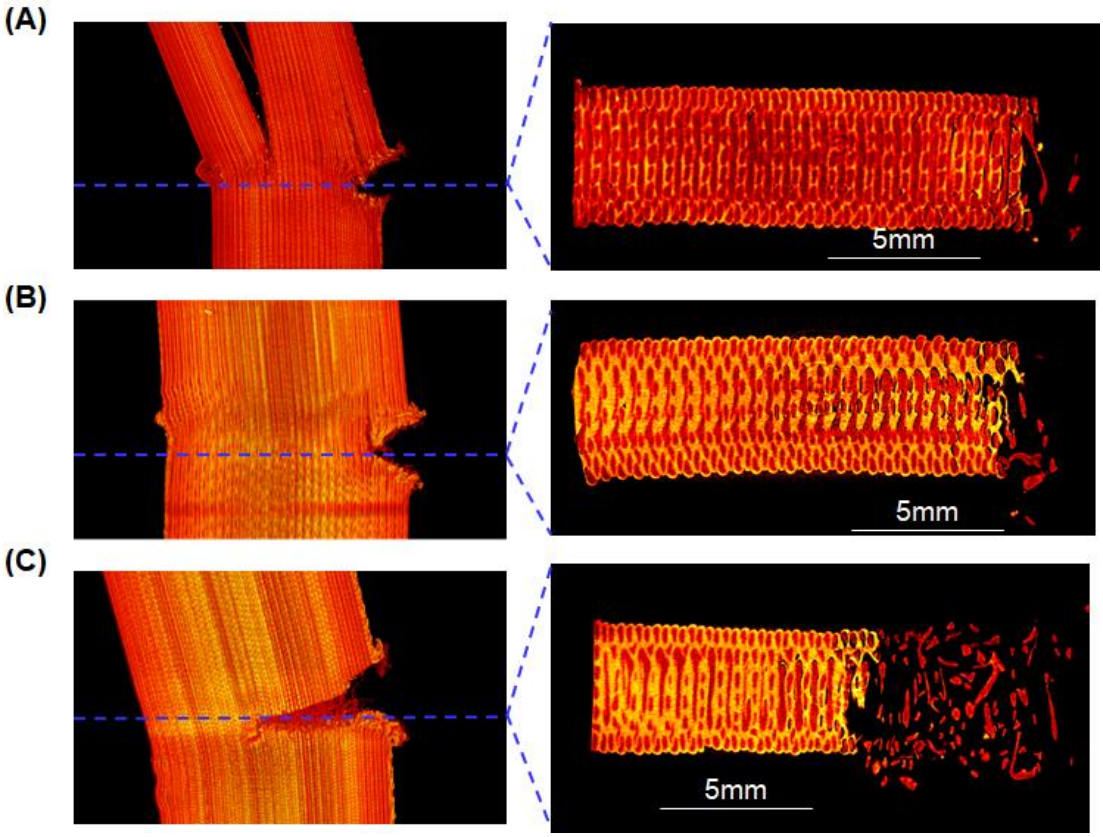

Figure 5-13 X-ray μCT images of the (left) side view and (right) cross section at the notch for 3D printed core-shell specimens with XZ orientation for (A) PC@25% Surlyn, (B) PC@45% Surlyn, and (C) PC@55% Surlyn.

Figure 5-13 illustrates how the composition of the core−shell filament influences the deformation of the 3D-printed specimen on impact as the thickness of the shell changes the observed impact resistance of the part. Figure 5-13A shows the structure of the damage zone for a specimen printed at the XZ geometry with PC@25% Surlyn. Instead of generating a crack propagating from the tip of notch (precrack), the impact event induces layer delamination of the core−shell perpendicular to the notch. This crack extends vertically through the sample, effectively breaking the upper part of the sample into two. This delamination is similar to a fiber laminate composite,[232] where impact damage is caused by the mismatch in stiffness. As PC is significantly stiffer than Surlyn, this composite-like behavior appears to be dominating when the shell (Surlyn) content is small. Conversely using PC@45% Surlyn (Figure 5-13B), neither a crack along the notch nor fully delaminated layers after the impact occurs, which illustrates the improved resilience of this composition. However, core−shell debonding is still observed in the cross-section, which indicates partial delamination as an energy dissipation mechanism. Further increasing the Surlyn content (PC@55% Surlyn, Figure 5-13C) leads to finite crack propagation along the notch direction after impact. In the damage zone, clean PC fibers free of Surlyn bridge across the crack. The different impacted zone structures suggest that the Surlyn−PC ratio is crucial for the enhancement of impact properties. At low PC content, matrix crack propagation is not fully

inhibited by the structured filaments (Figure 5-13C), whereas at low Surlyn content, the printed part is susceptible to deflection from impact (Figure 5-13A). A PC@45% Surlyn specimen absorbs the highest energy (Figure 5-8B) with the lowest deflection, which leads to synergistic impact properties in this PC−Surlyn composition. Figure 5-14 schematically illustrates these mechanisms for impact resistance with the core−shell filaments. This structured filament concept could be applied to other materials to generate 3D-printed objects with enhanced properties.

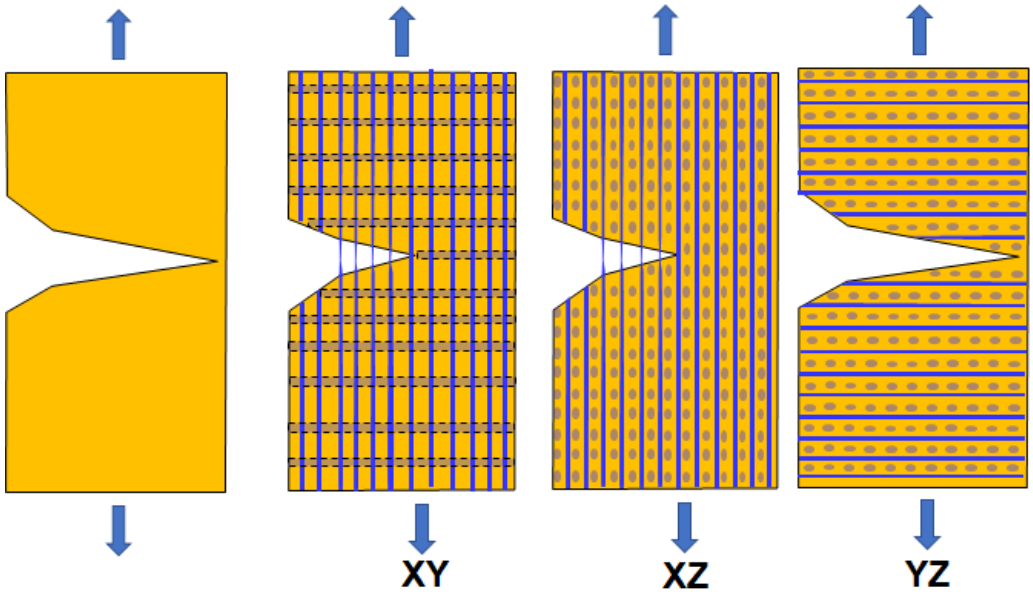

Figure 5-14 Schematic illustrating the inhibition of crack formation by PC-core reinforcement

5.3.4. Tensile Properties of 3D-Printed Objects

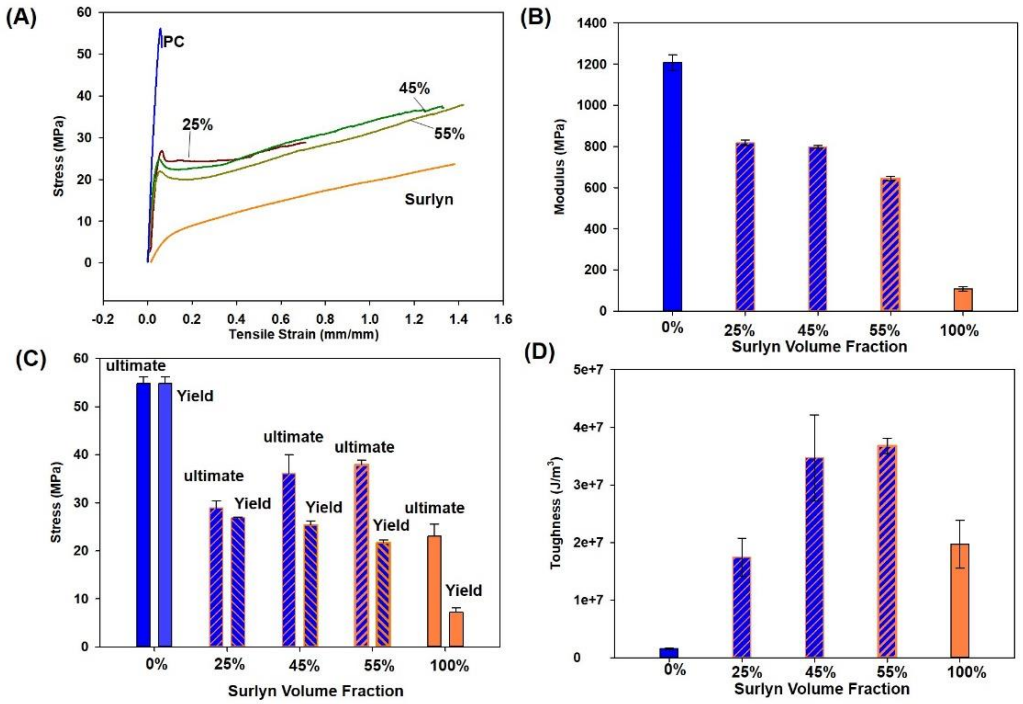

Figure 5-15 Tensile properties for 3D-printed PC, PC@Surlyn, and Surlyn. (A) Stress−strain curves of 3D-printed parts for three different compositions of PC@Surlyn in comparison to those of the pure components from which the (B) elastic modulus, (C) yield and ultimate tensile stress, and (D) toughness are determined. The ASTM tensile bar in this case is printed with the XY orientation.

More commonly, the tensile properties of 3D-printed parts are reported as Young's modulus is less sensitive to a small density of defects11,23 and optimization around modulus is common.[233] As such, the tensile properties of the parts printed with core− shell filaments are also examined. Figure 5-15A shows the stress− strain curves for 3D-printed samples printed from different filaments. On uniaxial stretching, the PC sample fails immediately after yielding

via a brittle fracture. This very limited elongation at break for the 3D-printed PC differs from the ductility of compression-molded tensile bars of analogous PC materials.[234235]Conversely, the part printed from Surlyn alone exhibits a low elastic modulus, but Surlyn can be elongated to more than double its initial dimensions. The stress−strain curve of 3D-printed Surlyn (Figure 5-15A) exhibits elastomer-like behavior, which is similar to the reported tensile properties of other compression-molded polyethylene ionomers.[236,237]However, the low modulus of the Surlyn part will lead to undesired deformation of the printed part at relatively low applied loads. The tensile performance of the parts printed from various compositions of PC@Surlyn filaments follows common features: (1) the initial modulus is modestly reduced in comparison to that of the pure PC, but significantly greater than that of the pure Surlyn, (2) yield point similar to the failure strain for the pure PC, and (3) stiffening post yield consistent with cold drawing. This combination of strain softening at yielding followed by a cold drawing in a strainhardening manner is often observed in the tensile test of compression-molded PC,[238] so the tensile behavior of the parts printed from the PC@Surlyn filaments appears to be more aligned with expectations of the mechanical performance of PC from traditional manufacturing (compression and injection molding) than the 3D-printed PC material. Figure 5-15B quantifies the differences in the elastic moduli for the 3D-printed parts from different composition filaments. The elastic modulus of Surlyn is approximately an order of magnitude less than that of PC, but there is only approximately 25% decrease in the elastic modulus for the two PC@Surlyn which are majority PC. This suggests that the tremendous increase in the

impact resistance with the core−shell filaments only modestly influences the elastic moduli of the printed parts.

Similarly, the tensile strength of the core−shell filaments is between that of PC and Surlyn (Figure 5-15C). The area under the tensile curve provides insight into the toughness of the printed parts as quantified by the energy absorption before fracture. This tensile toughness (Figure 5-15D) indicates improvements from the core−shell architecture, further confirming the synergistic improvement in toughness determined from impact properties (Figure 5-8). The relative improvement in toughness is less from the tensile test, which is attributed to the rate dependencies in the mechanical properties of PC and Surlyn. Table S2 summarizes the tensile properties of the 3D-printed parts.

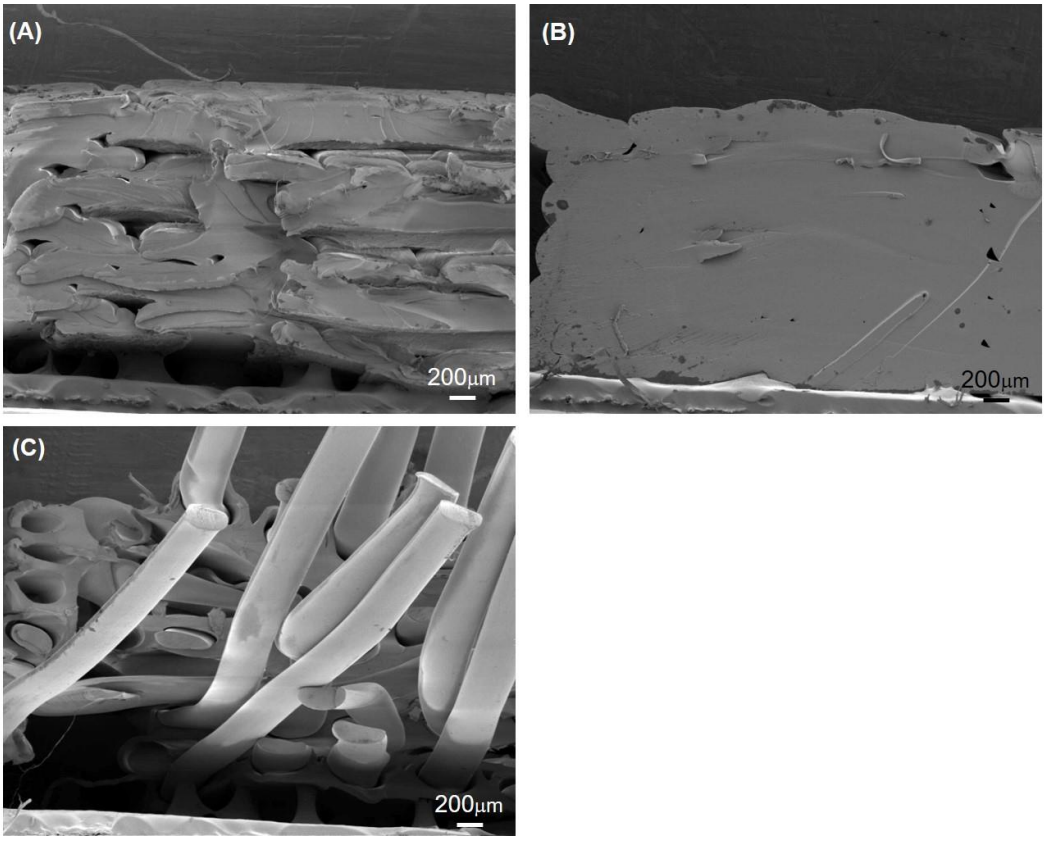

Figure 5-16 SEM micrographs illustrating the tensile fracture surfaces of 3D-printed parts from the filaments of (A) PC, (B) Surlyn, and (C) core−shell with 45% Surlyn. The fracture surfaces of parts from singlecomponent filaments are rather clean, whereas the PC@Surlyn filament leads to surfaces reminiscent of the fiber reinforced composites.

To understand the differences in tensile properties, the fracture surfaces are examined. Figure 5-16A illustrates voids at the fracture surface of PC samples, which indicates incomplete infill of PC samples. These voids provide defects in the tensile specimen that can promote failure. Additionally, the resolution of the cross-section of individual filaments is an indication of weak interfaces between the printed filaments, which provide pathways for catastrophic failure. The combination of voids and poor filament interfaces leads to brittle failure for the 3Dprinted PC, which is counter to the ductile behavior for PC processed by injection or compression molding.[234,239] The limited void concentration in the 3D-printed Suryln leads to smooth fracture surfaces (Figure 5-16B). The combination of excellent infill of the object and a well-diffused interface leads to the tensile behavior similar to the reported bulk properties for Surlyn.[236,237] The failure surface of the parts from the core−shell filaments appears to be consistent with fiber reinforced composites, where the PC fibers are elongated and delaminated from the Surlyn matrix at the fracture surface (Figure 5-16C). This indicates the ductile tensile behavior and provides insights into why the PC filament-reinforced Surlyn-based core−shell samples exhibit stress−strain curves similar to expectations for traditionally manufactured PC. This behavior suggests that filling of the voids in the 3D-

printed par and high-strength interfaces between the printed layers is most critical to achieving excellent mechanical properties from FFF parts.

5.4. Conclusion

In this work, a novel approach to overcome the poor mechanical properties associated with 3D-printed parts is demonstrated based on the use of structured filaments. A simple core−shell filament used in 3D printing via FFF is shown to enable synergistic impact performance enhancement through the generation of new pathways for energy dissipation and composite-like reinforcement. The printing orientation and composition of the core−shell filament are both important factors in determining the available mechanisms for energy dissipation in 3D-printed PC@Surlyn objects. Individually, printing with either PC or Surlyn leads to high susceptibility for crack propagation, which leads to catastrophic failure on impact. The use of the core−shell filament provides reinforcement from the continuous PC phase along the direction of the fiber; thus, the impacted specimen does not break when printed in XY and XZ orientations. Delamination of Surlyn from PC and stretching of PC fibers dissipate the energy from impact loading, which can provide unprecedented impact resistance for 3D-printed polymer parts exceeding 800 J/m. The tensile performance of the PC@Surlyn objects is similar to the expectations for traditionally processed (compression or injection molded) PC, although Young's modulus is decreased due to the lower modulus of the Surlyn matrix. The increased robustness of the 3D-printed parts will enable the use of core−shell filaments for high-performance applications where the brittle and failure prone nature of standard 3D-printed parts are unacceptable.

CHAPTER VI

TUNABLE PIEZORESISTIVITY FROM MAGNETICALLY ALIGNED NI(CORE)@AG(SHELL) PARTICLES IN AN ELASTOMER MATRIX

6.1. INTRODUCTION

Continuous roll-to-roll (R2R) processing has been actively explored for manufacture of a variety of emergent technologies, such as polymer photovoltaics[64], flexible electronics[65], smart packaging[66], and functional films[67,68], due to its potential for high production rates and low costs A typical R2R process involves unwinding a substrate material from a roll that is subsequently modified by coating,[240] deposition,[241] printing,[242] patterning,[243] or other functionalization of the unwound substrates in a continuous process. For functional devices, this typically involves multiple processes and steps where components are built in layers on the substrate, which necessitate registry and alignment.[244] Self-aligned imprint lithography provides one R2R compatible solution to overcome these registry challenges.[245] These lithographic methods are acceptable for high value products, but there opportunities for R2R production of functional films for commodity applications if the costs are sufficiently low. Self-assembly provide one potential avenue to low cost materials and has been demonstrated on flexible substrates.[246] However, these structures when anisotropic tend to orient in the plane of the substrate, which commonly is counter to the desired orientation. [247]

Controlling orientation in self-assembled structures has explored extensively in terms of directed self-assembly for nanofabrication in microelectronics.[248,249] One low cost route for desired self-assembled nanostructures is through field assisted alignment of block copolymers using electric,[250] magnetic, [251] or thermal[75]fields. In addition to providing orientation to self-assembled materials, the application of external fields can be used to generate structures in polymer blends[252] and polymer nanocomposites.[253] For example, the magnetic alignment of carbon nanotube containing polymer composites significantly enhance their thermal and electrical properties.[254] The alignment of iron particles in an elastomeric matrix provides tunable elastic properties for the composite.[255] External fields, such as electric and magnetic, provide opportunities to manipulate properties without changing the composition.[75] Functionalized magnetic particles at oil/water interfaces can be directed into 2-D assemblies in the presence external magnetic field.[256] By polymerized the oil phase, the directed assembled particles can be locked in place through “fossilized liquid assembly” to directly demonstrate how these particles respond to the magnetic field.[256]

The fabrication of these types of field directed materials can be scalable with recent advances with roll-to-roll (R2R) tools that are equipped with electric and magnetic field stations to provide continuous production of aligned materials.[257] For R2R processes, the materials are typically cast onto substrates; the casting process tends to orient anisotropic particles parallel to the substrate, but subsequent application of fields can provide “Z” orientation.[71] For example, dielectric particles are polarized in an applied electric field to align

themselves into chain-structures through their dipole-dipole interactions. This has been demonstrated with “Z” direction alignment of $BaTiO_3$ particles[72] in a continuous R2R process. For highly anisotropic particles such as graphite[71] or clay,[70] the application of an external electric field can preferentially align the long axis through the thickness of the film, “Z” orientation. An external magnetic field can also provide “Z” direction alignment of magnetically responsive particles, such as Ni.[74] The alignment of electrically conductive particles can lead to conductivity through the thickness of the film at concentrations well below the random percolation threshold due to the organization of the particles by the field.[74] For glassy polymers, this alignment leads to a permanently conductive material.

However, there are many cases where elastomers are desired to enable greater deformation of the functional material, such as desired for stretchable electronics.[258] When considering filled elastomers, the properties are not necessarily fixed due to the ability of the network to deform, which can lead to re-arrangement of the filler material. For example, elastomeric polymers filled with anisotropic conductive fillers can exhibit piezo-resistivity based on the deformation of elastic matrix inducing or breaking the percolated network of conductive fillers.[240,259,260] One of the most common matrices is polydimethylsiloxane (PDMS), which has been loaded with gold nanowires[240], silver nanowires[259] or carbon nanotubes[260] to generate piezoresistive elastomers. These materials have been demonstrated as structural health monitors[261] and wearable strain sensors[262]. However, one of the drawbacks of these approaches is the high cost and limited commercial availability of the

metal nanowires, while the purity, length distribution, and chirality of the carbon nanotubes[263] are important considerations for obtaining repeatable performance. These limitations are particularly problematic for cost sensitive applications of piezoresistive composites.

In this work, we present a scalable R2R process to fabricate elastomeric films with tunable piezo-resistivity through the use of magnetic fields to align nickel (core)-silver (shell) particles (Ni@Ag) in a PDMS matrix. The Ni@Ag particles are commercial, low cost filler materials that were developed to decrease the cost of Ag fillers for conductive adhesives for photovoltaic applications. The application of the external magnetic field leads to alignment of the particles into long chain structures that are orientated with long axis along "Z" direction of the film. These chains of Ni@Ag particles are in loose contact with the connectivity increasing as the loading of Ni@Ag in the PDMS increases. This structure results in electrical conductivity through the thickness of the film when a threshold pressure is applied. This threshold pressure for electrical conductivity is strongly dependent on the Ni@Ag particle content, which modulates the threshold from 0 kPa to 70 kPa as the Ni@Ag loading decreases from 3.6vol% to 0.25 vol%. The ability to use commercially available, low cost materials to generate tunable pressure sensors through a simple scalable R2R fabrication approach could be enabling for a range of applications for stretchable, flexible, and wearable electronics.

6.2. EXPERIMENTAL SECTION

6.2.1. Materials.

Sylgard 184 Silicone Elastomer was purchased from Dow Corning Corporation. Silver coated nickel (Ni@Ag) particles containing 15 wt% Ag were purchased from Novamet Specialty Products Corp USA. The average particle size was 49 ± 12 μm (see Figure 6-1). The substrate for the R2R line was thermally stabilized poly(ethylene terephthalate) (PET) (125 μm thick, Terphane, Inc.).

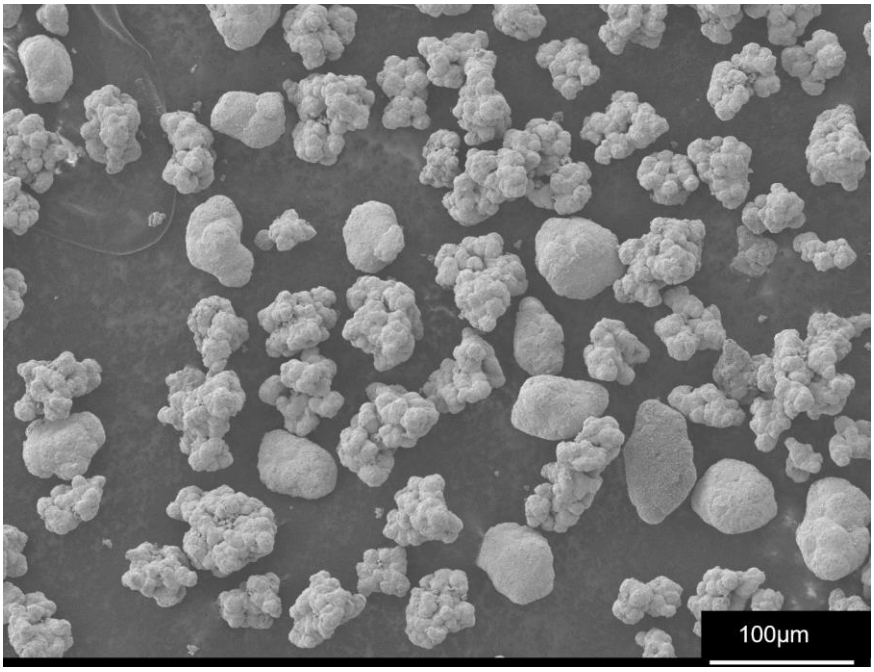

Figure 6-1 SEM micrographs illustrating the size of the Ni@Ag particles. The average particle size was determined to be 49 ± 12 μm from examination of 65 particles.

6.2.2. Particle alignment and film fabrication.

Sylgard 184 Silicone Elastomer base and curing agent was mixed at a ratio of 10:1 by a planetary vacuum mixer (Thinky ARV-310) at 1500 rpm for 5 min.

The PDMS pre-cursor was then pre-cured at 50°C in an oven for 22 min and then mixed with the Ni@Ag particles at the desired volume fraction (0.25 % to 5.3 %) using the planetary vacuum mixer at 1500 rpm under vacuum for 5 min. This composite mixture was then cast within 1 min to avoid significant variation in the cure state of the PDMS during the alignment. Two different processing procedures were used to generate samples with flat and textured topography.

For fabricating flat samples, the PDMS / Ni@Ag mixture was cast into a 1 mm deep glass mold and covered with a Mylar sheet on the roll-to-roll processing line[25] as shown in Figure 6-4. A pair of electromagnets applied a uniform magnetic field to the PDMS/Ni@Ag mixture along its thickness direction to produce “Z” alignment of the particles as shown in Figure 6-2A. Within the magnetic field (typically 52 mT unless otherwise noted), the PDMS/Ni@Ag mixture was heat cured by hot air (70 °C) for 60 min. To demonstrate that the alignment did not require an expensive electromagnet, an analogous alignment process was investigated where the same Mylar capped PDMS/Ni@Ag mixture was aligned between a pair of 3”×1” ×1/4" neodymium magnets (Amazon) during heat-curing in an oven at 90°C for 60 min.

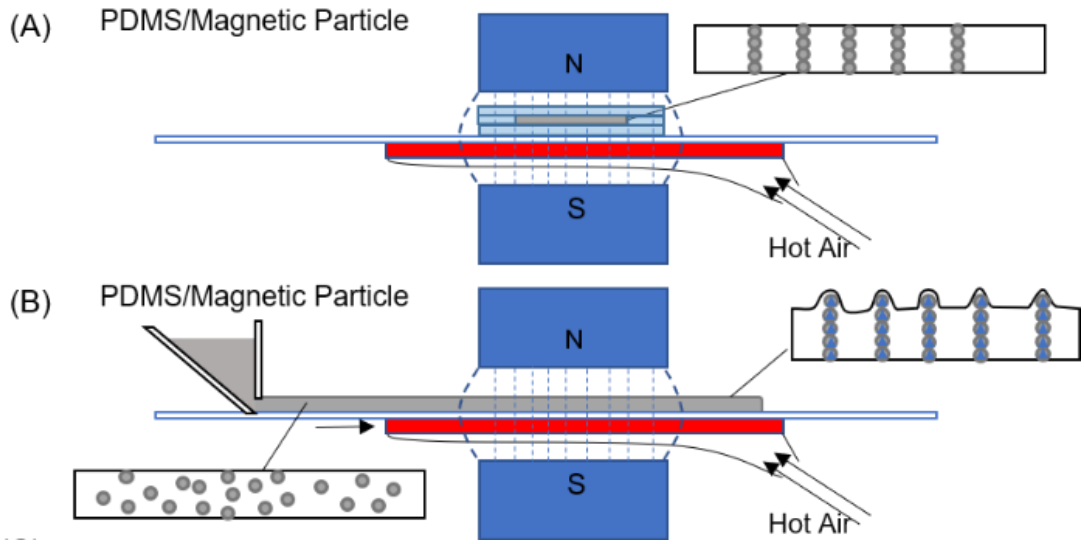

Figure 6-2 Schematic illustration of the two processes used to generate magnetically aligned Ni@Ag in PDMS: (A) molded materials cast within a glass mold and covered with Mylar to generate flat samples and (B) unconstrained roll-to-roll alignment of PDMS/ Ni@Ag where the material is produced in a continuous manner.

This processing results in a well-defined morphology for the composite, but this processing route with a mold does not lead to a readily manufacturable material. Aligned films of Ni@Ag in PDMS were also fabricated in a continuous process on the R2R machine using the electromagnet.[264] The PDMS/Ni@Ag mixture (prepared as described previously) was cast using a doctor blade with 1 mm gap onto the moving PET substrate (4 cm/min). The mixture was simultaneously aligned in the electromagnets with a magnetic field of 52 mT and heat-cured with hot air (140 °C) as shown pictorially in Figure 6-2B. The cured composite was removed by simply peeling from the PET substrate to generate free standing films approximately 1 mm thick.

6.2.3. Characterization.

The structure of the particle assembly within the composite films was assessed using an X-ray MicroCT scanner (Bruker Skyscan1172) operating at 50 kV and 200 μA. The large difference in electron density between the PDMS and the Ni@Ag particles enabled well resolved 3D structures from X-Ray tomography to provide the distribution of the Ni@Ag particles within the film. Transmission X-ray images were recorded at 0.3° rotational steps over 360° of rotation. NRecon software was used to reconstruct the cross-section images, which were then imported into the Skyscan CT Analyzer (V1.1) software to construct the full 3D morphology.

The surface morphologies of the films were characterized by using an optical microscope (Olympus CX31) and field-emission scanning electron microscopy (FESEM, JEOL-7401). Before the SEM imaging, the top surface of the samples was sputter coated with silver for good surface electrical conductivity to prevent undesired charging. To better assess the alignment of particles through the full thickness, optical images were obtained of both the top and bottom of the PDMS/Ni@Ag films in transmission mode.

The simultaneous measurements of mechanical and electrical properties of the PDMS/Ni@ Ag were carried out using a customized tensile machine with a customized compression clamp that was reported in detail elsewhere previously.[73,74] These measurements were performed in compression using 8mm × 8mm × 1mm PDMS/Ni@Ag films placed between two aluminum electrodes and compressed at 1 mm/min (strain rate 100% S^{-1}). During

compression, the through-thickness resistance was measured using a Keithley 6487 Picoameter.

The piezoresistivity of PDMS/Ni@ Ag samples was tested on an Instron 5567 Tensiometer in a step-wise manner. As shown in Figure 6-2, two gold-coated glass slides were placed between two compression plates to act as electrodes. In order to lower the pressure change applied by each compression step, the gold-coated slide on the bottom is supported by two springs. In compression, the PDMS/Ni@Ag samples were placed between two gold-coated glass slides and both top and bottom surface of the samples are coated by a thin layer of Spectra 360 Electrode Gel to minimize effect of the contact resistance change during compression. In each test, pressure applied to the sample was increased step-by-step via lowering the upper electrode.

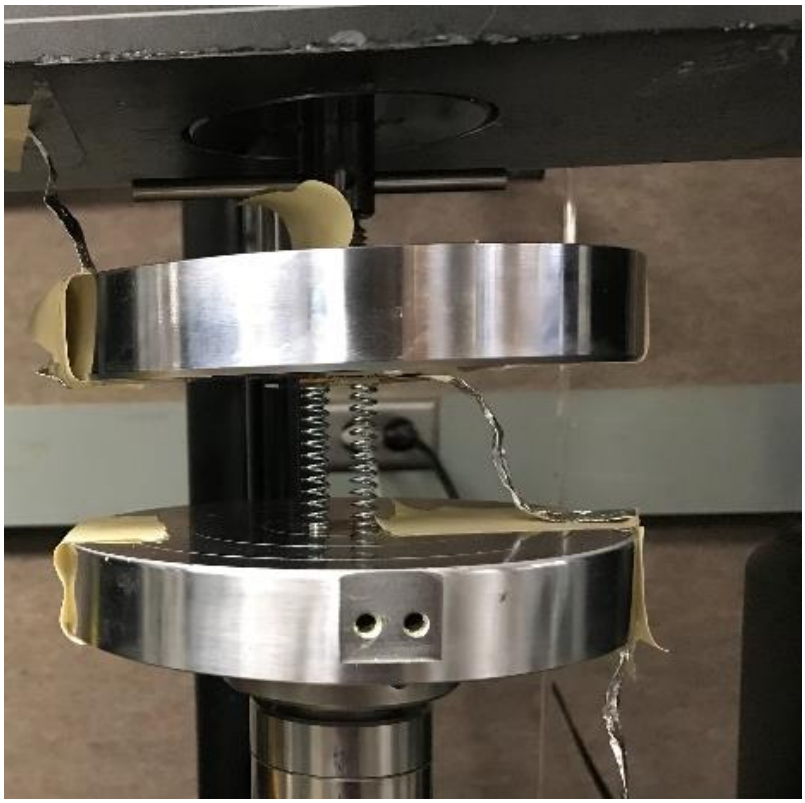

Figure 6-3 Picture of step-wise piezoresistivity measurement using an Instron 5567 compression fixture. The electrode leads are connected to gold coated slides that provide the electrodes between the PDMS/Ni@Ag composite.

6.3. RESULTS AND DISCUSSION

The application of the magnetic field during the curing process of the PDMS dramatically impacts the morphology of the composite as shown in Figure 6-6. From x-ray tomography, it is clear that the Ni@Ag particles sediment during the curing of the PDMS (Figure 6-5A) without any applied field. This leads to a surface that is devoid of any particles. This morphology leads to low electrical surface resistivity (0.262 in ohm/sq) on the bottom surface due to the formation of percolated network of Ni@Ag that have settled during curing. However, the resistivity through the thickness of the sample (> 10^{10} ohm·m) is very large due to the insulating characteristics of PDMS; a similar resistivity is found when considering the top surface of the specimen. With the application of a low strength magnetic field (52 mT) with the electromagnet (Figure 6-4), the morphology of the composite is drastically altered as shown in Figure 6-5C. In this case, the Ni@Ag are aligned into chains through the thickness of the film. This alignment leads to high surface resistivity on either side due to the isolation of the particles in the plane of the film, while the through-thickness resistivity is low due to the percolation of particles in the chains. Increasing the magnetic field strength to 225 mT leads to a limited change in the morphology or electrical properties of the composite (Figure 6-5E). The Ni@Ag particles can be well aligned using a permanent magnet as well as shown in Figure 6-5 (G),(H).

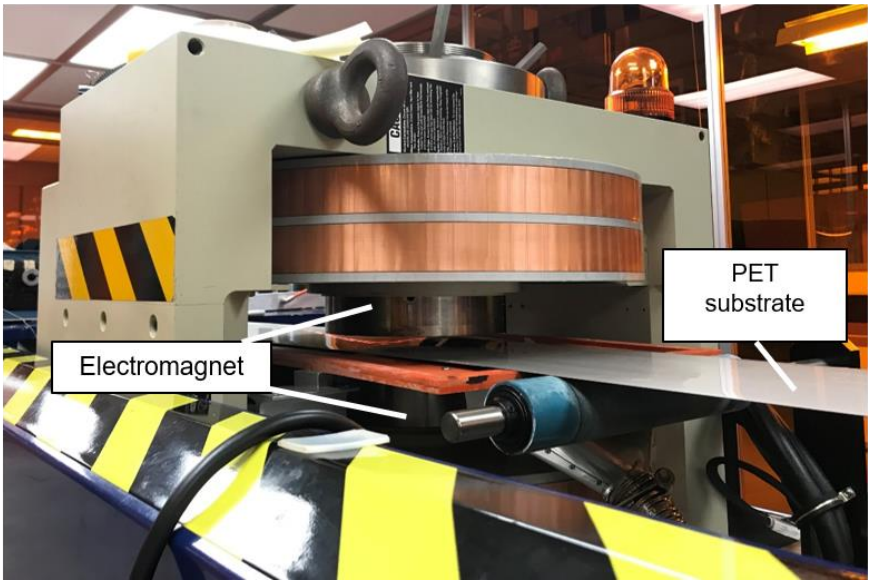

Figure 6-4 Picture of roll-to-roll machine that includes an electromagnet for “Z” alignment.

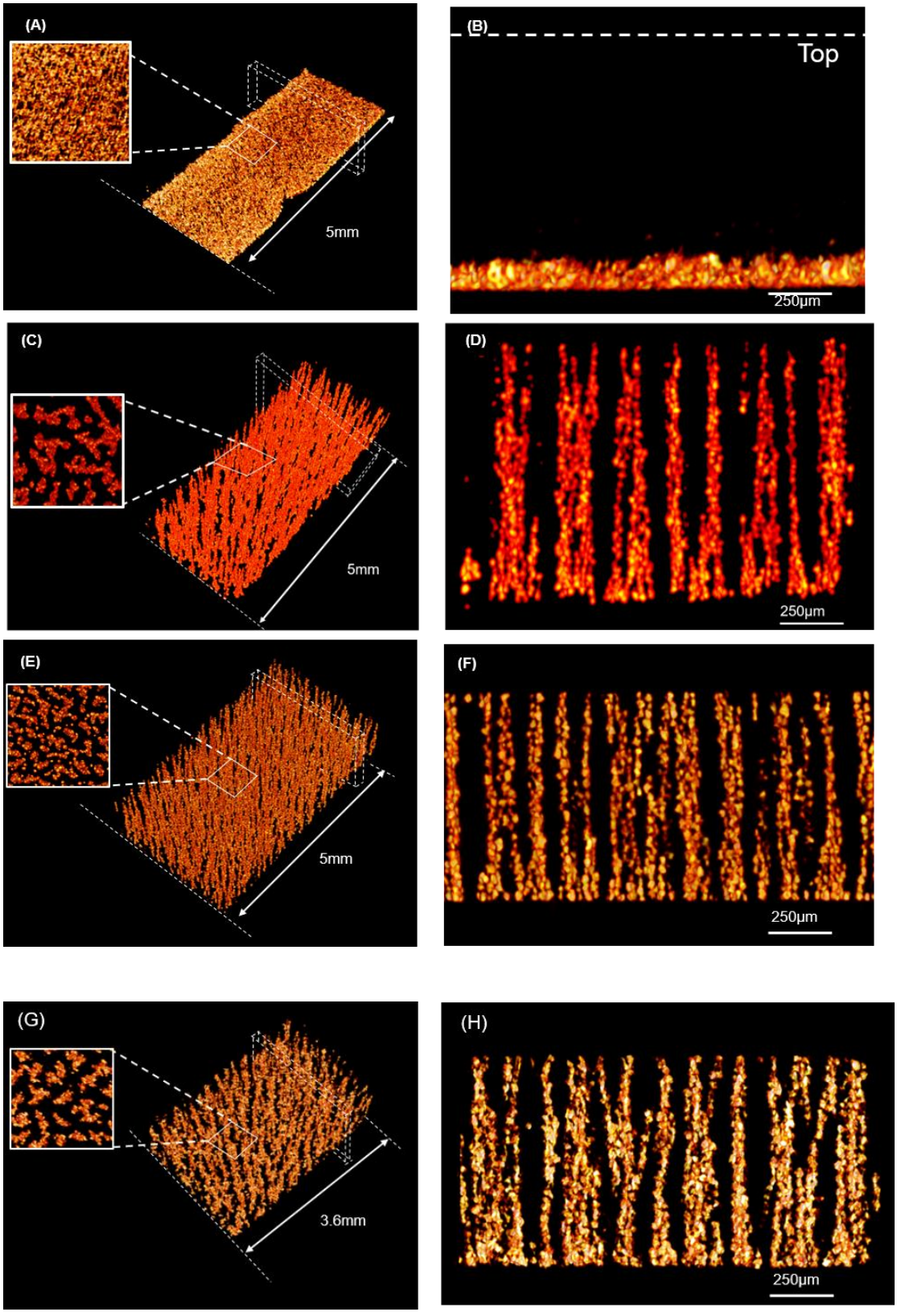

Figure 6-5 X-ray tomography images of composite films containing 3.6 vol % Ni@Ag particles in PDMS and cured at 70 °C for 1 h using (A) no magnetic field

with dashed line being a 0.3 mm cross-section slice shown in (B), (C) 52 mT field with the electromagnet with (D) 0.3 mm thick cross-section of this aligned sample, (E) 225 mT field with the electromagnet with (D) 0.3 mm thick cross-section of this aligned sample. The Ni@Ag particles can also be well aligned in the PDMS matrix using (G, H) a permanent magnet.

In order to better understand the electrical conductivity through the thickness of the aligned films, samples were prepared using different filler loadings but the same magnetic field strength (52 mT). As shown in Figure 6-6A, samples with different particle concentration all shows a resistivity lower than reported volume resistivity (2.9×10^{12} ohm·m) of Sylgard 184 PDMS,[265] due to the aligned Ni@Ag particle columns that percolate through the thickness direction. The resistivity of the aligned samples changes as applied pressure increases during the measurement. At low pressures, all samples show high resistivity (10^4 - 10^6 ohm·m) that decreases insignificantly with increasing pressure. Near a pressure threshold, the resistivity decreases drastically over a narrow pressure range with small increases in pressure. As the particle loading increases, the threshold pressure for this high to low conductivity transition decreases. Interestingly, all of the specimens examined are well below the random percolation threshold for spheres (≈28 vol%),[266,267] but exhibit good electrical conductivity at sufficient pressure. As the applied pressure increases from zero to 100kPa, all aligned PDMS/Ni@Ag composites exhibit a significant decrease in the resistivity, but the pressure at which the specimen transitions from high resistivity to low resistivity decreases as the particle concentration increases from 0.25 vol% to 3.6 vol%. This phenomenon

indicates that the effective pressure sensing range of piezo-resistivity can be effectively tuned by particle concentration for a fixed applied magnetic field. Figure 6-6B illustrates how the loading of Ni@Ag influences the required critical pressure for high-to-low resistivity transition. This critical pressure is determined to be the highest pressure at which the sample shows resistivity>10^4 ohm*m.

The relationship between the resistivity (ρ) of a polymer/conductive particle composite and applied pressure has been reported to follow:[186]

$$\rho(P)\Big/_{\rho(0)} = e^{-2\lambda\Delta d} = e^{-2P\lambda d/E} \qquad (1)$$

where $\rho(P)$ is the resistivity at applied pressure P, λ is the tunneling parameter when assuming identical tunneling junctions for all particles, d is the interparticle distance, and E is the modulus of the composite. PDMS filled with aligned conductive particles at loadings of ~ 15 % followed this scaling. [186] For the composites examined here, this resistivity-pressure relationship does not hold with a threshold stress required to observe an appreciable decrease in resistance. Magnetic field aligned PDMS/Ni particles composites with low particle concentration showed a similar threshold behavior,[73] but the minimum resistivity and required pressures were orders of magnitude greater than reported here with the origin of this critical pressure not reported.

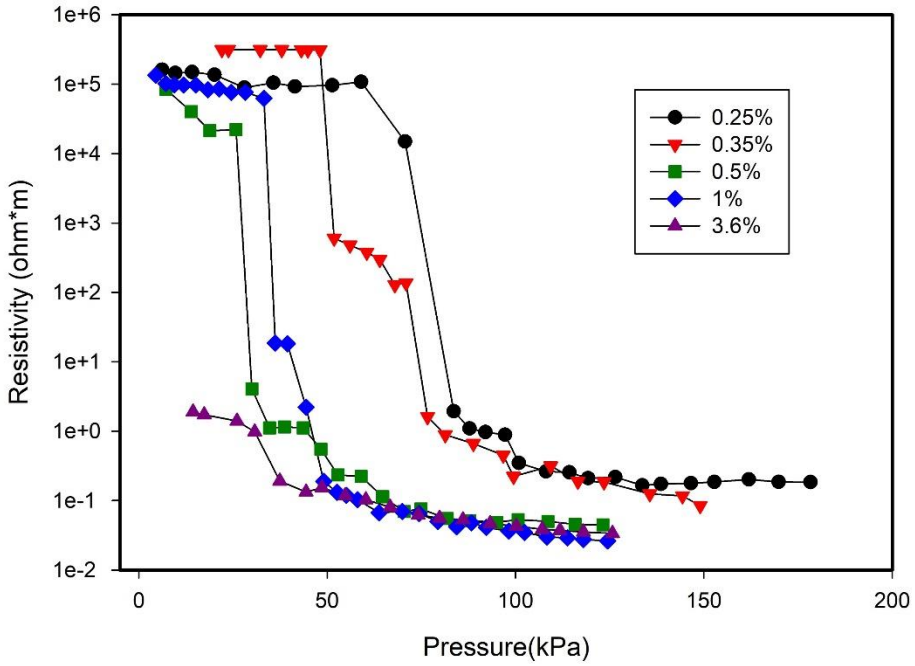

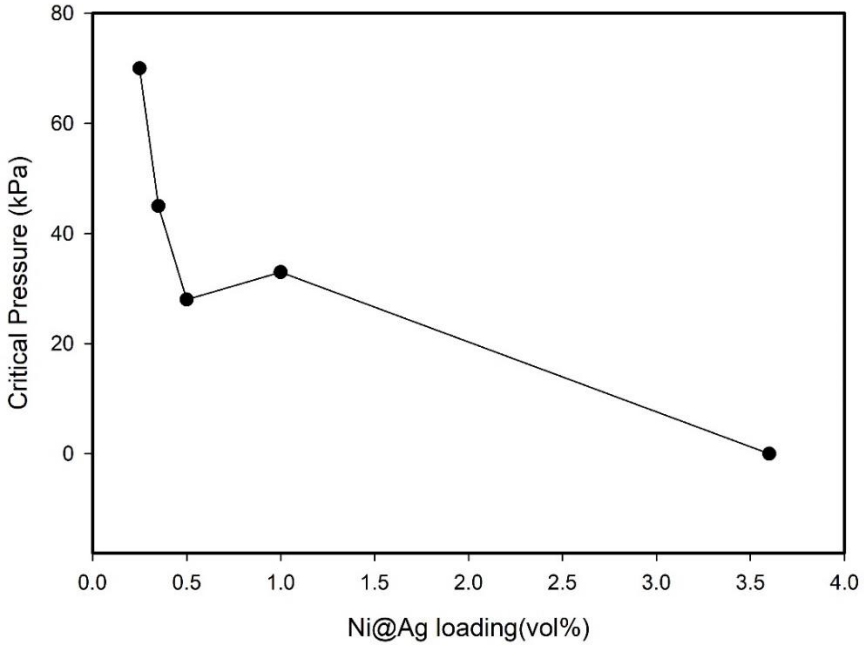

Figure 6-6 (A) Piezo-resistivity of aligned (flat) Ni@Ag composites as a function of the particle loading in the composite. (B) Threshold critical pressure associated with conductivity percolation of the aligned Ni@Ag composites.

To investigate the origins for the critical pressure in these Ni@Ag composites, the morphology of Ni@Ag particles was investigated using optical microscopy as shown in Figure 6-7. At all concentration, both the top and bottom surfaces show exposed particles (black regions with clear edges). However, at low concentration (0.25 - 1 vol%), significantly more particles are exposed at the bottom than at the top surface. In Figure 6-7A-C, the red circle shows particles that are buried in the matrix when observed from the top as the particles are out of focus. These buried particles suggest the formation of aligned particle columns that are too short to percolate through the thickness of the sample. At higher concentration (2-3.6 vol%), these buried particles less common at the top surface with larger particle aggregation clusters at the bottom than at the top surface. These optical images are consistent with better formed columns of Ni@Ag particles at higher loadings, which could explain the difference in piezoresistive behavior in the composites.

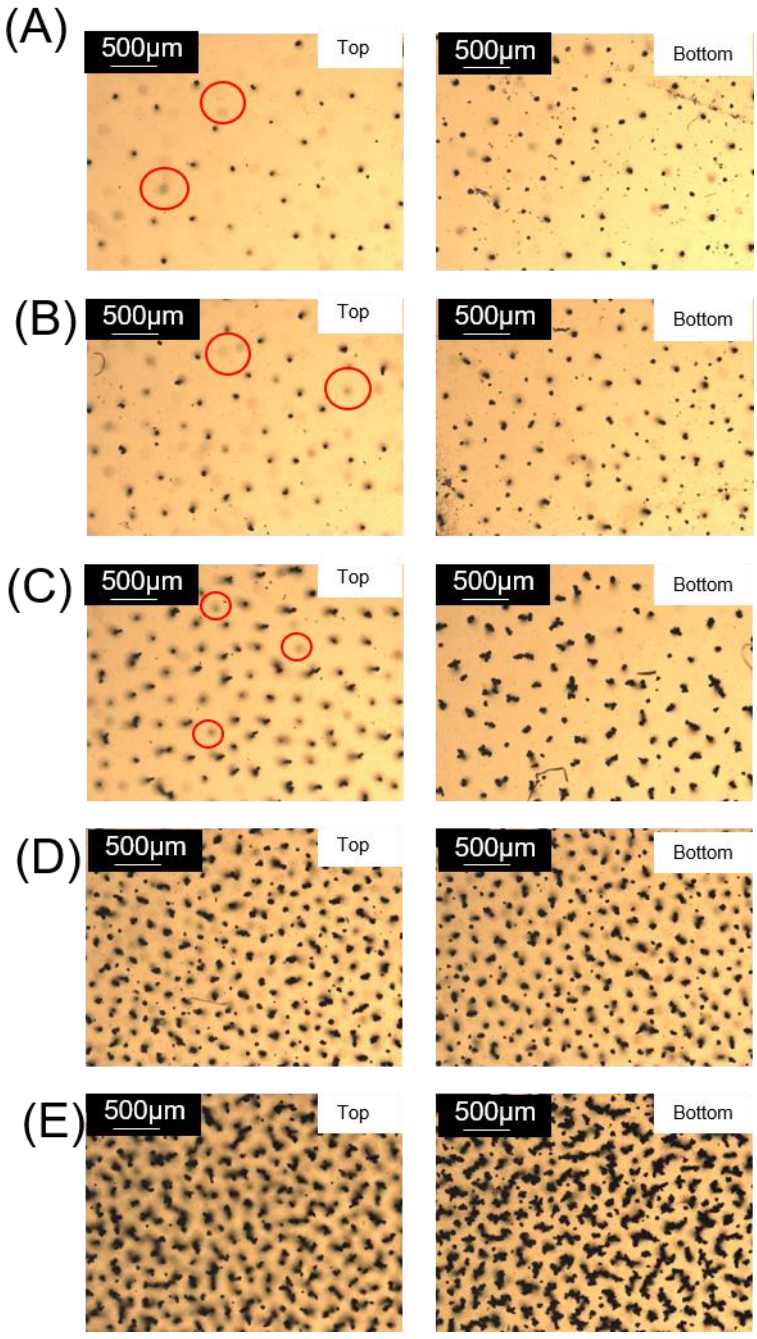

Figure 6-7 Optical micrographs of the top and bottom of the flat-PDMS/Ni@Ag films with different Ni@Ag loading: (A) 0.25 vol%, (B) 0.5 vol%, (C) 1 vol%, (D) 2 vol% and (E) 3.6 vol%. Select Ni@Ag particle columns that do not percolate through the thickness of the film are shown with the red circles. These particles are out of focus as they are imbedded within the PDMS and not at the surface.

The internal morphology was assessed with x-ray microCT for the 1% and 3.6% PDMS/Ni@Ag films. Figure 6-8A shows the distribution of Ni@Ag particles inside PDMS for the 1 vol% film. The magnetic field leads to aggregation of the Ni@Ag particles into small columns. In Figure 6-8A, most particle columns are composed of predominately a chain of single particles although some particle aggregation is observed at the bottom of the particle columns (Figure 6-8B). Increasing the concentration to 3.6 vol% of Ni@Ag (Figure 6-8C) leads to most particle columns being composed of aggregates of particles and some columns are connected to neighboring columns at the bottom (Figure 6-8D). The different morphology observed for the top and the bottom of PDMS/Ni@Ag films are likely from gravity driven sedimentation of Ni@Ag particles in liquid PDMS precursor prior to curing of the PDMS. Some sedimentation occurs prior to magnetic field application leading to higher concentration of Ni@Ag particles near the bottom than near the top surface. In the magnetic field, the Ni cores of Ni@Ag particles are magnetized and gain a magnetic dipole. The dipole-dipole interaction between neighboring particles leads to formation of chain-like structures. At higher concentration, each particle chain is closer to neighboring particle chains upon formation, therefore are more likely to be attracted by neighboring particle chains to form particle aggregates in the column.

Another important morphology difference between these two films are the gaps between adjacent Ni@Ag particles. As shown in Figure 6-8B, at 1 vol% Ni@Ag, gap between adjacent particles can be clearly observed in each aligned particle column. Meanwhile, Figure 6-8D suggests that at 3.6%, particles are

more densely packed in each particle columns and only little gaps are observed in each column at the resolution of the x-ray microCT (approximately 2.5 μm). These gaps in particle columns are discontinuities in the electrically conductive network, which would result in increased through-thickness resistivity due to requirement of electron tunneling through the insulating PDMS. During compression of the film, these gaps can be closed to form new conductive paths through the thickness. Below the critical pressure, a significant number of gaps still exist in each column. At the critical pressure, some gaps are closed due to dimension change in thickness direction. Therefore, new conductive paths are formed and the resistivity decreases drastically. The pressure range over which the rapid decrease in resistivity occurs is likely related to the distribution of gap sizes. This mechanism based on closing gaps between particles is different than that described by eqn(1) as in this case the decrease of resistivity relies on the closing of large interparticle gap that are randomly along the chain of aligned particles instead of the uniform decrease of interparticle distance. As there are more and wider interparticle gaps with only 1 vol% Ni@Ag, larger compression strain and hence higher compression pressure is required to close these gaps. This mechanism explains the presence of the a critical pressure for high conductivity and its concentration dependence based on the microCT images in Figure 6-8.

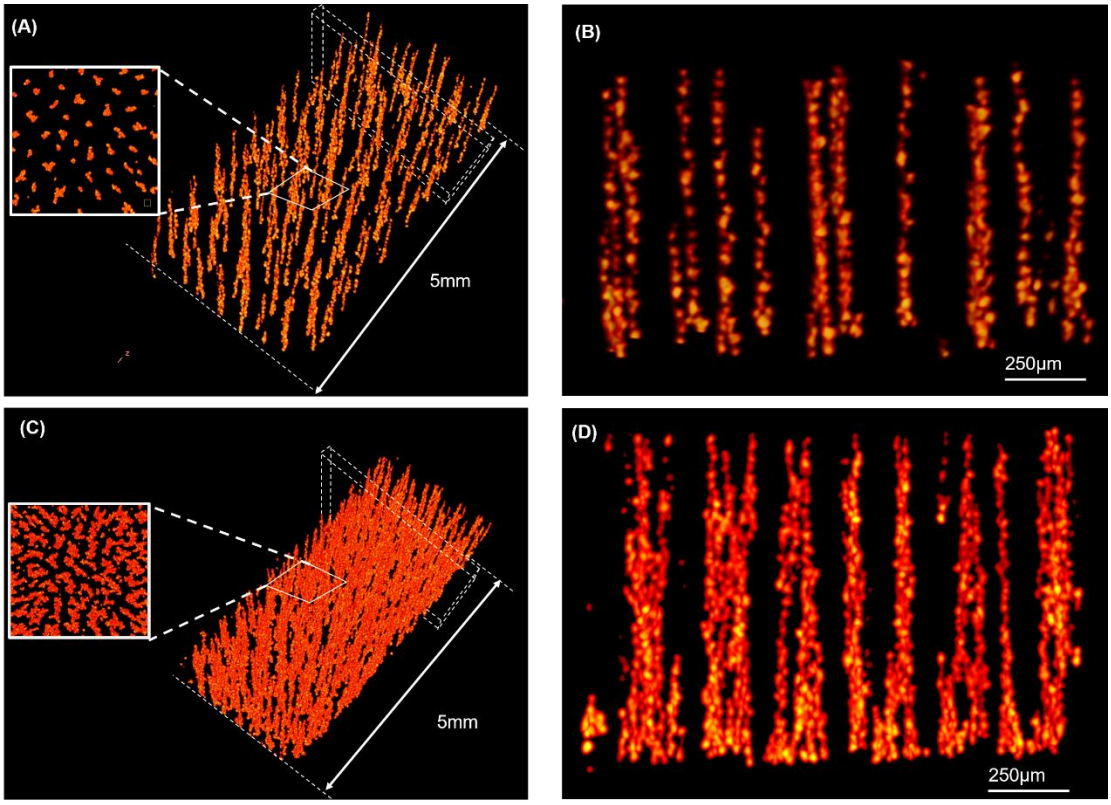

Figure 6-8 MicroCT images of flat-PDMS/Ni@Ag film containing 1 vol% of Ni@Ag for (A) full 3D representation with surface projection shown in the inset and (B) a 0.3 mm-thick section as noted by the dashed box. The chains of Ni@Ag tend to bundle when the concentration is increased to 3.6 vol% as shown for (C) the full 3D representation and (D) a cross-section that better illustrates the bundling.

Figure 6-9 shows the reversibility of the piezoresistivity of the 1 vol % Ni@Ag /PDMS composite over cyclic loading and unloading. During the first cycle, the resistivity of the sample decreases during compression then increases back to high resistivity when the applied pressure is released. However, there is a large hysteresis in the resistivity loop with the critical pressure decreasing by nearly half during unloading. During the 2nd loading cycle, the resistivity drops at >23kPa, which is much lower the original pressure

required on loading, but greater than the pressure during the initial unloading. During pressure released of the 2nd cycle, the resistivity increases back to its initial high value at even lower pressures. This hysteresis in the pressure dependencies of the resistivity suggests that there is a change in the connectivity between particles upon compression that does not fully recover. This could be a result of the low melting point for Ag where the ohmic heating[268] of the Ni@Ag could weakly weld particles to maintain the connections. For the third cycle, the hysteresis loop is reduced with the plateau high resistivity achieved at the same pressure. Additional cycling leads to very similar piezoresistive to the unloading of the 3rd cycle. In these cases as the applied pressure increases above 13 kPa, the resistivity drops drastically. For device applications, this prior history dependence of the piezoresistive behavior is generally undesired, but there are instances where this history dependence could be beneficial. This dependence on prior loading history could be a simple anti-tampering component[44] or determine if a device was subjected to undesired pressures. However as the piezoresistive behavior appears to reach a quasiequilibrium state after 3 loading-unloading cycles, this could be considered a ‘burn-in’ period that acts to increase the pressure sensitivity of the material.

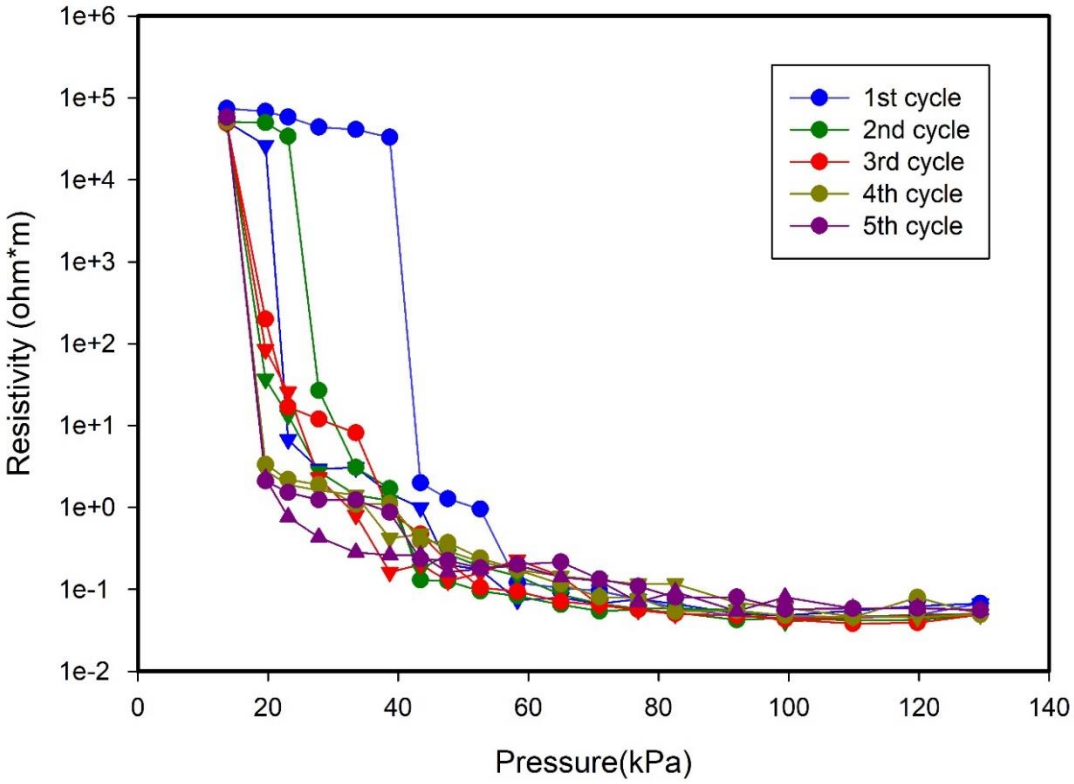

Figure 6-9 sistivity of flat PDMS/Ni@Ag film containing 1vol% Ni@Ag particles during loading (compression) (●) and unloading (▼) cycles

In the cases presented, the composite is covered during the magnetic field application and curing, without this cover the Ni@Ag particles can generate surface features during the magnetic field assisted alignment as shown in Figure 6-10. With 1 vol% Ni@Ag, the film surface is nearly flat, like the previously reported materials. However at higher concentration (3.6 vol%-10.2 vol%), large spiky features appear on the surface of the films. Further increasing the concentration of Ni@Ag to 18 vol % leads to a significant reduction in these surface features with only tiny spikes at the surface. As the loading of Ni@Ag increases, the transparency of the composite decreases. With 1 vol % Ni@Ag, there is only a slight decrease in the light transmission. At

5.3 vol% Ni@Ag, the grid lines can still be observed behind the sample, but at 10.2 vol% the sample becomes fully opaque.

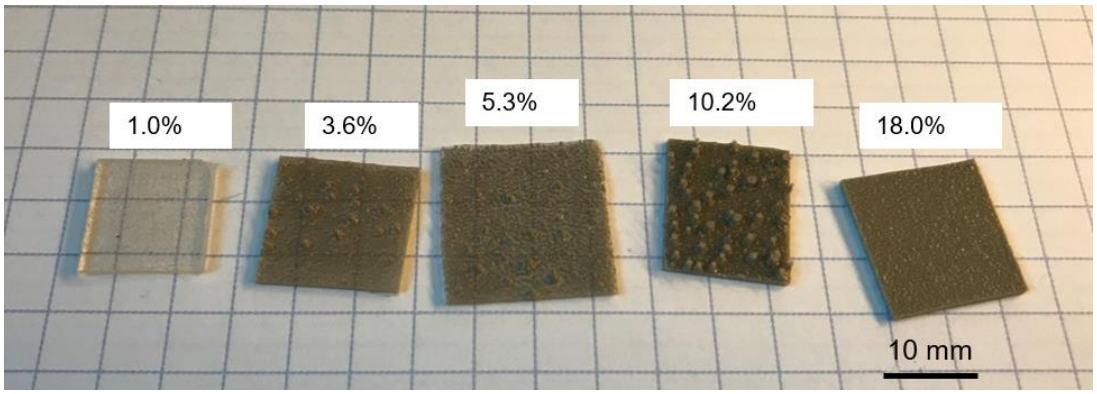

Figure 6-10 Photographs of aligned PDMS/Ni@Ag films with different Ni@Ag volume fractions produced by continuous roll-to-roll fabrication.

Figure 6-11A illustrates the spiky features in the surface of the 5.3 vol% Ni@Ag composite from a SEM cross-section. In this case, the spikes are approximately 0.5 mm wide and 1 mm high. These spikes are comprised predominately of Ni@Ag particles as determined by microCT (Figure 6-11B). Without the constraint of the cap layer at the surface of PDMS during alignment, the Ni@Ag particles can overcome the gravity and surface tension of PDMS to form spiky aggregaties that protrude from the surface of PDMS due to the force provided by the applied magnetic field. Such surface features could be enabling for reusable dry contact electrocardiography (ECG)/electroencephalograms (EEG) sensors.[45] These electrodes are fabricated with conductive materials, which are connected to an amplification circuit and in contact with skin during use, but dry electrodes often suffer from poor signal quality due to the contact impedance between electrodes and the Stratum Corneum. To improve the signal quality, surface features manufactured by molding,[46] micromachining[47]

or 3D-printing[48] act to reduce motion artifact and the contact through increasing the local pressure. The R2R manufacturing of aligned PDMS/Ni@Ag provides a potential scalable, low-cost alternative method for the fabrication of flexible dry-contact electrodes with low resistivity ($<10^{-1}$ ohm·m) at low applied pressures (< 60kPa). Moreover, the surface features can be easily tuned from nearly flat (1 vol%) to large and thick spikes (3.6vol% to 10.2vol%) or rough surface with tiny particle protrusions (18 vol%).

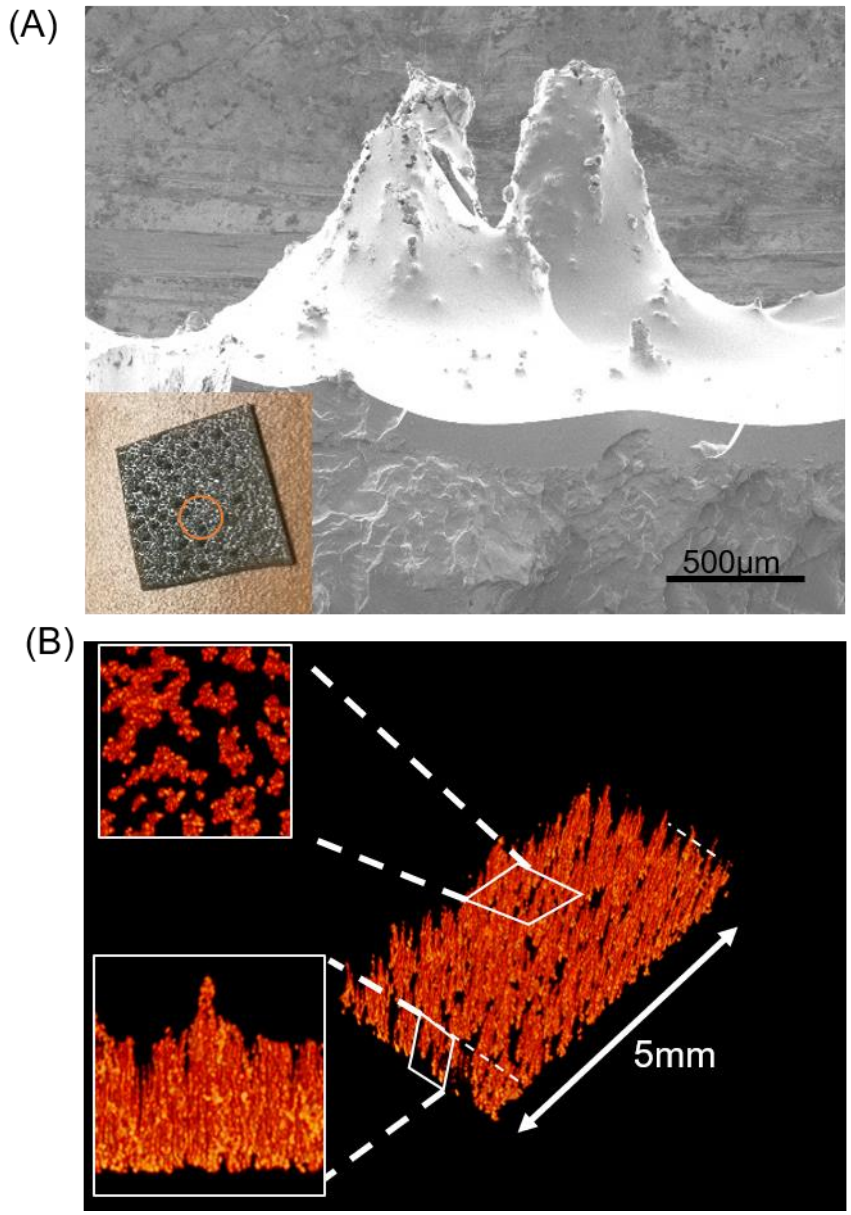

Figure 6-11 (A) SEM micrographs illustrate two spikes on the surface of a PDMS/Ni@Ag (5.3vol%) film. The inset shows a photograph of the sample to demonstrate the topographically rough surface. (B) MicroCT 3D image of the PDMS/Ni@Ag (5.3vol%) film to illustrate the aggregation of the Ni@Ag particles. The top inset illustrates the top down projection of the aggregates, while the bottom inset shows the cross-section of the Ni@Ag particles in the film.

6.4. Conclusion

Core-shell Ni@Ag / PDMS composite films with tunable through-thickness piezo-resistivity are demonstrated using manufacturable R2R processing via magnetic field assisted alignment. The magnetic field promotes formation of chains of particles that align in the through thickness (“Z”) direction. Compression of these aligned PDMS/Ni@Ag films at low particle concentrations (<5 vol%) leads to an appreciable decrease in the electrical resistivity at a threshold critical pressure. At lower pressures, the resistivity is effectively unchanged in comparison to the initial state with a high resistivity (ca. 10^5 ohm·m), but application of pressures greater than this threshold pressure leads to 5-6 orders of magnitude decrease in the resistivity. This piezo-resistive behavior is controlled by the formation of new percolating conductive particle chains by closing the interparticle gaps during compression. This behavior is distinct from prior reports of pressure dependent electrical properties of aligned particles, where the resistance monotonically decreased due to decreased interparticle tunneling distance.[42] X-ray tomography illustrates a larger interparticle gap at lower Ni@Ag concentrations, which leads to larger pressure required to close the gap to form new percolated particle chains. The surface morphology can also be tuned with the Ni@Ag concentration and the magnetic field strength. A mylar sheet is demonstrated to be sufficient to maintain a flat interface, but without this constraint at PDMS/air interface, spiky surface features can be generated with tunable morphology ranging from nearly flat to large spikes to small features as the Ni@Ag content increases. These features

have the potential to add functionality to these composites for applications such as biopotential sensors.

CHAPTER VII

SUMMARY

The first objective of this dissertation is to broaden our understanding of Fused Filament fabrication (FFF) 3D-printing process as a polymer processing technique. Melt extrusion in FFF 3D-printing was demonstrated to be highly non-isothermal. In CHAPTER III, an experimental approach was developed to elucidate the complex temperature and flow history in the FFF extrusion process. Pigments were used as flow indicators to elucidate the flow history of FFF extrusion processes. The measured pigment distribution in extruded filaments indicates a more blunted velocity profile of FFF extrusion process as compared to that expected for an isothermal flow of Power-law fluid, especially at high extrusion speed. Real-time temperature measurement demonstrates the existence of radial temperature gradient, which become more significant at higher extrusion speed, by showing the center of the filament in liquefier is cooler than the set temperature. The results of pigment distribution measurement combined with the measured temperature history suggests that the temperature gradient in the liquefier is a major factor controlling the flow history of FFF extrusion process.

The second part of this dissertation aims to provide a novel approach of using core-shell filament to overcome the inherent trade-off between interfacial

bond strength and dimensional accuracy. In CHAPTER IV, the development of a co-extrusion system for core-shell filament fabrication is elucidated. It is demonstrated that printing at high processing temperature can promote part-filling and mechanical properties while potentially leads to deformed shape of the 3D-printed part. PC based core-shell filaments composed of high glass-transition temperature (T_g) cores and shells with low T_g or low melt viscosity are demonstrated to provide synergistic improvement of impact properties as compared to parts printed with pure core materials or shell materials. Meanwhile, core-shell filaments broaden the processing temperature window of FFF 3D printing by providing a good dimensional accuracy at high temperature and enabling extruding at low temperature. In Chapter V, we also demonstrates a simple core(PC)−shell(Surlyn) filament can enable synergistic impact performance enhancement through the generation of new pathways for energy dissipation and composite-like reinforcement. The printing orientation and composition of the core−shell filament are demonstrated both important factors in determining the available mechanisms for energy dissipation in 3D-printed PC@Surlyn objects. Individually, parts 3D printed with either PC or Surlyn leads to high susceptibility for crack propagation, an eventually causes catastrophic failure on impact. The use of the core−shell filament provides reinforcement from the continuous PC fibers that are oriented along the printing direction. For sample printed at XY and XZ orientation, delamination of Surlyn from PC and stretching of PC fibers dissipate the energy from impact loading, which can provide unprecedented impact resistance for 3D-printed polymer parts. Additionally, the tensile stretching of the PC@Surlyn objects shows ductile behavior which allow it to absorb more energy than parts printed with

PC or Surlyn individually. 3Dprinting of PC@Surlyn filaments also demonstrated to be less susceptible to warpage deformation because internal stress is mitigated by Surlyn shell. The increased robustness and dimensional accuracy of the 3D-printed parts will enable the use of core−shell filaments for high-performance applications where the brittle and failure prone nature of standard 3D-printed parts are unacceptable.

The third part of this dissertation describes the development of core-shell Ni@Ag / PDMS composite films with tunable through-thickness piezo-resistivity using manufacturable R2R processing via magnetic field assisted alignment. In Chapter VI, we demonstrate that magnetic field generated by a pair of electromagnets can induce the formation of chains of Ni@Ag particles aligned along thickness (“Z”) direction in PDMS matrix. Thermal curing of PDMS precursor during the alignment keeps the aligned structures of Ni@Ag particles. Compression of these aligned PDMS/Ni@Ag films at low particle concentrations (<5 vol%) leads to an appreciable decrease in the electrical resistivity at a threshold critical pressure. At lower pressures, the resistivity is effectively unchanged in comparison to the initial state with a high resistivity (ca. 10^5 ohm·m), but application of pressures greater than this threshold pressure leads to 5-6 orders of magnitude decrease in the resistivity. This piezo-resistive behavior is controlled by the formation of new percolating conductive particle chains by closing the interparticle gaps during compression. This behavior is distinct from prior reports of pressure dependent electrical properties of aligned particles, where the resistance monotonically decreased due to decreased interparticle tunneling distance.[42] X-ray tomography illustrates a larger

interparticle gap at lower Ni@Ag concentrations, which leads to larger pressure required to close the gap to form new percolated particle chains. The surface morphology can also be tuned with the Ni@Ag concentration and the magnetic field strength. When the magnetic field alignment is proceeded without the constraint of Mylar sheet at PDMS/air interface, spiky surface features can be generated with tunable morphology ranging from nearly flat to large spikes to small features as the Ni@Ag content increases. These features have the potential to add functionality to these composites for applications such as biopotential sensors.

REFERENCES

(1) ASTM International. ISO/ASTM 52900 - Standard Terminology for Additive Manufacturing Technologies. *Rapid Manuf. Assoc.* **2016**, 10–12. https://doi.org/10.1520/F2792-12A.2.

(2) Vashishtha, V. K.; Makade, R.; Mehla, N. Advancement of Rapid Prototyping in Aerospace Industry-a Review. *Int. J. Eng. Sci. Technol.* **2011**, *3* (3), 2486–2493.

(3) Kroll, E.; Artzi, D. Enhancing Aerospace Engineering Students' Learning with 3D Printing Wind-Tunnel Models. *Rapid Prototyp. J.* **2011**, *17* (5), 393–402.

(4) Bennett, G. R. The Application of Virtual Prototyping in the Development of Complex Aerospace Products. *Aircr. Eng. Aerosp. Technol.* **1997**, *69* (1), 19–25.

(5) Stroop, J.; Stolpe, R. Prototyping of Automotive Control Systems in a Time-Triggered Environment Using Flexray. In *Computer Aided Control System Design, 2006 IEEE International Conference on Control Applications, 2006 IEEE International Symposium on Intelligent Control, 2006 IEEE*; IEEE, 2006; pp 2332–2337.

(6) Döllner, G.; Kellner, P.; Tegel, O. Digital Mock-up and Rapid Prototyping in Automotive Product Development. *J. Integr. Des. Process Sci.* **2000**, *4* (1), 55–66.

(7) Elverum, C. W.; Welo, T. On the Use of Directional and Incremental Prototyping in the Development of High Novelty Products: Two Case Studies in the Automotive Industry. *J. Eng. Technol. Manag.* **2015**, *38*, 71–88.

(8) Lantada, A. D.; Morgado, P. L. Rapid Prototyping for Biomedical Engineering: Current Capabilities and Challenges. *Annu. Rev. Biomed. Eng.* **2012**, *14*, 73–96.

(9) Webb, P. A. A Review of Rapid Prototyping (RP) Techniques in the Medical and Biomedical Sector. *J. Med. Eng. Technol.* **2000**, *24* (4), 149–153.

(10) Williams, J. V; Revington, P. J. Novel Use of an Aerospace Selective Laser Sintering Machine for Rapid Prototyping of an Orbital Blowout Fracture. *Int. J. Oral Maxillofac. Surg.* **2010**, *39* (2), 182–184.

(11) McCullough, E. J.; Yadavalli, V. K. Surface Modification of Fused Deposition Modeling ABS to Enable Rapid Prototyping of Biomedical Microdevices. *J. Mater. Process. Technol.* **2013**, *213* (6), 947–954.

(12) Hollister, S. J.; Green, G. E.; Morrison, R. J.; Hollister, S. J.; Niedner, M. F.; Mahani, M. G.; Park, A. H.; Mehta, D. K.; Ohye, R. G.; Green, G. E. Mitigation of Tracheobronchomalacia with 3D- Printed Personalized Medical Devices in Pediatric Patients Mitigation of Tracheobronchomalacia with 3D-

Printed Personalized Medical Devices in Pediatric Patients. **2016**, *7* (April 2015), 1–12. https://doi.org/10.1126/scitranslmed.3010825.

(13) Kolesky, D. B.; Truby, R. L.; Gladman, A. S.; Busbee, T. A.; Homan, K. A.; Lewis, J. A. 3D Bioprinting of Vascularized, Heterogeneous Cell-Laden Tissue Constructs. *Adv. Mater.* **2014**, *26* (19), 3124–3130. https://doi.org/10.1002/adma.201305506.

(14) Fukuda, H. Additive Manufacturing Technology for Orthopedic Implants BT - Advances in Metallic Biomaterials: Processing and Applications; Niinomi, M., Narushima, T., Nakai, M., Eds.; Springer Berlin Heidelberg: Berlin, Heidelberg, 2015; pp 3–26. https://doi.org/10.1007/978-3-662-46842-5_1.

(15) Moroni, L.; de Wijn, J. R.; van Blitterswijk, C. a. 3D Fiber-Deposited Scaffolds for Tissue Engineering: Influence of Pores Geometry and Architecture on Dynamic Mechanical Properties. *Biomaterials* **2006**, *27* (7), 974–985. https://doi.org/10.1016/j.biomaterials.2005.07.023.

(16) Lee, K.-W.; Wang, S.; Fox, B. C.; Ritman, E. L.; Yaszemski, M. J.; Lu, L. Poly (Propylene Fumarate) Bone Tissue Engineering Scaffold Fabrication Using Stereolithography: Effects of Resin Formulations and Laser Parameters. *Biomacromolecules* **2007**, *8* (4), 1077–1084.

(17) Landers, R.; Mülhaupt, R. Desktop Manufacturing of Complex Objects, Prototypes and Biomedical Scaffolds by Means of Computer-Assisted Design Combined with Computer-Guided 3D Plotting of Polymers and Reactive Oligomers. *Macromol. Mater. Eng.* **2000**, *282* (Llm), 17–21. https://doi.org/10.1002/1439-2054(20001001)282:1<17::AID-MAME17>3.0.CO;2-8.

(18) Hardin, J. O.; Ober, T. J.; Valentine, A. D.; Lewis, J. A. Microfluidic Printheads for Multimaterial 3D Printing of Viscoelastic Inks. *Adv. Mater.* **2015**, *27* (21), 3279–3284.

(19) Yazdi, A. A.; Popma, A.; Wong, W.; Nguyen, T.; Pan, Y.; Xu, J. 3D Printing: An Emerging Tool for Novel Microfluidics and Lab-on-a-Chip Applications. *Microfluid. Nanofluidics* **2016**, *20* (3), 50.

(20) Bhattacharjee, N.; Urrios, A.; Kang, S.; Folch, A. The Upcoming 3D-Printing Revolution in Microfluidics. *Lab Chip* **2016**, *16* (10), 1720–1742.

(21) Wehner, M.; Truby, R. L.; Fitzgerald, D. J.; Mosadegh, B.; Whitesides, G. M.; Lewis, J. A.; Wood, R. J. An Integrated Design and Fabrication Strategy for Entirely Soft, Autonomous Robots. *Nature* **2016**, *536* (7617), 451.

(22) Sydney Gladman, A.; Matsumoto, E. A.; Nuzzo, R. G.; Mahadevan, L.; Lewis, J. A. Biomimetic 4D Printing. *Nat. Mater.* **2016**, *15* (4), 413–418. https://doi.org/10.1038/nmat4544.

(23) Lewis, J. A. Direct Ink Writing of 3D Functional Materials. *Adv. Funct. Mater.* **2006**, *16* (17), 2193–2204. https://doi.org/10.1002/adfm.200600434.

(24) Therriault, D.; Shepherd, R. F.; White, S. R.; Lewis, J. A. Fugitive Inks for Direct-Write Assembly of Three-Dimensional Microvascular Networks. *Adv. Mater.* **2005**, *17* (4), 395–399. https://doi.org/10.1002/adma.200400481.

(25) Barry, R. A.; Shepherd, R. F.; Hanson, J. N.; Nuzzo, R. G.; Wiltzius, P.; Lewis, J. A. Direct-Write Assembly of 3D Hydrogel Scaffolds for Guided Cell Growth. *Adv. Mater.* **2009**, *21* (23), 2407–2410. https://doi.org/10.1002/adma.200803702.

(26) Corbel, S.; Dufaud, O.; Roques-Carmes, T. Materials for Stereolithography. In *Stereolithography*; Springer, 2011; pp 141–159.

(27) Arcaute, K.; Mann, B.; Wicker, R. Stereolithography of Spatially Controlled Multi-Material Bioactive Poly (Ethylene Glycol) Scaffolds. *Acta Biomater.* **2010**, *6* (3), 1047–1054.

(28) Corcione, C. E.; Greco, A.; Maffezzoli, A. Photopolymerization Kinetics of an Epoxy-Based Resin for Stereolithography. *J. Appl. Polym. Sci.* **2004**, *92* (6), 3484–3491. https://doi.org/10.1002/app.20347.

(29) Schmidt, M.; Pohle, D.; Rechtenwald, T. Selective Laser Sintering of PEEK. *CIRP Ann. Technol.* **2007**, *56* (1), 205–208.

(30) Kumar, S. Selective Laser Sintering: A Qualitative and Objective Approach. *JOM* **2003**, *55* (10), 43–47. https://doi.org/10.1007/s11837-003-0175-y.

(31) Roskies, M.; Jordan, J. O.; Fang, D.; Abdallah, M. N.; Hier, M. P.; Mlynarek, A.; Tamimi, F.; Tran, S. D. Improving PEEK Bioactivity for Craniofacial Reconstruction Using a 3D Printed Scaffold Embedded with Mesenchymal Stem Cells. *J. Biomater. Appl.* **2016**, *31* (1), 132–139. https://doi.org/10.1177/0885328216638636.

(32) Mohamed, O. A.; Masood, S. H.; Bhowmik, J. L. Optimization of Fused Deposition Modeling Process Parameters: A Review of Current Research and Future Prospects. *Adv. Manuf.* **2015**, *3* (1), 42–53. https://doi.org/10.1007/s40436-014-0097-7.

(33) Sood, A. K.; Ohdar, R. K.; Mahapatra, S. S. Parametric Appraisal of Fused Deposition Modelling Process Using the Grey Taguchi Method. *Proc. Inst. Mech. Eng. Part B J. Eng. Manuf.* **2010**, *224* (1), 135–145. https://doi.org/10.1243/09544054JEM1565.

(34) Venkataraman, N.; Rangarajan, S.; Harper, B.; Matthewson, M. J.; Safari, A.; Danforth, S. C. Process-Property-Performance Relationship for Fused Deposition of Ceramics (FDC) Feedstock Materials. *MRS Proc.* **2000**, *625*, 203. https://doi.org/10.1557/PROC-625-203.

(35) Lee, W.; Wei, C.; Chung, S.-C. Development of a Hybrid Rapid Prototyping System Using Low-Cost Fused Deposition Modeling and Five-Axis Machining. *J. Mater. Process. Technol.* **2014**, *214* (11), 2366–2374.

(36) Wang, T.-M.; Xi, J.-T.; Jin, Y. A Model Research for Prototype Warp Deformation in the FDM Process. *Int. J. Adv. Manuf. Technol.* **2006**, *33* (11–12), 1087–1096. https://doi.org/10.1007/s00170-006-0556-9.

(37) Turner, B. N.; Gold, S. A. A Review of Melt Extrusion Additive Manufacturing Processes: II. Materials, Dimensional Accuracy, and Surface Roughness. *Rapid Prototyp. J.* **2015**, *21* (3), 250–261. https://doi.org/10.1108/RPJ-02-2013-0017.

(38) Zhang, Y.; Chou, Y. K. Three-Dimensional Finite Element Analysis Simulations of the Fused Deposition Modelling Process. *Proc. Inst. Mech. Eng. Part B J. Eng. Manuf.* **2006**, *220* (10), 1663–1671. https://doi.org/10.1243/09544054JEM572.

(39) Chin Ang, K.; Fai Leong, K.; Kai Chua, C.; Chandrasekaran, M. Investigation of the Mechanical Properties and Porosity Relationships in Fused Deposition Modelling-Fabricated Porous Structures. *Rapid Prototyp. J.* **2006**, *12* (2), 100–105.

(40) Es-Said, O. S.; Foyos, J.; Noorani, R.; Mendelson, M.; Marloth, R.; Pregger, B. A. Effect of Layer Orientation on Mechanical Properties of Rapid Prototyped Samples. *Mater. Manuf. Process.* **2000**, *15* (1), 107–122. https://doi.org/10.1080/10426910008912976.

(41) Lafleur, P. G.; Vergnes, B. Single-Screw Extrusion. *Polym. Extrus.* **2014**, 37–108.

(42) Gajdoš, I.; Slota, J. Influence of Printing Conditions on Structure in FDM Prototypes. *Tech. Gaz.* **2013**, *20* (2), 231–236. https://doi.org/658.512.2:004.896.

(43) Ramanath, H. S.; Chua, C. K.; Leong, K. F.; Shah, K. D. Melt Flow Behaviour of Poly-Epsilon-Caprolactone in Fused Deposition Modelling. *J. Mater. Sci. Mater. Med.* **2008**, *19* (7), 2541–2550. https://doi.org/10.1007/s10856-007-3203-6.

(44) Kim, Y. H.; Wool, R. P. A Theory of Healing at a Polymer-Polymer Interface. *Macromolecules* **1983**, *16* (7), 1115–1120. https://doi.org/10.1021/ma00241a013.

(45) Dawoud, M.; Taha, I.; Ebeid, S. J. Mechanical Behaviour of ABS: An Experimental Study Using FDM and Injection Moulding Techniques. *J. Manuf. Process.* **2016**, *21*, 39–45. https://doi.org/10.1016/j.jmapro.2015.11.002.

(46) Torrado Perez, A. R.; Roberson, D. A.; Wicker, R. B. Fracture Surface Analysis of 3D-Printed Tensile Specimens of Novel ABS-Based Materials. *J. Fail. Anal. Prev.* **2014**, *14* (3), 343–353. https://doi.org/10.1007/s11668-014-9803-9.

(47) Tymrak, B. M.; Kreiger, M.; Pearce, J. M. Mechanical Properties of Components Fabricated with Open-Source 3-D Printers under Realistic

Environmental Conditions. *Mater. Des.* **2014**, *58*, 242–246. https://doi.org/10.1016/j.matdes.2014.02.038.

(48) Anitha, R.; Arunachalam, S.; Radhakrishnan, P. Critical Parameters Influencing the Quality of Prototypes in Fused Deposition Modelling. *J. Mater. Process. Technol.* **2001**, *118* (1–3), 385–388. https://doi.org/10.1016/S0924-0136(01)00980-3.

(49) Sood, A. K.; Ohdar, R. K.; Mahapatra, S. S. Parametric Appraisal of Mechanical Property of Fused Deposition Modelling Processed Parts. *Mater. Des.* **2010**, *31* (1), 287–295. https://doi.org/10.1016/j.matdes.2009.06.016.

(50) Domingo-Espin, M.; Borros, S.; Agulló, N.; García-Granada, A.-A.; Reyes, G. Influence of Building Parameters on the Dynamic Mechanical Properties of Polycarbonate Fused Deposition Modeling Parts. *3D Print. Addit. Manuf.* **2014**, *1* (2), 70–77. https://doi.org/10.1089/3dp.2013.0007.

(51) Ahn, S.-H.; Montero, M.; Odell, D.; Roundy, S.; Wright, P. K. Anisotropic Material Properties of Fused Deposition Modeling ABS. *Rapid Prototyp. J.* **2002**, *8* (4), 248–257. https://doi.org/10.1108/13552540210441166.

(52) Rezayat, H.; Zhou, W.; Siriruk, A.; Penumadu, D.; Babu, S. S. Structure–mechanical Property Relationship in Fused Deposition Modelling. *Mater. Sci. Technol.* **2015**, *31* (8), 895–903. https://doi.org/10.1179/1743284715Y.0000000010.

(53) Sun, Q.; Rizvi, G. M.; Bellehumeur, C. T.; Gu, P. Experimental Study of the Cooling Characteristics of Polymer Filaments in FDM and Impact on the Mesostructures and Properties of Prototypes. *Solid Free. Fabr. Proc.* **2003**, No. 403, 313–323.

(54) Domingo-Espin, M.; Puigoriol-Forcada, J. M.; Garcia-Granada, A. A.; Llumà, J.; Borros, S.; Reyes, G. Mechanical Property Characterization and Simulation of Fused Deposition Modeling Polycarbonate Parts. *Mater. Des.* **2015**, *83*, 670–677. https://doi.org/10.1016/j.matdes.2015.06.074.

(55) Zhang, Y.; Chou, K. A Parametric Study of Part Distortions in Fused Deposition Modelling Using Three-Dimensional Finite Element Analysis. *Proc. Inst. Mech. Eng. Part B J. Eng. Manuf.* **2008**, *222*, 959–967. https://doi.org/10.1243/09544054JEM990.

(56) Carutasu, N. L.; Simion, I.; Carutasu, G.; Jiga, G.; Arion, A. F. Experimental Test for Elastic and Mechanical Evaluation of ABS Plastic Used in 3D Printing. *Mater. Plast.* **2015**, *52* (3), 397–401.

(57) Sun, Q.; Rizvi, G. M. M.; Bellehumeur, C. T. T.; Gu, P. Effect of Processing Conditions on the Bonding Quality of FDM Polymer Filamentsnull. *Rapid Prototyp. J.* **2008**, *14* (2), 72–80. https://doi.org/10.1108/13552540810862028.

(58) Pikkula, B. M.; Tunnell, J. W.; Chang, D. W.; Anvari, B. Effects of

Droplet Velocity, Diameter, and Film Height on Heat Removal during Cryogen Spray Cooling. *Ann. Biomed. Eng.* **2004**, *32* (8), 1133–1142.

(59) Lee, B. H.; Abdullah, J.; Khan, Z. A. Optimization of Rapid Prototyping Parameters for Production of Flexible ABS Object. *J. Mater. Process. Technol.* **2005**, *169* (1), 54–61. https://doi.org/10.1016/j.jmatprotec.2005.02.259.

(60) Bellehumeur, C.; Li, L.; Sun, Q.; Gu, P. Modeling of Bond Formation Between Polymer Filaments in the Fused Deposition Modeling Process. *J. Manuf. Process.* **2004**, *6* (2), 170–178. https://doi.org/10.1016/S1526-6125(04)70071-7.

(61) Manapat, J. Z.; Chen, Q.; Ye, P.; Advincula, R. C. 3D Printing of Polymer Nanocomposites via Stereolithography. *1600553*, 1–13. https://doi.org/10.1002/mame.201600553.

(62) Pennington, R. C.; Hoekstra, N. L.; Newcomer, J. L. Significant Factors in the Dimensional Accuracy of Fused Deposition Modelling. *Proc. Inst. Mech. Eng. Part E J. Process Mech. Eng.* **2005**, *219* (1), 89–92.

(63) Print Quality Troubleshooting Guide | Simplify3D Software https://www.simplify3d.com/support/print-quality-troubleshooting/#overheating (accessed Oct 4, 2018).

(64) Krebs, F. C.; Tromholt, T.; Jørgensen, M. Upscaling of Polymer Solar Cell Fabrication Using Full Roll-to-Roll Processing. *Nanoscale* **2010**, *2* (6), 873–886.

(65) Jain, K.; Klosner, M.; Zemel, M.; Raghunandan, S. Flexible Electronics and Displays: High-Resolution, Roll-to-Roll, Projection Lithography and Photoablation Processing Technologies for High-Throughput Production. *Proc. IEEE* **2005**, *93* (8), 1500–1510.

(66) Das, R. N.; Egitto, F. D.; Wilson, B.; Poliks, M. D.; Markovich, V. R. Development of Rigid-Flex and Multilayer Flex for Electronic Packaging. In *Electronic Components and Technology Conference (ECTC), 2010 Proceedings 60th*; IEEE, 2010; pp 568–574.

(67) Søndergaard, R. R.; Hösel, M.; Krebs, F. C. Roll-to-Roll Fabrication of Large Area Functional Organic Materials. *J. Polym. Sci. Part B Polym. Phys.* **2013**, *51* (1), 16–34. https://doi.org/10.1002/polb.23192.

(68) Song, D.-P.; Naik, A.; Li, S.; Ribbe, A.; Watkins, J. J. Rapid, Large-Area Synthesis of Hierarchical Nanoporous Silica Hybrid Films on Flexible Substrates. *J. Am. Chem. Soc.* **2016**, *138* (41), 13473–13476.

(69) Cakmak, M.; Batra, S. Continuous Roll-to-Roll Process Design for Vertical Alignment of Particles Using Electric Field. Google Patents March 31, 2016.

(70) Batra, S.; Unsal, E.; Cakmak, M. Directed Electric Field Z-Alignment

Kinetics of Anisotropic Nanoparticles for Enhanced Ionic Conductivity. *Adv. Funct. Mater.* **2014**, *24* (48), 7698–7708.

(71) Guo, Y.; Chen, Y.; Wang, E.; Cakmak, M. Roll-to-Roll Continuous Manufacturing Multifunctional Nanocomposites by Electric-Field-Assisted "Z" Direction Alignment of Graphite Flakes in Poly (Dimethylsiloxane). *ACS Appl. Mater. Interfaces* **2016**, *9* (1), 919–929.

(72) Guo, Y.; Batra, S.; Chen, Y.; Wang, E.; Cakmak, M. Roll to Roll Electric Field "Z" Alignment of Nanoparticles from Polymer Solutions for Manufacturing Multifunctional Capacitor Films. *ACS Appl. Mater. Interfaces* **2016**, *8* (28), 18471–18480.

(73) Chen, Y.; Guo, Y.; Batra, S.; Unsal, E.; Wang, E.; Wang, Y. Y.; Liu, X.; Wang, Y. Y.; Cakmak, M. Large-Scale R2R Fabrication of Piezoresistive Films (Ni/PDMS) with Enhanced through Thickness Electrical and Thermal Properties by Applying a Magnetic Field. *RSC Adv.* **2015**, *5* (112), 92071–92079. https://doi.org/10.1039/C5RA17005B.

(74) Chen, Y.; Guo, Y.; Batra, S.; Wang, E.; Wang, Y.; Liu, X.; Wang, Y.; Cakmak, M. Transparent and through Thickness Conductive Polystyrene Films Using External Magnetic Fields for "Z" Alignment of Nickel Nanoparticles. *Nanoscale* **2015**, *7* (35), 14636–14642.

(75) Singh, G.; Batra, S.; Zhang, R.; Yuan, H.; Yager, K. G.; Cakmak, M.; Berry, B.; Karim, A. Large-Scale Roll-to-Roll Fabrication of Vertically Oriented Block Copolymer Thin Films. *ACS Nano* **2013**, *7* (6), 5291–5299.

(76) Hermsen, J. L.; Burke, T. M.; Seslar, S. P.; Owens, D. S.; Ripley, B. A.; Mokadam, N. A.; Verrier, E. D. Scan, Plan, Print, Practice, Perform: Development and Use of a Patient-Specific 3-Dimensional Printed Model in Adult Cardiac Surgery. *J. Thorac. Cardiovasc. Surg.* **2017**, *153* (1), 132–140.

(77) He, R.; Peng, F.; Dunn, W. E.; Kyu, T. Chemical and Electrochemical Stability Enhancement of Lithium Bis (Oxalato)Borate (LiBOB)-Modified Solid Polymer Electrolyte Membrane in Lithium Ion Half-Cells. *Electrochim. Acta* **2017**. https://doi.org/10.1016/j.electacta.2017.06.043.

(78) Chen, K.; Dreger, N. Z.; Peng, F.; Vogt, B. D.; Becker, M. L.; Cakmak, M. Nonlinear Mechano-Optical Behavior and Strain-Induced Structural Changes of l - Valine-Based Poly(Ester Urea)S. *Macromolecules* **2018**, acs.macromol.8b01176. https://doi.org/10.1021/acs.macromol.8b01176.

(79) Chen, K.; Yu, J.; Guzman, G.; Es-haghi, S. S.; Becker, M. L.; Cakmak, M. Role of Hydrogen Bonding on Nonlinear Mechano-Optical Behavior of L-Phenylalanine-Based Poly(Ester Urea)S. *Macromolecules* **2017**, *50* (3), 1075–1084. https://doi.org/10.1021/acs.macromol.6b02415.

(80) Huang, T.-M.; Pang, F.; Hsieh, I.-F.; Cakmak, M. Control of Radial Structural Gradient in PAN/Silver Nanofibers Using Solvent Vapor Treatment. *Synth. Met.* **2016**, *221*, 309–318.

(81) Stansbury, J. W.; Idacavage, M. J. 3D Printing with Polymers: Challenges among Expanding Options and Opportunities. *Dent. Mater.* **2016**, *32* (1), 54–64.

(82) Truby, R. L.; Lewis, J. A. Printing Soft Matter in Three Dimensions. *Nature* **2016**, *540* (7633), 371–378. https://doi.org/10.1038/nature21003.

(83) Ligon, S. C.; Liska, R.; Stampfl, J. J.; Gurr, M.; Mülhaupt, R.; Mülhaupt, R. Polymers for 3D Printing and Customized Additive Manufacturing. *Chem. Rev.* **2017**, *117* (15), 10212–10290. https://doi.org/10.1021/acs.chemrev.7b00074.

(84) Gabriel, S.; Hull, C. W. United States Patent (19). **1984**, No. 19.

(85) G.G. Liversidge, K.C. Cundy, J.F. Bishop, D. A. C. United States Patent (19) 54. **1980**, *96* (19), 62–66. https://doi.org/US005485919A.

(86) Melchels, F. P. W.; Feijen, J.; Grijpma, D. W. Biomaterials A Review on Stereolithography and Its Applications in Biomedical Engineering. *Biomaterials* **2010**, *31* (24), 6121–6130. https://doi.org/10.1016/j.biomaterials.2010.04.050.

(87) Jacobs, P. F. *Rapid Prototyping & Manufacturing: Fundamentals of Stereolithography*; Society of Manufacturing Engineers, 1992.

(88) Calvert, P.; Crockett, R. Chemical Solid Free-Form Fabrication: Making Shapes without Molds. *Chem. Mater.* **1997**, *9* (3), 650–663. https://doi.org/10.1021/cm9604726.

(89) Resins, S. P. Investigation of Shrinkage-Induced Stresses in Stereolithography Photo-Curable Resins. 439–444.

(90) Scalera, F.; Esposito Corcione, C.; Montagna, F.; Sannino, A.; Maffezzoli, A. Development and Characterization of UV Curable Epoxy/Hydroxyapatite Suspensions for Stereolithography Applied to Bone Tissue Engineering. *Ceram. Int.* **2014**, *40* (10), 15455–15462. https://doi.org/10.1016/j.ceramint.2014.06.117.

(91) Crivello, J. V; Dietliker, K. Photoinitiators for Free Radical Cationic & Anionic Photopolymerisation. **1998**.

(92) Gibson, I.; Rosen, D. W.; Stucker, B. Additive Manufacturing Technologies. 2010. *Google Sch.* **2015**, *44* (8), 085201. https://doi.org/10.1007/978-1-4939-2113-3.

(93) Kim, K.; Dean, D.; Wallace, J.; Breithaupt, R.; Mikos, A. G.; Fisher, J. P. The Influence of Stereolithographic Scaffold Architecture and Composition on Osteogenic Signal Expression with Rat Bone Marrow Stromal Cells. *Biomaterials* **2011**, *32* (15), 3750–3763.

(94) Kucybała, Z.; Pietrzak, M.; Pączkowski, J.; Lindén, L.-Å.; Rabek, J. F. Kinetic Studies of a New Photoinitiator Hybrid System Based on

Camphorquinone-N-Phenylglicyne Derivatives for Laser Polymerization of Dental Restorative and Stereolithographic (3D) Formulations. *Polymer (Guildf).* **1996**, *37* (20), 4585–4591.

(95) Chia, H. N.; Wu, B. M. Recent Advances in 3D Printing of Biomaterials. *J. Biol. Eng.* **2015**, *9* (1), 1–15. https://doi.org/10.1186/s13036-015-0001-4.

(96) Maruo, S.; Nakamura, O.; Kawata, S. Three-Dimensional Microfabrication with Two-Photon-Absorbed Photopolymerization. *Opt. Lett.* **1997**, *22* (2), 132. https://doi.org/10.1364/OL.22.000132.

(97) Xing, J.-F.; Zheng, M.-L.; Duan, X.-M. Two-Photon Polymerization Microfabrication of Hydrogels: An Advanced 3D Printing Technology for Tissue Engineering and Drug Delivery. *Chem. Soc. Rev.* **2015**, *44* (15), 5031–5039. https://doi.org/10.1039/C5CS00278H.

(98) Qin, X. H.; Ovsianikov, A.; Stampfl, J.; Liska, R. Additive Manufacturing of Photosensitive Hydrogels for Tissue Engineering Applications. *BioNanoMaterials* **2014**, *15* (3–4), 49–70. https://doi.org/10.1515/bnm-2014-0008.

(99) Xing, J.; Liu, J.; Zhang, T.; Zhang, L.; Zheng, M.; Duan, X. A Water Soluble Initiator Prepared through Host-Guest Chemical Interaction for Microfabrication of 3D Hydrogels via Two-Photon Polymerization. *J. Mater. Chem. B* **2014**, *2* (27), 4318–4323. https://doi.org/10.1039/c4tb00414k.

(100) Badev, A.; Abouliatim, Y.; Chartier, T.; Lecamp, L.; Lebaudy, P.; Chaput, C.; Delage, C. Photopolymerization Kinetics of a Polyether Acrylate in the Presence of Ceramic Fillers Used in Stereolithography. *J. Photochem. Photobiol. A Chem.* **2011**, *222* (1), 117–122. https://doi.org/10.1016/j.jphotochem.2011.05.010.

(101) Sun, C.; Fang, N.; Wu, D. M.; Zhang, X. Projection Micro-Stereolithography Using Digital Micro-Mirror Dynamic Mask. *Sensors Actuators, A Phys.* **2005**, *121* (1), 113–120. https://doi.org/10.1016/j.sna.2004.12.011.

(102) Takagi, T.; Nakajima, N. Photoforming Applied to Fine Machining. In *Micro Electro Mechanical Systems, 1993, MEMS'93, Proceedings An Investigation of Micro Structures, Sensors, Actuators, Machines and Systems. IEEE.*; IEEE, 1993; pp 173–178.

(103) Tumbleston, J. R.; Shirvanyants, D.; Ermoshkin, N.; Janusziewicz, R.; Johnson, A. R.; Kelly, D.; Chen, K.; Pinschmidt, R.; Rolland, J. P.; Ermoshkin, A.; et al. Continuous Liquid Interface Production Of3D Objects. *Science (80-.).* **2015**, *347* (6228), 1349–1352. https://doi.org/10.1126/science.aaa2397.

(104) He, Y.; Wildman, R. D.; Tuck, C. J.; Christie, S. D. R.; Edmondson, S. An Investigation of the Behavior of Solvent Based Polycaprolactone Ink for Material Jetting. *Sci. Rep.* **2016**, *6* (February), 1–10. https://doi.org/10.1038/srep20852.

(105) Bass, L.; Meisel, N. A.; Williams, C. B. Exploring Variability of Orientation and Aging Effects in Material Properties of Multi-Material Jetting Parts. *Rapid Prototyp. J.* **2016**, *22* (5), 826–834. https://doi.org/10.1108/RPJ-11-2015-0169.

(106) Stratasys. PolyJet Materials White Paper | Stratasys http://www.stratasys.com/resources/search/white-papers/polyjet-materials?utm_source=google&utm_medium=cpc&utm_campaign=whyssys&cid=7010Y0000006mFeQAI&utm_ad=&utm_source=google&utm_term=stratasys polyjet printer&utm_campaign=Search+-+US+-+Brand&utm_med (accessed Sep 23, 2018).

(107) Napadensky, E. Compositions and Methods for Use in Three Dimensional Model Printing. Google Patents May 27, 2003.

(108) Van der Schueren, B.; Kruth, J.-P. Powder Deposition in Selective Metal Powder Sintering. *Rapid Prototyp. J.* **1995**, *1* (3), 23–31.

(109) Manthiram, A.; Bourell, D. L.; Marcus, H. L. Nanophase Materials in Solid Freeform Fabrication. *JOM* **1993**, *45* (11), 66–70.

(110) Schmid, M.; Amado, A.; Wegener, K. Materials Perspective of Polymers for Additive Manufacturing with Selective Laser Sintering. *J. Mater. Res.* **2014**, *29* (17), 1824–1832. https://doi.org/10.1557/jmr.2014.138.

(111) Sachs, E. M.; Haggerty, J. S.; Cima, M. J.; Williams, P. A. Three-Dimensional Printing Techniques. Google Patents April 20, 1993.

(112) Gratson, G. M.; Xu, M.; Lewis, J. A. Microperiodic Structures: Direct Writing of Three-Dimensional Webs. *Nature* **2004**, *428* (6981), 386.

(113) Channell, G. M.; Miller, K. T.; Zukoski, C. F. Effects of Microstructure on the Compressive Yield Stress. *AIChE J.* **2000**, *46* (1), 72–78.

(114) Herschel, W. H.; Bulkley, R. Konsistenzmessungen von Gummi-Benzollösungen. *Colloid Polym. Sci.* **1926**, *39* (4), 291–300.

(115) Zhao, M.; Eghtesadi, S. A.; Dawadi, M. B.; Wang, C.; Huang, S.; Seymore, A. E.; Vogt, B. D.; Modarelli, D. A.; Liu, T.; Zacharia, N. S. Partitioning of Small Molecules in Hydrogen-Bonding Complex Coacervates of Poly (Acrylic Acid) and Poly (Ethylene Glycol) or Pluronic Block Copolymer. *Macromolecules* **2017**, *50* (10), 3818–3830.

(116) Huang, C.; Wang, C.; Chen, Q.; Colby, R. H.; Weiss, R. A. Reversible Gelation Model Predictions of the Linear Viscoelasticity of Oligomeric Sulfonated Polystyrene Ionomer Blends. *Macromolecules* **2016**, *49* (10), 3936–3947.

(117) Wang, C.; Wiener, C. G.; Cheng, Z.; Vogt, B. D.; Weiss, R. A. Modulation of the Mechanical Properties of Hydrophobically Modified Supramolecular Hydrogels by Surfactant-Driven Structural Rearrangement.

Macromolecules **2016**, *49* (23), 9228–9238.

(118) Zhang, H.; Wang, C.; Zhu, G.; Zacharia, N. S. Self-Healing of Bulk Polyelectrolyte Complex Material as a Function of PH and Salt. *ACS Appl. Mater. Interfaces* **2016**, *8* (39), 26258–26265.

(119) Wang, C.; Duan, Y.; Zacharia, N. S.; Vogt, B. D. A Family of Mechanically Adaptive Supramolecular Graphene Oxide/Poly (Ethylenimine) Hydrogels from Aqueous Assembly. *Soft Matter* **2017**, *13* (6), 1161–1170.

(120) Yang, Y.; Wang, C.; Wiener, C. G.; Hao, J.; Shatas, S.; Weiss, R. A.; Vogt, B. D. Tough Stretchable Physically-Cross-Linked Electrospun Hydrogel Fiber Mats. *ACS Appl. Mater. Interfaces* **2016**, *8* (35), 22774–22779.

(121) Zhu, G. H.; Zhang, C.; Wang, C.; Zacharia, N. S. Gel-Infused Slippery Surface with Enhanced Longevity and Thermally Controllable Sliding Properties. *Adv. Mater. Interfaces* **2016**, *3* (20), 1600515.

(122) Wang, C.; Wiener, C. G.; Yang, Y.; Weiss, R. A.; Vogt, B. D. Structural Rearrangement and Stiffening of Hydrophobically Modified Supramolecular Hydrogels during Thermal Annealing. *J. Polym. Sci. Part B Polym. Phys.* **2017**, *55* (13), 1036–1044.

(123) Wiener, C. G.; Wang, C.; Liu, Y.; Weiss, R. A.; Vogt, B. D. Nanostructure Evolution during Relaxation from a Large Step Strain in a Supramolecular Copolymer-Based Hydrogel: A SANS Investigation. *Macromolecules* **2017**, *50* (4), 1672–1680.

(124) Xia, Y.; Wang, C.; Li, R.; Fukuto, M.; Vogt, B. D. Sulfur Diffusion within Nitrogen-Doped Ordered Mesoporous Carbons Determined by in Situ X-Ray Scattering. *Langmuir* **2018**, *34* (30), 8767–8776.

(125) Qiao, X.; Wang, X.; Wang, C.; Weiss, R. A. Effect of Zinc Stearate on the Properties of a Sulfonated Polystyrene Ionomer. *J. Rheol. (N. Y. N. Y).* **2018**, *62* (4), 821–830.

(126) Duan, Y.; Wang, C.; Zhao, M.; Vogt, B. D.; Zacharia, N. S. Mechanical Properties of Bulk Graphene Oxide/Poly (Acrylic Acid)/Poly (Ethylenimine) Ternary Polyelectrolyte Complex. *Soft Matter* **2018**, *14* (21), 4396–4403.

(127) Ye, C.; Wang, C.; Wang, J.; Wiener, C. G.; Xia, X.; Cheng, S. Z. D.; Li, R.; Yager, K. G.; Fukuto, M.; Vogt, B. D. Rapid Assessment of Crystal Orientation in Semi-Crystalline Polymer Films Using Rotational Zone Annealing and Impact of Orientation on Mechanical Properties. *Soft Matter* **2017**, *13* (39), 7074–7084.

(128) Clausen, A.; Wang, F.; Jensen, J. S.; Sigmund, O.; Lewis, J. A. Topology Optimized Architectures with Programmable Poisson's Ratio over Large Deformations. *Adv. Mater.* **2015**, *27* (37), 5523–5527. https://doi.org/10.1002/adma.201502485.

(129) Huang, S.; Zhao, M.; Wang, C.; Zacharia, N. Effects of Small Molecules on Coacervation of Poly (Diallyldimethylammoniumchloride) and Poly (Sodium 4-Styrenesulfonate). In *ABSTRACTS OF PAPERS OF THE AMERICAN CHEMICAL SOCIETY*; AMER CHEMICAL SOC 1155 16TH ST, NW, WASHINGTON, DC 20036 USA, 2017; Vol. 254.

(130) Zhao, M.; Zacharia, N. S. Protein Encapsulation via Polyelectrolyte Complex Coacervation: Protection against Protein Denaturation. *J. Chem. Phys.* **2018**, *149* (16), 163326.

(131) Carvalho, C.; Landers, R.; Mülhaupt, R. Soft and Hard Implant Fabrication Using 3D-BioplottingTM. **2004**.

(132) Bhattacharjee, T.; Zehnder, S. M.; Rowe, K. G.; Jain, S.; Nixon, R. M.; Sawyer, W. G.; Angelini, T. E. Writing in the Granular Gel Medium. *Sci. Adv.* **2015**, *1* (8), 4–10. https://doi.org/10.1126/sciadv.1500655.

(133) S. Scott Crump. Apparatus and Method for Creating Three-Dimensional Objects. U.S. Patent June 9, 1992, p No. 5,121,329. 9.

(134) Safari, A. Processing of Advanced Electroceramic Components by Fused Deposition Technique. *Ferroelectrics* **2001**, *263* (1), 45–54. https://doi.org/10.1080/00150190108225177.

(135) 15 Best Cheap DIY 3D Printer Kits of Summer 2018 | All3DP https://all3dp.com/1/best-cheap-diy-3d-printer-kit/ (accessed Oct 7, 2018).

(136) Evans, B. *Practical 3D Printers: The Science and Art of 3D Printing*; Apress, 2012.

(137) Grutle, Ø. K. 5-Axis 3D Printer. 2015.

(138) Chakraborty, D.; Reddy, B. A.; Choudhury, A. R. Extruder Path Generation for Curved Layer Fused Deposition Modeling. *Comput. Des.* **2008**, *40* (2), 235–243.

(139) Guan, H. W.; Savalani, M. M.; Gibson, I.; Diegel, O. Influence of Fill Gap on Flexural Strength of Parts Fabricated by Curved Layer Fused Deposition Modeling. *Procedia Technol.* **2015**, *20*, 243–248.

(140) Extreme Versatility and Thermal Performance Provides Unlimited Potential | DuPont™ Kapton® | DuPont USA http://www.dupont.com/products-and-services/membranes-films/polyimide-films/brands/kapton-polyimide-film.html/ (accessed Sep 30, 2018).

(141) Singh, K. Experimental Study to Prevent the Warping of 3D Models in Fused Deposition Modeling. *Int. J. Plast. Technol.* **2018**. https://doi.org/10.1007/s12588-018-9206-y.

(142) Peng, F.; Zhao, Z.; Xia, X.; Cakmak, M.; Vogt, B. D. Enhanced Impact Resistance of Three-Dimensional-Printed Parts with Structured Filaments. *ACS*

Appl. Mater. Interfaces **2018**, *10* (18), 16087–16094. https://doi.org/10.1021/acsami.8b00866.

(143) Gardner, J. M.; Sauti, G.; Kim, J. W.; Cano, R. J.; Wincheski, R. A.; Stelter, C. J.; Grimsley, B. W.; Working, D. C.; Siochi, E. J. 3-D Printing of Multifunctional Carbon Nanotube Yarn Reinforced Components. *Addit. Manuf.* **2016**, *12*, 38–44. https://doi.org/10.1016/j.addma.2016.06.008.

(144) F123 Series Printers | Stratasys http://www.stratasys.com/3d-printers/f123 (accessed Sep 30, 2018).

(145) Halidi, S. N. A. M.; Abdullah, J. Moisture Effects on the ABS Used for Fused Deposition Modeling Rapid Prototyping Machine. In *Humanities, Science and Engineering Research (SHUSER), 2012 IEEE Symposium on*; IEEE, 2012; pp 839–843.

(146) Haipeng, P.; Tianrui, Z. Generation and Optimization of Slice Profile Data in Rapid Prototyping and Manufacturing. *J. Mater. Process. Technol.* **2007**, *187–188*, 623–626. https://doi.org/10.1016/j.jmatprotec.2006.11.221.

(147) N. Turner, B.; Strong, R.; A. Gold, S. A Review of Melt Extrusion Additive Manufacturing Processes: I. Process Design and Modeling. *Rapid Prototyp. J.* **2014**, *20* (3), 192–204. https://doi.org/10.1108/RPJ-01-2013-0012.

(148) Krotkỳ, J.; Honzíková, J.; Moc, P. Deformation of Print PLA Material Depending on the Temperature of Reheating Printing Pad. *Manuf. Technol.* **2016**, *16* (1), 136–140.

(149) Pérez, C. J. L. Analysis of the Surface Roughness and Dimensional Accuracy Capability of Fused Deposition Modelling Processes. *Int. J. Prod. Res.* **2002**, *40* (12), 2865–2881. https://doi.org/10.1080/00207540210146099.

(150) Agarwala, M. K.; Jamalabad, V. R.; Langrana, N. a.; Safari, A.; Whalen, P. J.; Danforth, S. C. Structural Quality of Parts Processed by Fused Deposition. *Rapid Prototyp. J.* **1996**, *2* (4), 4–19. https://doi.org/10.1108/13552549610732034.

(151) White, J. L.; Kondo, A. Flow Patterns in Polyethylene and Polystyrene Melts during Extrusion through a Die Entry Region: Measurement and Interpretation. *J. Nonnewton. Fluid Mech.* **1977**, *3* (1), 41–64. https://doi.org/10.1016/0377-0257(77)80011-6.

(152) Jang, S. H.; Park, Y. L.; Yin, H. Influence of Coalescence on the Anisotropic Mechanical and Electrical Properties of Nickel Powder/Polydimethylsiloxane Composites. *Materials (Basel).* **2016**, *9* (4). https://doi.org/10.3390/ma9040239.

(153) Bellini, A.; Güçeri, S.; Bertoldi, M. Liquefier Dynamics in Fused Deposition. *J. Manuf. Sci. Eng.* **2004**, *126* (2), 237. https://doi.org/10.1115/1.1688377.

(154) Yardimci, M. A.; Hattori, T.; Guceri, S. I.; Danforth, S. C. Thermal Analysis of Fused Deposition. *Proc. Solid Free. Fabr. Conf.* **1997**, 689–698.

(155) Mcilroy, C.; Olmsted, P. D. Disentanglement Effects on Welding Behaviour of Polymer Melts during the Fused- Fi Lament-Fabrication Method for Additive Manufacturing. *Polymer (Guildf).* **2017**, *123*, 376–391. https://doi.org/10.1016/j.polymer.2017.06.051.

(156) Yousefpour, A.; Hojjati, M.; Immarigeon, J.-P. Fusion Bonding/Welding of Thermoplastic Composites. *J. Thermoplast. Compos. Mater.* **2004**, *17* (4), 303–341. https://doi.org/10.1177/0892705704045187.

(157) Prager, S. The Healing Process at Polymer–polymer Interfaces. *J. Chem. Phys.* **1981**, *75* (10), 5194. https://doi.org/10.1063/1.441871.

(158) Daniels, E. S.; Klein, A. Development of Cohesive Strength in Polymer Films from Latices: Effect of Polymer Chain Interdiffusion and Crosslinking. *Prog. Org. Coatings* **1991**, *19* (4), 359–378. https://doi.org/10.1016/0033-0655(91)80018-E.

(159) Bastien, L. J.; Gillespie, J. W. A Non-Isothermal Healing Model for Strength and Toughness of Fusion Bonded Joints of Amorphous Thermoplastics. *Polym. Eng. Sci.* **1991**, *31* (24), 1720–1730. https://doi.org/10.1002/pen.760312406.

(160) and, F. Y.; Pitchumani*, R. Healing of Thermoplastic Polymers at an Interface under Nonisothermal Conditions. **2002**. https://doi.org/10.1021/MA010858O.

(161) de Gennes, P.-G. Reptation of a Polymer Chain in the Presence of Fixed Obstacles. *J. Chem. Phys.* **1971**, *55* (2), 572–579.

(162) Yang, F.; Pitchumani, R. Nonisothermal Healing and Interlaminar Bond Strength Evolution during Thermoplastic Matrix Composites Processing. *Polym. Compos.* **2003**, *24* (2), 263–278. https://doi.org/10.1002/pc.10027.

(163) Thomas, J. P.; Fodriguez, J. F. Modeling the Fracture Strength Between Fused-Deposition Extruded Roads. *Solid Free. Fabr. Proc.* **2000**, 17–23.

(164) Pokluda, O.; Bellehumeur, C. T.; Vlachopoulos, J. Modification of Frenkel's Model for Sintering. *AIChE J.* **1997**, *43* (12), 3253–3256. https://doi.org/10.1002/aic.690431213.

(165) Li, L.; Sun, Q.; Bellehumeur, C.; Gu, P. Investigation of Bond Formation in FDM Process. *Solid Free. Fabr. Proc.* **2002**, No. 403, 400–407. https://doi.org/10.1108/13552540810862028.

(166) Hill, N.; Haghi, M. Deposition Direction-Dependent Failure Criteria for Fused Deposition Modeling Polycarbonate. *Rapid Prototyp. J.* **2014**, *20* (3), 221–227. https://doi.org/10.1108/RPJ-04-2013-0039.

(167) Brian N Turner; Gold, S. A. A Review of Melt Extrusion Additive Manufacturing Processes: II. Materials, Dimensional Accuracy, and Surface Roughnessnull. *Rapid Prototyp. J.* **2015**, *21* (3), 250–261. https://doi.org/10.1108/RPJ-02-2013-0017.

(168) Lee, C. S.; Kim, S. G.; Kim, H. J.; Ahn, S. H. Measurement of Anisotropic Compressive Strength of Rapid Prototyping Parts. *J. Mater. Process. Technol.* **2007**, *187–188*, 627–630. https://doi.org/10.1016/j.jmatprotec.2006.11.095.

(169) Herrero, M.; Peng, F.; Núñez Carrero, K. Ca.; Merino, J. C.; Vogt, B. D. Renewable Nanocomposites for Additive Manufacturing Using Fused Filament Fabrication. *ACS Sustain. Chem. Eng.* **2018**, *6*, acssuschemeng.8b02919. https://doi.org/10.1021/acssuschemeng.8b02919.

(170) Zhang, L.; Gong, X.; Bao, Y.; Zhao, Y.; Xi, M.; Jiang, C.; Fong, H. Electrospun Nano Fi Brous Membranes Surface-Decorated with Silver Nanoparticles as Flexible and Active / Sensitive Substrates for Surface-Enhanced Raman Scattering. **2012**.

(171) Zhao, W.; Nugay, I. I.; Yalcin, B.; Cakmak, M. Flexible, Stretchable, Transparent and Electrically Conductive Polymer Films via a Hybrid Electrospinning and Solution Casting Process: In-Plane Anisotropic Conductivity for Electro-Optical Applications. *Displays* **2016**. https://doi.org/10.1016/j.displa.2016.01.001.

(172) Zhang, D.; Ryu, K.; Liu, X.; Polikarpov, E.; Ly, J.; Tompson, M. E.; Zhou, C. Transparent, Conductive, and Flexible Carbon Nanotube Films and Their Application in Organic Light-Emitting Diodes. *Nano Lett.* **2006**, *6* (9), 1880–1886. https://doi.org/10.1021/nl0608543.

(173) Kim, T.; Canlier, A.; Kim, G. H.; Choi, J.; Park, M.; Han, S. M. Electrostatic Spray Deposition of Highly Transparent Silver Nanowire Electrode on Flexible Substrate. *ACS Appl. Mater. Interfaces* **2013**, *5* (3), 788–794. https://doi.org/10.1021/am3023543.

(174) Lee, H.-H.; Chou, K.-S.; Shih, Z.-W. Effect of Nano-Sized Silver Particles on the Resistivity of Polymeric Conductive Adhesives. *Int. J. Adhes. Adhes.* **2005**, *25* (5), 437–441. https://doi.org/10.1016/j.ijadhadh.2004.11.008.

(175) Ye, L.; Lai, Z.; Liu, J.; Tholen, A. Effect of Ag Particle Size on Electrical Conductivity of Isotropically Conductive Adhesives. *IEEE Trans. Electron. Packag. Manuf.* **1999**, *22* (4), 299–302.

(176) Li, Y.; Wong, C. P. Recent Advances of Conductive Adhesives as a Lead-Free Alternative in Electronic Packaging: Materials, Processing, Reliability and Applications. *Mater. Sci. Eng. R Reports* **2006**, *51* (1–3), 1–35.

(177) Chun, K.; Oh, Y.; Rho, J.; Ahn, J.; Kim, Y.; Choi, H. R.; Baik, S. Highly Conductive , Printable and Stretchable Composite Films of Carbon Nanotubes and Silver. **2010**, *5* (December), 853–858.

https://doi.org/10.1038/NNANO.2010.232.

(178) Lise, S.; Swift, M. R.; Maritan, A. Precise Determination of the Critical Threshold and Exponents in a Three-Dimensional Precise Determination of the Critical Threshold and Exponents in a Three-Dimensional Continuum Percolation Model. *J. Phys. A. Math. Gen.* **1997**, *30* (16), 585–592.

(179) Sancaktar, E.; Dilsiz, N. Anisotropic Alignment of Nickel Particles in a Magnetic Field for Electronically Conductive Adhesives Applications. *J. Adhes. Sci. Technol.* **1997**, *11* (2), 155–166. https://doi.org/10.1163/156856197X00273.

(180) Trotsenko, O.; Tokarev, A.; Gruzd, A.; Enright, T.; Minko, S. Magnetic Field Assisted Assembly of Highly Ordered Percolated Nanostructures and Their Application for Transparent Conductive Thin Films. *Nanoscale* **2015**, *7* (16), 7155–7161. https://doi.org/10.1039/C5NR00154D.

(181) Ieda, M. Dielectric Breakdown Process of Polymers. *IEEE Trans. Electr. Insul.* **1980**, No. 3, 206–224.

(182) Varghese, O. K.; Paulose, M.; Grimes, C. A. Long Vertically Aligned Titania Nanotubes on Transparent Conducting Oxide for Highly Efficient Solar Cells. *Nat. Nanotechnol.* **2009**, *4* (9), 592–597. https://doi.org/10.1038/nnano.2009.226.

(183) Faraudo, J.; Andreu, J. S.; Camacho, J. Understanding Diluted Dispersions of Superparamagnetic Particles under Strong Magnetic Fields: A Review of Concepts, Theory and Simulations. *Soft Matter* **2013**, *9* (29), 6654. https://doi.org/10.1039/c3sm00132f.

(184) Hangarter, C. M.; Rheem, Y.; Yoo, B.; Yang, E. H.; Myung, N. V. Hierarchical Magnetic Assembly of Nanowires. *Nanotechnology* **2007**, *18* (20). https://doi.org/10.1088/0957-4484/18/20/205305.

(185) Zhu, L.; Xie, D.; Ma, J.; Shao, J.; Shen, X. Fabrication of Polydimethylsiloxane Composites with Nickel Particles and Nickel Fibers and Study of Their Magnetic Properties. *Smart Mater. Struct.* **2013**, *22* (4). https://doi.org/10.1088/0964-1726/22/4/045015.

(186) Mietta, J. L.; Ruiz, M. M.; Antonel, P. S.; Perez, O. E.; Butera, A.; Jorge, G.; Negri, R. M. Anisotropic Magnetoresistance and Piezoresistivity in Structured Fe3O4-Silver Particles in PDMS Elastomers at Room Temperature. *Langmuir* **2012**, *28* (17), 6985–6996.

(187) Steinert, B. W.; Dean, D. R. Magnetic Field Alignment and Electrical Properties of Solution Cast PET-Carbon Nanotube Composite Films. *Polymer (Guildf).* **2009**, *50* (3), 898–904. https://doi.org/10.1016/j.polymer.2008.11.053.

(188) Parsa, N.; Hawk, N.; Gasper, M. R.; Toonen, R. C.; Peng, F. Apparatus for Characterizing Millimeter-Wave Propagation through Magnetoelastic Multiferroic Materials. In *Cognitive Communications for Aerospace Applications*

Workshop (CCAA), 2017; IEEE, 2017; pp 1–4.

(189) Parsa, N.; Toonen, R. C.; Peng, F.; Cakmak, M. Voltage-Controlled, Nonreciprocal Millimeter-Wave Propagation From Magnetoelastic Membranes Infused With Aligned Nickel Microparticles. *IEEE Trans. Magn.* **2018**, No. 99, 1–5.

(190) Peng, F.; Vogt, B. D.; Cakmak, M. Complex Flow and Temperature History during Melt Extrusion in Material Extrusion Additive Manufacturing. *Addit. Manuf.* **2018**, *22* (August 2017), 197–206. https://doi.org/10.1016/j.addma.2018.05.015.

(191) ISO/ASTM. Standard Terminology for Additive Manufacturing – General Principles – Terminology. **2015**. https://doi.org/10.1520/F2792-12A.2.

(192) Comb, J. W.; Priedeman, W. R.; Turley, P. W. FDM Technology Process Improvements. In *Proceedings of Solid Freeform Fabrication Symposium*; DTIC Document, 1994; pp 42–49.

(193) Shojib Hossain, M.; Espalin, D.; Ramos, J.; Perez, M.; Wicker, R. Improved Mechanical Properties of Fused Deposition Modeling-Manufactured Parts Through Build Parameter Modifications. *J. Manuf. Sci. Eng.* **2014**, *136* (6), 061002. https://doi.org/10.1115/1.4028538.

(194) C. D. Han. *Rheology and Processing of Polymeric Materials Volume 1, Polymer Rheology*; Oxford University Press, 2007.

(195) Madenci, E.; Guven, I. *The Finite Element Method and Applications in Engineering Using ANSYS*®; Springer, 2015.

(196) Mostafa, N.; Syed, H. M.; Igor, S.; Andrew, G. A Study of Melt Flow Analysis of an ABS-Iron Composite in Fused Deposition Modelling Process. *Tsinghua Sci. Technol.* **2009**, *14*, 29–37. https://doi.org/10.1016/S1007-0214(09)70063-X.

(197) Marcus, S. M.; Blaine, R. L. Thermal Conductivity of Polymers, Glasses and Ceramics by Modulated DSC. *Thermochim. Acta* **1994**, *243* (2), 231–239. https://doi.org/10.1016/0040-6031(94)85058-5.

(198) Schumacher, C.; Bickel, B.; Rys, J.; Marschner, S.; Daraio, C.; Gross, M. Microstructures to Control Elasticity in 3D Printing. *ACM Trans. Graph.* **2015**, *34* (4), 136:1-136:13. https://doi.org/10.1145/2766926.

(199) Rodríguez, J. F.; Thomas, J. P.; Renaud, J. E. Mechanical Behavior of Acrylonitrile Butadiene Styrene Fused Deposition Materials Modeling. *Rapid Prototyp. J.* **2013**.

(200) Kousiatza, C.; Karalekas, D. In-Situ Monitoring of Strain and Temperature Distributions during Fused Deposition Modeling Process. *Mater. Des.* **2016**, *97*, 400–406. https://doi.org/10.1016/j.matdes.2016.02.099.

(201) Dinwiddie, R. B.; Kunc, V.; Lindal, J. M.; Post, B.; Smith, R. J.; Love, L.; Duty, C. E. Infrared Imaging of the Polymer 3D-Printing Process. In *SPIE Sensing Technology + Applications*; Colbert, F. P., Hsieh, S.-J. (Tony), Eds.; International Society for Optics and Photonics, 2014; p 910502. https://doi.org/10.1117/12.2053425.

(202) Chabbra, R.; Richarson, J. Non Newtonian Flow and Applied Rheology. Elsevier, Amsterdam 2008.

(203) Buffham, B. A.; Mason, G. Holdup and Dispersion: Tracer Residence Times, Moments and Inventory Measurements. *Chem. Eng. Sci.* **1993**, *48* (23), 3879–3887. https://doi.org/10.1016/0009-2509(93)80366-X.

(204) Franco, W.; Liu, J.; Wang, G.-X.; Nelson, J. S.; Aguilar, G. Radial and Temporal Variations in Surface Heat Transfer during Cryogen Spray Cooling. *Phys. Med. Biol.* **2005**, *50* (2), 387.

(205) Zheng, J.; Takahashi, S.; Yoshikawa, S.; Uchino, K.; Vries, J. W. C. de. Heat Generation in Multilayer Piezoelectric Actuators. *J. Am. Ceram. Soc.* **1996**, *79* (12), 3193–3198.

(206) Ning, F.; Cong, W.; Hu, Y.; Wang, H. Additive Manufacturing of Carbon Fiber-Reinforced Plastic Composites Using Fused Deposition Modeling: Effects of Process Parameters on Tensile Properties. *J. Compos. Mater.* **2017**, *51* (4), 451–462. https://doi.org/10.1177/0021998316646169.

(207) Zhong, W.; Li, F.; Zhang, Z.; Song, L.; Li, Z. Short Fiber Reinforced Composites for Fused Deposition Modeling. *Mater. Sci. Eng. A* **2001**, *301* (2), 125–130. https://doi.org/10.1016/S0921-5093(00)01810-4.

(208) Sweeney, C. B.; Lackey, B. A.; Pospisil, M. J.; Achee, T. C.; Hicks, V. K.; Moran, A. G.; Teipel, B. R.; Saed, M. A.; Green, M. J. Welding of 3D-Printed Carbon Nanotube–polymer Composites by Locally Induced Microwave Heating. *Sci. Adv.* **2017**, *3* (6), 1–7. https://doi.org/10.1126/sciadv.1700262.

(209) Weng, Z.; Wang, J.; Senthil, T.; Wu, L. Mechanical and Thermal Properties of ABS/Montmorillonite Nanocomposites for Fused Deposition Modeling 3D Printing. *Mater. Des.* **2016**, *102*, 276–283.

(210) Kalita, S. J.; Bose, S.; Hosick, H. L.; Bandyopadhyay, A. Development of Controlled Porosity Polymer-Ceramic Composite Scaffolds via Fused Deposition Modeling. *Mater. Sci. Eng. C* **2003**, *23* (5), 611–620.

(211) McKelvey, J.; Rice, W. Gear-Pump-Assisted Plasticating Extrusion. *Adv. Poly-mer Technol.* **1982**.

(212) Doi, M.; Edwards, S. F. Dynamics of Concentrated Polymer Systems. Part 1.—Brownian Motion in the Equilibrium State. *J. Chem. Soc. Faraday Trans. 2 Mol. Chem. Phys.* **1978**, *74*, 1789–1801.

(213) Han, C. D.; Chin, H. B. Theoretical Prediction of the Pressure Gradients

in Coextrusion of Non-newtonian Fluids. *Polym. Eng. Sci.* **1979**, *19* (16), 1156–1162. https://doi.org/10.1002/pen.760191605.

(214) Pham, D. T.; Gault, R. S. A Comparison of Rapid Prototyping Technologies. *Int. J. Mach. tools Manuf.* **1998**, *38* (10–11), 1257–1287.

(215) Gao, W.; Zhang, Y.; Ramanujan, D.; Ramani, K.; Chen, Y.; Williams, C. B.; Wang, C. C. L. L.; Shin, Y. C.; Zhang, S.; Zavattieri, P. D. The Status, Challenges, and Future of Additive Manufacturing in Engineering. *Comput. Des.* **2015**, *69*, 65–89. https://doi.org/10.1016/j.cad.2015.04.001.

(216) Eckel, Z. C.; Zhou, C.; Martin, J. H.; Jacobsen, A. J.; Carter, W. B.; Schaedler, T. A. Additive Manufacturing of Polymer-Derived Ceramics. *Science (80-.).* **2016**, *351* (6268), 58–62. https://doi.org/10.1126/science.aad2688.

(217) Murphy, S. V; Atala, A. 3D Bioprinting of Tissues and Organs. *Nat. Biotechnol.* **2014**, *32* (8), 773.

(218) Bose, S.; Vahabzadeh, S.; Bandyopadhyay, A. Bone Tissue Engineering Using 3D Printing. *Mater. today* **2013**, *16* (12), 496–504.

(219) Hong, S.; Sycks, D.; Chan, H. F.; Lin, S.; Lopez, G. P.; Guilak, F.; Leong, K. W.; Zhao, X. 3D Printing of Highly Stretchable and Tough Hydrogels into Complex, Cellularized Structures. *Adv. Mater.* **2015**, *27* (27), 4035–4040.

(220) Compton, B. G.; Lewis, J. A. 3D-printing of Lightweight Cellular Composites. *Adv. Mater.* **2014**, *26* (34), 5930–5935.

(221) Wu, W.; Geng, P.; Li, G.; Zhao, D.; Zhang, H.; Zhao, J. Influence of Layer Thickness and Raster Angle on the Mechanical Properties of 3D-Printed PEEK and a Comparative Mechanical Study between PEEK and ABS. *Materials (Basel).* **2015**, *8* (9), 5834–5846.

(222) Garland, A.; Fadel, G. Design and Manufacturing Functionally Gradient Material Objects with an off the Shelf Three-Dimensional Printer: Challenges and Solutions. *J. Mech. Des.* **2015**, *137* (11), 111407.

(223) Zhao, Z.; Peng, F.; Cavicchi, K. A.; Cakmak, M.; Weiss, R. A.; Vogt, B. D. Three-Dimensional Printed Shape Memory Objects Based on an Olefin Ionomer of Zinc-Neutralized Poly (Ethylene-Co-Methacrylic Acid). *ACS Appl. Mater. Interfaces* **2017**, *9* (32), 27239–27249.

(224) Wu, J.; Yuan, C.; Ding, Z.; Isakov, M.; Mao, Y.; Wang, T.; Dunn, M. L.; Qi, H. J. Multi-Shape Active Composites by 3D Printing of Digital Shape Memory Polymers. *Sci. Rep.* **2016**, *6*, 24224.

(225) Ge, Q.; Qi, H. J.; Dunn, M. L. Active Materials by Four-Dimension Printing. *Appl. Phys. Lett.* **2013**, *103* (13), 131901.

(226) Wang, Q.; Jackson, J. A.; Ge, Q.; Hopkins, J. B.; Spadaccini, C. M.; Fang, N. X. Lightweight Mechanical Metamaterials with Tunable Negative

Thermal Expansion. *Phys. Rev. Lett.* **2016**, *117* (17), 175901.

(227) Pascu, N. E.; Arion, A. F.; Dobrescu, T.; Carutasu, N. L. Fused Deposition Modeling Design Rules for Plastics. *Mater. Plast.* **2015**, *52* (2), 141–143.

(228) Han, C. D. A. E.; Subsidiary, A.; Brace, H. *Multiphase Flow in Polymer Processing*; 1981.

(229) LLC, C. Makrolon® 3208. **2018**, 5–7.

(230) DuPont Packaging & Industrial Polymers DuPont ™ Surlyn ® 9320. **2014**, 9–11.

(231) Coppée, S.; Gabriele, S.; Jonas, A. M.; Jestin, J.; Damman, P. Influence of Chain Interdiffusion between Immiscible Polymers on Dewetting Dynamics. *Soft Matter* **2011**, *7* (21), 9951–9955.

(232) Liu, D. Impact-Induced Delamination—a View of Bending Stiffness Mismatching. *J. Compos. Mater.* **1988**, *22* (7), 674–692.

(233) Smith, W. C.; Dean, R. W. Structural Characteristics of Fused Deposition Modeling Polycarbonate Material. *Polym. Test.* **2013**, *32* (8), 1306–1312.

(234) Adam, G. A. A.; Cross, A.; Haward, R. N. N. The Effect of Thermal Pretreatment on the Mechanical Properties of Polycarbonate. *J. Mater. Sci.* **1975**, *10* (9), 1582–1590. https://doi.org/10.1007/BF01031859.

(235) G'Sell, C.; Hiver, J. M.; Dahoun, A.; Souahi, A. Video-Controlled Tensile Testing of Polymers and Metals beyond the Necking Point. *J. Mater. Sci.* **1992**, *27* (18), 5031–5039. https://doi.org/10.1007/BF01105270.

(236) Akimoto, H.; Kanazawa, T.; Yamada, M.; Matsuda, S.; Shonaike, G. O.; Murakami, A. Impact Fracture Behavior of Ethylene Ionomer and Structural Change after Stretching. *J. Appl. Polym. Sci.* **2001**, *81* (7), 1712–1720. https://doi.org/10.1002/app.1603.

(237) Middleton, L. R.; Szewczyk, S.; Azoulay, J.; Murtagh, D.; Rojas, G.; Wagener, K. B.; Cordaro, J.; Winey, K. I. Hierarchical Acrylic Acid Aggregate Morphologies Produce Strain-Hardening in Precise Polyethylene-Based Copolymers. *Macromolecules* **2015**, *48* (11), 3713–3724. https://doi.org/10.1021/acs.macromol.5b00797.

(238) Haward, R. N. Strain Hardening of Thermoplastics. *Macromolecules* **1999**, *26*, 5860–5869. https://doi.org/10.1021/ma00074a006.

(239) Parsons, E.; Boyce, M. C.; Parks, D. M. An Experimental Investigation of the Large-Strain Tensile Behavior of Neat and Rubber-Toughened Polycarbonate. *Polymer (Guildf).* **2004**, *45* (8), 2665–2684. https://doi.org/10.1016/j.polymer.2004.01.068.

(240) Gong, S.; Schwalb, W.; Wang, Y.; Chen, Y.; Tang, Y.; Si, J.; Shirinzadeh, B.; Cheng, W. A Wearable and Highly Sensitive Pressure Sensor with Ultrathin Gold Nanowires. *Nat. Commun.* **2014**, *5*, 3132.

(241) Bae, S.; Kim, H.; Lee, Y.; Xu, X.; Park, J.-S.; Zheng, Y.; Balakrishnan, J.; Lei, T.; Kim, H. R.; Song, Y. Il. Roll-to-Roll Production of 30-Inch Graphene Films for Transparent Electrodes. *Nat. Nanotechnol.* **2010**, *5* (8), 574.

(242) Qiang, Z.; Guo, Y.; Liu, H.; Cheng, S. Z. D.; Cakmak, M.; Cavicchi, K. A.; Vogt, B. D. Large-Scale Roll-to-Roll Fabrication of Ordered Mesoporous Materials Using Resol-Assisted Cooperative Assembly. *ACS Appl. Mater. Interfaces* **2015**, *7* (7), 4306–4310.

(243) Angmo, D.; Larsen-Olsen, T. T.; Jørgensen, M.; Søndergaard, R. R.; Krebs, F. C. Roll-to-roll Inkjet Printing and Photonic Sintering of Electrodes for ITO Free Polymer Solar Cell Modules and Facile Product Integration. *Adv. Energy Mater.* **2013**, *3* (2), 172–175.

(244) Cooper, K. Materials and Manufacturing Challenges in Hybrid Flexible Electronics. *Minerals, Metals and Materials Society/AIME, 420 Commonwealth Dr., P. O. Box 430 Warrendale PA 15086 USA.[np]. 14-18 Feb*. Minerals, Metals and Materials Society/AIME, 420 Commonwealth Dr., P. O. Box 430 Warrendale PA 15086 USA 2010.

(245) Kim, H.; Almanza-Workman, M.; Garcia, B.; Kwon, O.; Jeffrey, F.; Braymen, S.; Hauschildt, J.; Junge, K.; Larson, D.; Stieler, D. Roll-to-roll Manufacturing of Electronics on Flexible Substrates Using Self-aligned Imprint Lithography (SAIL). *J. Soc. Inf. Disp.* **2009**, *17* (11), 963–970.

(246) Park, S.; Lee, D. H.; Russell, T. P. Self-Assembly of Block Copolymers on Flexible Substrates. *Adv. Mater.* **2010**, *22* (16), 1882–1884.

(247) Mansky, P.; Liu, Y.; Huang, E.; Russell, T. P.; Hawker, C. Controlling Polymer-Surface Interactions with Random Copolymer Brushes. *Science (80-.).* **1997**, *275* (5305), 1458–1460.

(248) Rockford, L.; Liu, Y.; Mansky, P.; Russell, T. P.; Yoon, M.; Mochrie, S. G. J. Polymers on Nanoperiodic, Heterogeneous Surfaces. *Phys. Rev. Lett.* **1999**, *82* (12), 2602.

(249) Stoykovich, M. P.; Müller, M.; Kim, S. O.; Solak, H. H.; Edwards, E. W.; De Pablo, J. J.; Nealey, P. F. Directed Assembly of Block Copolymer Blends into Nonregular Device-Oriented Structures. *Science (80-.).* **2005**, *308* (5727), 1442–1446.

(250) Morkved, T. L.; Lu, M.; Urbas, A. M.; Ehrichs, E. E.; Jaeger, H. M.; Mansky, P.; Russell, T. P. Local Control of Microdomain Orientation in Diblock Copolymer Thin Films with Electric Fields. *Science (80-.).* **1996**, *273* (5277), 931–933.

(251) Feng, X.; Tousley, M. E.; Cowan, M. G.; Wiesenauer, B. R.; Nejati, S.;

Choo, Y.; Noble, R. D.; Elimelech, M.; Gin, D. L.; Osuji, C. O. Scalable Fabrication of Polymer Membranes with Vertically Aligned 1 Nm Pores by Magnetic Field Directed Self-Assembly. *ACS Nano* **2014**, *8* (12), 11977–11986.

(252) Leach, K. A.; Gupta, S.; Dickey, M. D.; Willson, C. G.; Russell, T. P. Electric Field and Dewetting Induced Hierarchical Structure Formation in Polymer/Polymer/Air Trilayers. *Chaos An Interdiscip. J. Nonlinear Sci.* **2005**, *15* (4), 47506.

(253) Kao, J.; Thorkelsson, K.; Bai, P.; Rancatore, B. J.; Xu, T. Toward Functional Nanocomposites: Taking the Best of Nanoparticles, Polymers, and Small Molecules. *Chem. Soc. Rev.* **2013**, *42* (7), 2654–2678. https://doi.org/10.1039/c2cs35375j.

(254) Choi, E. S.; Brooks, J. S.; Eaton, D. L.; Al-Haik, M. S.; Hussaini, M. Y.; Garmestani, H.; Li, D.; Dahmen, K. Enhancement of Thermal and Electrical Properties of Carbon Nanotube Polymer Composites by Magnetic Field Processing. *J. Appl. Phys.* **2003**, *94* (9), 6034–6039.

(255) Varga, Z.; Filipcsei, G.; Zr?nyi, M. Magnetic Field Sensitive Functional Elastomers with Tuneable Elastic Modulus. *Polymer (Guildf).* **2006**, *47* (1), 227–233. https://doi.org/10.1016/j.polymer.2005.10.139.

(256) Benkoski, J. J.; Jones, R. L.; Douglas, J. F.; Karim, A. Photocurable Oil/Water Interfaces as a Universal Platform for 2-D Self-Assembly. *Langmuir* **2007**, *23* (7), 3530–3537.

(257) Cakmak, M.; Batra, S.; Yalcin, B. Field Assisted Self-assembly for Preferential through Thickness (“Z-direction”) Alignment of Particles and Phases by Electric, Magnetic, and Thermal Fields Using a Novel Roll-to-roll Processing Line. *Polym. Eng. Sci.* **2015**, *55* (1), 34–46.

(258) Robinson, A. P.; Minev, I.; Graz, I. M.; Lacour, S. P. Microstructured Silicone Substrate for Printable and Stretchable Metallic Films. *Langmuir* **2011**, *27* (8), 4279–4284.

(259) Myers, A. C.; Huang, H.; Zhu, Y. Wearable Silver Nanowire Dry Electrodes for Electrophysiological Sensing. *RSC Adv.* **2015**, *5* (15), 11627–11632.

(260) Hu, N.; Fukunaga, H.; Atobe, S.; Liu, Y.; Li, J. Piezoresistive Strain Sensors Made from Carbon Nanotubes Based Polymer Nanocomposites. *Sensors* **2011**, *11* (11), 10691–10723.

(261) Kang, I.; Schulz, M. J.; Kim, J. H.; Shanov, V.; Shi, D. A Carbon Nanotube Strain Sensor for Structural Health Monitoring. *Smart Mater. Struct.* **2006**, *15* (3), 737.

(262) Park, J.; Lee, Y.; Hong, J.; Ha, M.; Jung, Y.-D.; Lim, H.; Kim, S. Y.; Ko, H. Giant Tunneling Piezoresistance of Composite Elastomers with Interlocked Microdome Arrays for Ultrasensitive and Multimodal Electronic Skins. *ACS*

Nano **2014**, *8* (5), 4689–4697.

(263) Simien, D.; Fagan, J. A.; Luo, W.; Douglas, J. F.; Migler, K.; Obrzut, J. Influence of Nanotube Length on the Optical and Conductivity Properties of Thin Single-Wall Carbon Nanotube Networks. *ACS Nano* **2008**, *2* (9), 1879–1884.

(264) Cakmak, M.; Batra, S.; Yalcin, B. Field Assisted Self-Assembly for Preferential Through Thickness (“ z-Direction ”) Alignment of Particles and Phases by Electric , Magnetic , and Thermal Fields Using a Novel Roll-to-Roll Processing Line. **2014**, No. 1, 1–13. https://doi.org/10.1002/pen.

(265) Dow Chemical Company. SYLGARD™ 184 Silicone Elastomer. **2017**.

(266) Ziff, R. M.; Torquato, S. Percolation of Disordered Jammed Sphere Packings. *J. Phys. A Math. Theor.* **2017**, *50* (8), 85001.

(267) Matheson, A. J. Computation of a Random Packing of Hard Spheres. *J. Phys. C Solid State Phys.* **1974**, *7* (15), 2569.

(268) Roberson, D. A.; Wicker, R. B.; MacDonald, E. Ohmic Curing of Three-Dimensional Printed Silver Interconnects for Structural Electronics. *J. Electron. Packag.* **2015**, *137* (3), 31004.